

Dipl.-Ing. Sabine F. Kruschwitz

**Assessment of the
complex resistivity behavior
of salt affected building materials**

Die vorliegende Arbeit entstand an der Bundesanstalt für Materialforschung und -prüfung (BAM).

Impressum

**Assessment of the
complex resistivity behavior
of salt affected building materials**

2008

Herausgeber:

Bundesanstalt für Materialforschung und -prüfung (BAM)

Unter den Eichen 87

12205 Berlin

Telefon: +49 30 8104-0

Telefax: +49 30 8112029

E-Mail: info@bam.de

Internet: www.bam.de

Copyright © 2008 by Bundesanstalt für
Materialforschung und -prüfung (BAM)

Layout: BAM-Arbeitsgruppe Z.64

ISSN 1613-4249

ISBN 978-3-9811655-9-3

Assessment of the complex resistivity behavior of salt affected building materials

vorgelegt von
Diplom-Ingenieurin
Sabine F. Kruschwitz
aus Berlin

von der Fakultät VI - Planen Bauen Umwelt
der Technischen Universität Berlin
zur Erlangung des akademischen Grades
Doktorin der Naturwissenschaften

- Dr. rer. nat. -

genehmigte Dissertation

Promotionsausschuss:

Vorsitzender:	Prof. G. Franz
Berichter:	Prof. U. Yaramanci
Berichter:	Prof. A. Weller (University Clausthal, Germany)
Berichter:	Prof. A. Binley (University of Lancaster, UK)

Tag der wissenschaftlichen Aussprache: 29. Oktober 2007

Berlin 2007
D 83

ASSESSMENT OF THE COMPLEX RESISTIVITY BEHAVIOR OF SALT AFFECTED BUILDING MATERIALS

- SABINE F KRUSCHWITZ -

Dissertation, Technical University of Berlin, Department of Applied Geophysics, 2007

Keywords: complex resistivity, spectral induced polarization, building materials, deteriorating salts, moisture, zeta-potential, FD effective impedance modelling

Synopsis

The ability to reliably predict the amount and type of salts within a wet masonry is one of the most important and challenging subjects in the field of non-destructive combat of salt attack and preserving buildings and monuments of historical or archaeological value. To investigate the potential value of complex resistivity (CR) measurements for the early detection of salt and moisture related stone altering, a controlled salt type and concentration experiment series has been performed and a new procedure of an image based effective impedance modelling developed.

Complex resistivity magnitude and phase measurements in the frequency range of 1 mHz to 100 Hz were acquired on a wide variety of wholly and partially brine saturated building stone samples. Deteriorating agents $NaCl$, Na_2SO_4 , $CaCl_2$ and $MgSO_4$ were used. Since water and salt are not measured directly, the method is incapable of deducing possible building damages lacking a priori information. In the case of saturated materials, and provided thorough calibration data are available, a reliable estimate of salt concentration is possible from the measured resistivity magnitude. Additional indication on the dominant cation in the solution can be obtained from the measured resistivity phase, which is significantly higher the lower its valency. Furthermore, the measurements reported in this study give an important guide to the limitations of CR in obtaining pore surface area and pore throat estimates. For wet porous materials, in which polarization occurs due to complex surface conduction, the dominant pore throat and amount of specific surface affect its polarizability. Sandstones, sand-limestones and aerated concretes are more qualified observation objects (pore throats between 20 and 100 μm), whereas for bricks (pore sizes often $< 5 \mu\text{m}$) the method seems far less favorable. For those materials, which exhibit a Cole-Cole (C-C) type of relaxation, the phase peak is observed to decrease significantly with pore throat size and to occur at higher frequencies. The predicted power-law correlation between the C-C relaxation time and characteristic length scale (pore throat size for consolidated materials) is supported by the presented data.

The experimental salinity study reveals how responsive polarization (in terms of imaginary conductivity) is to changing the ionic concentration or composition of the pore fluid. The properties of the electrical double layer and particularly its chemical composition are most likely the crucial controlling factors. The imaginary conductivity is observed to increase for most materials up to fluid salinities of about 1 S/m - a fact, that may be attributed to a mechanism of ion saturation within the electrical double layer; further

ion supply seems to counteract this leading to ion-ion interactions, which decrease ionic mobility.

CR measurements on partially saturated samples demonstrate the method's sensitivity to water content. For most materials the imaginary conductivity component decreased significantly faster than the real component. Independent of the pore fluid and even though its salinity naturally increased during the evaporative drying procedure, the normalized saturation exponent of the quadrature component was about twice as high as the real one especially for clay-rich sandstones. The results revealed diverse behavior such as decreases and increases in relaxation time with saturation. In some cases a suppression of a distinctive relaxation curve at low saturations was observed. The results indicate, that contrary to conclusions from recent related studies, the correlation between a C-C relaxation time and hydraulic properties may be limited.

In order to infer information on the charge distributions within the EDL, zeta-potentials and surface charge densities were obtained from electroacoustic measurements on particle suspension containing the same amounts and types of salt like used in the brine saturation CR study. The results add weight to the assumption that there is some universal positive relationship between zeta-potential and imaginary conductivity. A notable dependence of imaginary conductivity on diffuse layer surface charge was only observed in case of one sandstone (Cottaer), this being the material with the most abundant clay content.

An image based effective impedance modelling approach revealed the fact that, even though it is not able to factor scale effects in, it is helpful to study general microstructural implications on CR responses. It was observed, that an increasing salt concentration (that creates a shrinking electrical double layer) reduces the peak phase and moves it towards higher frequency. The same effect would have an increasing fluid conductivity for a otherwise fixed microstructure. For some combinations of material and salt, however, in the experimental work the peak phase was observed to shift towards lower frequency: a phenomenon that could not be explained with the modelling. Therefore, it is assumed that chemical properties, like ion mobilities or other surface chemistry properties (ion-exchange processes) must be regarded to conclusively explain surface conductivity mechanisms.

Other experimental observations like the alteration of CR spectra at desaturation could likewise be modelled. If these models truly mimic the effective electrical properties, the results give new implications on the effective medium behavior.

Concluding, the author values the complex resistivity method as a possible effective non-destructive testing (NDT) tool for a wide range of building stones. Depending on pore size and saturation important additional information can be obtained. In all cases, a priori information and calibration data are essential, that is, CR should not be treated as a stand-alone method. Further measurements are needed to develop a more complete model of the electrical double layer and its alteration with changing salinity and ion types.

ASSESSMENT OF THE COMPLEX RESISTIVITY BEHAVIOR OF SALT AFFECTED BUILDING MATERIALS

- SABINE F KRUSCHWITZ -

Dissertation, Technische Universität Berlin, Fachgebiet Angewandte Geophysik, 2007

Stichworte: Komplexer elektrischer Widerstand, Spektral Induzierte Polarisation, Baustoffe, Schadsalze, Feuchte, Zeta-Potential, FD effektive Impedanzmodellierung

Zusammenfassung

Die Art und den Grad einer Salzbelastung in feuchten Baustoffen festzustellen, gehört zu den wichtigsten und gleichfalls schwierigsten Aufgaben im Bereich der zerstörungsfreien Prüfung. Die vorliegende Arbeit beschäftigt sich mit dem möglicherweise bislang ungenutzten Potential spektraler Leitfähigkeitsmessungen und deren praktischer Anwendbarkeit. Dazu wurde erstens eine umfangreiche Experimentreihe an unterschiedlichen Baustoffen mit vier Salzen in variierenden Konzentrationen durchgeführt, um die Sensitivität komplexer Leitfähigkeitsmessungen der für den Baubereich relevanten Salzmengen zu untersuchen. Zweitens wurde der Einfluß der Sättigung für verschiedene Ausgangsfluide nachvollzogen, da Feuchteschäden häufig räumlich begrenzt sind und sich in ihrer Stärke verändern. Da das spektrale Leitfähigkeitsverhalten allerdings ein Wechselspiel verschiedener Stoffeigenschaften ist, beschäftigt sich diese Arbeit darüber hinaus auch mit dem Versuch, chemisch von strukturell bedingten Impedanzänderungen unterscheiden zu lernen. In einer Finite Differenzen Modellierung wurden die effektiven Impedanzen synthetischer Mikrostrukturen berechnet und die Auswirkungen von Strukturunterschieden untersucht.

Die komplexen elektrischen Eigenschaften wurden generell im Frequenzbereich 1 mHz -100 Hz bestimmt. Als Schadsalze wurden $NaCl$, Na_2SO_4 , $CaCl_2$ und $MgSO_4$ verwendet. Da elektrische Verfahren Wasser und Salz nicht direkt, sondern indirekt über den Widerstand messen, sind a-priori Informationen bei der Auswertung erforderlich. Liegen Kalibrationsdaten vor, kann im Fall eines vollständig gesättigten Baustoffes allein anhand der (realen und einfach messbaren) Widerstandsamplitude eine verlässliche Einschätzung des Salzgehaltes vorgenommen werden. Die Phase des komplexen elektrischen Widerstands enthält Informationen über den Charakter (Wertigkeit) des dominanten Kations in der Porenfluidlösung. In porösen, feuchten Baustoffen, in denen Polarisation als Folge komplexer Grenzflächenleitfähigkeit auftritt, bestimmen generell das Matrixmaterial, der Porendurchmesser und die innere Oberfläche seine Aufladbarkeit. Die Ergebnisse der vorliegenden Arbeit zeigen jedoch deutlich, daß diese Größen nur bedingt aus elektrischen Messungen abgeleitet werden können. Liegt die durchschnittliche Porenhalsgröße eines Baustoffs zwischen 20 und 100 μm , kann in der Regel eine deutliche Aufladbarkeit im untersuchten Frequenzbereich beobachtet werden. In feinporigen Baustoffen wie den meisten Tonziegeln sind die dominanten Porenhalsgrößen kleiner als 5 μm , und die Aufladbarkeit liegt oft nur noch im Bereich der Messgenauigkeit. Generell können material-

und fluidbedingt verschiedene Arten von Widerstands-/Frequenzverhalten beobachtet werden. Für solche Baustoffe, die ein Cole-Cole (C-C) Relaxationsverhalten zeigen, wird beobachtet, daß die Relaxationszeit τ und ebenfalls die Magnitude des Phasenmaximums mit zunehmenden Porenhalbdurchmesser abnehmen. Die hier vorgestellte Datenbasis untermauert den theoretisch vorhergesagten exponentiellen Zusammenhang zwischen τ und einer materialbedingten, charakteristischen Relaxationslänge - im Fall von Festmaterialien der Porenhalblänge.

In der Salinitätsstudie konnte nachgewiesen werden, wie sensitiv die Polarisierbarkeit (Imaginärteil der Leitfähigkeit) auf die Ionenkonzentration und sogar die Art der im Fluid enthaltenen Ionen reagiert. Ausschlaggebend sind wahrscheinlich Veränderungen in der elektrischen Doppelschicht (EDL) hinsichtlich ihrer Geometrie und chemischen Zusammensetzung. Der Imaginärteil der elektrischen Leitfähigkeit steigt für die meisten Baustoffe bis zu Fluidleitfähigkeiten von 1 S/m an. Dies liegt wahrscheinlich an der fortschreitenden Ionensättigung des EDL. Ist eine gewisse Sättigungsstufe erreicht, führt eine weitere Ionenzufuhr zu zunehmenden elektrostatischen Wechselwirkungen und schließlich abnehmenden Ionendiffusionskoeffizienten.

Die experimentellen Befunde dieser Arbeit weisen auch den Einfluß des Durchfeuchtungsgrades auf die komplexen Leitfähigkeitseigenschaften deutlich nach. Für die meisten Baustoffe nimmt mit dem Wassergehalt der Imaginärteil der Leitfähigkeit stärker als der Realteil. Unabhängig von der Art des Porenfluids und obwohl die Leitfähigkeit des Porenfluids während der evaporativen Trocknung zunahm, lagen die Sättigungsexponenten des Imaginärteils in der Regel doppelt so hoch wie die des Realteils. Es deutet sich im Vergleich dieser Daten mit den Beobachtungen anderer Autoren an, daß der Tongehalt und möglicherweise der Zementationsgrad eines Materials ausschlaggebend für ein solches, nicht der bisherigen Theorie entsprechendes Verhalten sind. Darüber hinaus wurde beobachtet, daß die Position des Phasenmaximums im Frequenzbereich und damit die C-C Relaxationszeit für einige Baustoffe zu-, für andere abnahm und für wieder andere der Phasenpeak schnell ganz abflachte. Diese Ergebnisse zeigen deutlich, daß der kürzlich von anderen Autoren aufgezeigte Zusammenhang von C-C Relaxationszeit und hydraulischen Eigenschaften (Permeabilität) zumindest nicht bedingungslos gültig ist und weiterer Forschungsbedarf besteht.

Um die Eigenschaften der elektrischen Doppelschicht in Abhängigkeit der Porenfluidchemie zu untersuchen, wurden Zetapotentialmessungen durchgeführt sowie mittels Autotitration Oberflächenladungsdichten ermittelt. Die verwendeten Partikelsuspensionen wurden in gleicher Weise mit den Schadsalzen versetzt wie zuvor die Baustoffproben in den elektrischen Messungen. Die Auswertung der elektroakustischen Messungen deutet zwar generell einen positiven linearen Zusammenhang zwischen Zetapotential und dem Imaginärteil der Leitfähigkeit an, dieser ist jedoch schwächer als erwartet. Eine ausgeprägte Abhängigkeit der imaginären Leitfähigkeit konnte nur in einem Fall nachgewiesen werden, nämlich für den sehr tonhaltigen Cottaer Sandstein.

In der einschlägigen Literatur wird davon ausgegangen, daß die komplexen elektrischen Eigenschaften eines Materials außer vom Chemismus der elektrischen Doppelschicht auch von der Geometrie des Porenraumes in einem Material bestimmt werden. In einem neuartigen Versuch, diese beiden Phenomäne zu trennen, wurde eine Parameterstudie mittels einer FD-Impedanzmodellierung durchgeführt, in der gezielt Längenverhältnisse und Leitfähigkeiten verändert werden konnten. Es wurde grundsätzlich von einem Dreiphasensystem aus Matrix, elektrischer Doppelschicht und Fluid ausgegangen. Eine Erhöhung der Salzfracht in der Fluidphase bewirkt zum einen eine Zunahme der Fluidleitfähigkeit und zum anderen eine Abnahme der Doppelschichtmächtigkeit. Beide Vorgänge hatten in der Modellierung zur Folge, daß das Phasenmaximum abnahm und sich zu höheren Frequenzen verschob. Dies wurde auch für die Mehrheit der Baustoffe in der experimentellen Arbeit beobachtet. Nur im Fall des Cottaer Sandstein verschob sich das Phasenmaximum mit zunehmender Fluidsalinität zu niedrigeren Frequenzen; möglicherweise findet hier eine chemische Umstrukturierung (Ionenaustauschvorgänge) statt, die abhängig von der Art und dem Gehalt der Tonfraktion und dem Chemismus des Porenfluids sein könnten. Die Beobachtungen der Entsättigungsexperimente konnten ebenfalls mit der effektiven Impedanzmodellierung nachvollzogen werden. Falls die hier verwendeten, stark vereinfachten, synthetischen Modelle die komplexen elektrischen Eigenschaften wahrheitsgemäß abbilden, bieten sie die Möglichkeit eines erweiterten Verständnisses des Leitfähigkeitsverhaltens teilgesättigter Medien.

Komplexe Widerstandsmessungen bieten also durchaus Potential für die Anwendung im Bereich der zerstörungsfreien Bauwerksanalyse, es handelt sich zum gegenwärtigen Zeitpunkt jedoch noch um eine Methode im Forschungsstadium. Die Aussagekraft und Anwendbarkeit des Verfahrens variiert stark mit der durchschnittlichen Porengröße, dem Durchfeuchtungsgrad und der Salzfracht des Untersuchungsobjekts. In jedem Fall sind a-priori Informationen und -sofern quantitative Aussagen getroffen werden sollen- auch Kalibrationsdaten erforderlich. Das Verfahren sollte nicht allein angewendet werden. Um quantitativ Salzgehalte zu bestimmen, muß die Materialfeuchte bekannt sein und vice versa. Zuverlässiger wird die Interpretation, wenn die Art des Schadsalzes (oder Fluids, z.B. Regenwasser oder Leitungswasser) bekannt ist. Weitere, leicht kontrollierbare Laboruntersuchungen sind letztlich notwendig, um ein umfassenderes Model der Polarisationsvorgänge in der elektrischen Doppelschicht zu entwickeln.

Contents

Synopsis	v
Zusammenfassung	vii
1 Introduction	1
1.1 Background and rationale	1
1.2 Objectives	2
1.3 Significance	3
1.4 Sources of moisture and salt in building materials	4
2 Complex resistivity	7
2.1 CR parameter and related quantities	9
2.2 Electrochemical polarization	11
2.2.1 Electrical double layer	13
2.2.2 Surface chemistry	14
2.3 Zeta-potential and electrokinetic phenomena	17
2.4 Interpretation of CR data	21
2.4.1 Relaxation models	21
2.4.2 Constant Phase Model	23
2.5 Water saturation	24
3 Salt experiments	27
3.1 Experimental procedure	27
3.1.1 Sample selection and characterization	27
3.1.2 Sample preparation	27
3.1.3 Cell and impedance devices	31
3.2 Material type	32
3.2.1 CR spectra	32
3.2.2 CR parameter and lithology	35
3.3 Salt type and concentration	39
3.4 Conductivity components σ' and σ''	45
3.5 Cole-Cole modelling	50
3.6 Comparison distilled water / tap water	55
3.7 Summary	59

4 Saturation experiments	63
4.1 Experimental Procedure	63
4.2 Results	63
4.2.1 CR Spectra	63
4.2.2 Cole-Cole parameters	64
4.2.3 Saturation exponents	68
4.3 Summary	71
5 Electroacoustic experiments	73
5.1 Zeta-potential	73
5.1.1 Surface charge density	80
5.2 Discussion	83
5.3 Summary	86
6 Microstructure based Impedance Response Computing	89
6.1 Finite Difference Program AC2D	89
6.2 Microstructural parameter study	91
6.2.1 Interface shape	93
6.2.2 Developing pore throat	93
6.2.3 Interface thickness	98
6.2.4 Changing conductivity	102
6.2.5 Changing saturation	104
6.2.6 Archie relationships	109
6.3 Summary	111
7 Conclusions	113
Appendices	117
A Mineralogy of the materials investigated	119
B Experiment set-up and reliability tests	127
C Additional experimental results	131
D FD modelling with Ac2D	141
List of Symbols and Abbreviations	145
List of Figures	147
List of Tables	155
Bibliography	157

Acknowledgements	163
Vita	165

1 Introduction

1.1 Background and rationale

Masonry has been the architectural material of choice since time immemorial. Historic and artistic monuments are the most visible aspects of our cultural heritage. Buildings are dynamic systems often made of a variety of materials and reacting to a range of stresses. Stone weathering and decomposition are natural processes. Pollution, urbanization, public access or other man-made phenomena expand the universal threats stones undergo. One immediate consequence of the increasing number of flooding disasters in the past years will surely be the awareness of the drastic damaging power of waters and the topicality of this work. Apart from the numerous vast and imminent destructions, such catastrophes leave damage patterns, which afflict buildings during their remaining life cycle. Cooperative efforts in stone conservation involves such disciplines as geology, chemistry, meteorology, civil and chemical engineering. Even though there might be a lack of common vocabulary among scientists and conservators, it must be understood how these individual factors relate to the whole.

Modern long-term conservation policy concentrates on the early diagnosis and fighting the causes of decay. According to the Committee on Conservation of Historic Stone Buildings and Monuments (CETS) of the American National Materials Advisory Board, much of the trouble in the present situation lies in the insufficient number and level of competence technologies available. Moreover, the committee agrees that the dominant factor in deterioration of stone and masonry structures is moisture. Once water is permitted to penetrate a masonry wall, the deterioration will accelerate very quickly.

Although there might be good control in the laboratory, often problems occur with scale and data collected under complicated ambient conditions in the field. It is often assumed, within the industry and among outsiders, that damp-proofing techniques have been thoroughly researched and developed. But still, by normal academic standards, very little work has been carried out and often results have tended to cast doubt upon the accuracy of diagnosis. Either methods are precise and destructive or ambiguous, fairly quantitative and often non-satisfactory in lateral and downward resolution. Naturally, a recurring theme for those concerned with stone conservations and maintenance is the importance of reliable field data either to evaluate damages or to monitor the progress of chemical treatments. According to the British Building Research Establishment the only approved way is the oven-drying or gravimetric Darr-method, which is, essentially, destructive. Almost 10 years ago the combined use of nuclear magnetic resonance (NMR) and gamma-ray absorption has been reported as being highly qualified for the indepen-

dent measurement of water and salts in damaged materials (Holm et al., 1997). Despite its theoretical compelling power, it never became a ready-to-use application in the field, reasons of which might be financially or manageably.

Today, despite the fact that electrical measurements are generally considered to be sensitive to water content, their informational value and application is still very limited in the field of civil engineering. Misinterpretations, theoretical and experimental failures are all-too easy when it comes to heterogenous materials. Having no a-priori information available, common direct-current measurements can be ambiguous. Resistivity variations may either be due to material or water content changes, salt loads, mounting parts or imperfections. Still, the value of qualitative measurements has been shown by different authors in the past decade. Kahle (1994) published a wide study into the detection of structural inhomogeneities in masonry based upon the variation of the resistivities. More recently Lataste et al. (2001), Latatste et al. (2003) and Chouteau and Beaulieu (2002) reported on the use of resistivity methods for the detection of cracks, voids and backfilling in concrete structures. Raupach and Wolff (2002) tested multi-ring electrodes to monitor the effectiveness of different sealings. Despite this activity: these investigations using dc-resistivity measurements have rather qualitative than reliable quantitative and evaluative character.

Compared to on-site measurements a good deal of promising, but destructive laboratory work has been done. The study of the frequency dependent electrical properties as being done in impedance spectroscopy (IS) or frequency dependent resistivity (CR) measurements is a powerful tool since the measured spectra are sensitive to surface chemical and microgeometrical properties of a medium. The outcome of a number of recent publications, mostly coming from a geophysical background, encouraged the study of frequency dependent resistivity measurements as a possible auspicious non-destructive testing (NDT) tool for all kinds of porous, wet building materials. Lesmes and Frye (2001) reported on the influence of changing pore fluids on the complex resistivity responses of sandstone. For the same material Breede et al. (2005) and Breede and Weller (2006) discuss the effect of a variety of chlorine salts. All working groups agree that frequency dependent electrical behavior is a complex function of pore solution chemistry, surface chemical properties, and sample microgeometry.

An extensive investigation into the effect of saturation on induced polarization responses has been published in Binley et al. (2005). Encouraged by their findings, the first general study into complex resistivity properties of building stones was presented in Kruschwitz et al. (2005). Measurements on saturated laboratory samples proved that the interpretation of CR characteristics may launch a new way of non-invasive material discrimination and characterization.

1.2 Objectives

The general aim of the work here is to determine the affect of water saturation and pore fluid chemistry on the CR response of building materials with a view to establishing the

potential value of CR for determining environmental variables affecting the weathering process in a non-destructive manner. The specific objectives of the study are:

- to examine closely the behavior of building materials in the low electrical frequency domain, including the interpretation of the results with models which have been suggested for electrical relaxation in wet porous media;
- to investigate how the amount or type of salt changes the CR characteristics of polarizable materials and to decide, whether the method is apt to assess material damages in an accurate and comprehensible way;
- to determine, experimentally, how saturation affects the complex resistivity and estimate, whether fluid and salt content can be determined simultaneously;
- to address the potential value of CR from the results obtained in the laboratory for the non-invasive material characterization and specify what a-priori information might be essential for such use;
- to illustrate, by simulations, the effective impedance responses of multi-phase systems and address characteristic length scales or conductivity properties crucial for the polarization behavior.

1.3 Significance

The ability to qualitatively identify a salt contamination and its spatial distribution without using invasive procedures would greatly benefit the stone conservation industry in both cost and time. Therefore a better understanding of the effect of saturation on CR is required to accurately interpret measurements collected wholly or partially in unsaturated media. But, since both saturation as well as the chemical composition of the fluid and its interplay with the matrix strongly alter CR behavior, the method's ability to unlink the two needs to be described.

Another important aspect of this work, which comprises numerous in terms of physical properties and chemical composition very heterogeneous materials, is to improve the understanding of polarization and complex resistivity behavior in general. The author is unaware of other publications on such a wide variety of materials focussed on the systematic change of chemical composition and trying to deconvolve these from microgeometrical sample effects. It is, therefore, anticipated, that the findings will have value to wide community, such as those concerned with natural materials.

There are several theories about the role of the different layers of polarizing charges at the matrix-fluid interface, however, these are still rather assumptious in character and lacking complete laboratory evidence. Here an attempt is made, to examine by electroacoustic measurements, the diffuse part of the electrical double layer and investigate both how the layer changes for each material with salt concentration and type. Hence, the outcome of this work may also lead to the development of a more capacious theoretical model of electrical polarization.

1.4 Sources of moisture and salt in building materials

Most moisture related problems in building materials are due to rainwater ingress. Other sources can be leaking plumbing, roofs and gutters or sealant failures. Similarly, air condensation, caused by inadequate levels of heating and ventilation, can lead to damage. Rising ground moisture, travelling from the ground upward by capillary action, can also leave typical damage patterns.

Salts can be derived from several sources. Laboratory analysis of salt contaminated masonry samples typically yields a large array of ions: sulfates, nitrates, chlorides, sodium, potassium, magnesium and calcium in varying concentrations. Table 1.1 summarizes the most common deterioration salts according to Kabrede (2003).

Table 1.1: Most common deterioration salts. Source: Kabrede (2003).

Class	Chemical expression	Salt
Sulfates	$MgSO_4 \cdot 7H_2O$	magnesium sulfate, epsomite
	$NaSO_4 \cdot 10H_2O$	sodium sulfate, glauber's salt
	$CaSO_4 \cdot 2H_2O$	calcium sulfate, gypsum
	$3CaO \cdot Al_2O_3 \cdot CaSO_4 \cdot 32H_2O$	ettringite
Chlorides	$NaCl$	sodium chloride, table salt
	$CaCl_2 \cdot 6H_2O$	calcium chloride
Nitrates	$Mg(NO_3)_2 \cdot 6H_2O$	magnesium nitrate
	$Ca(NO_3)_2 \cdot 4H_2O$	calcium nitrate
	$5Ca(NO_3)_2 \cdot 4NH_4NO_3 \cdot 10H_2O$	lime salpeter
Carbonates	$Na_2CO_3 \cdot 10H_2O$	sodium carbonate, soda
	K_2CO_3	potassium carbonate, potash
	$CaCO_3$	calcium carbonate, lime

Natural and material inherent sources Salt accumulation in walls often originates from movement of groundwater into building foundations by capillary action or wicking upwards into masonry, stucco or concrete. Subsequent horizontal sealing is controversially discussed as being one of the most difficult rehabilitation tasks. Most natural stones, cementitious materials and binder contain sulfates or carbonates of sodium, magnesium, potassium and calcium as well as various chlorides and sometimes nitrates. These salts are usually locked into the matrix and remain there during normal cure, rising groundwater, however, dissolves and transports them.

Sea salt damage is a well-known problem not only regions located near the sea but also in continental areas. Sea salt may stem from rising moisture, be carried as spray by the wind or due to flooding (Lubelli et al., 2004). Another problem associated with sea salts is reported in CETS (1982): since brick is an artificial building material made of natural raw material, another potential source of soluble salts may lie in the composing sands and clays.

For ancient bricks, and sometimes for mortars, it can be assumed the materials used would not meet present requirements: instead of fresh water, brackish water, or salt water might have been used. Sea sand may have been used rather than river sand. In the present day manufacturing process highly soluble salts are washed from the raw materials and a barium salt is added to react with the calcium sulfate which may be present. In this reaction, the product is two fairly insoluble compounds-barium sulfate and calcium carbonate.

It has also been noted that the occurrence of efflorescence bears a relationship to the type of mortar used. With a particular type of brick and a certain mortar no efflorescence may occur, whereas, the same brick with different mortar may produce a wall heavily coated with salt deposits. Usually, Portland cement is a potential source of sulfates. Sulphates contribute significantly to the decay of stonework and sculpture where cement has been used in past repairs, particularly for grouting. The use of low alkali cement in mortar and grout will minimize efflorescence, at least from this source.

Anthropogenic sources Chemical weathering due to rainwaters which are usually charged with carbon dioxide and sulfate in urban and industrial areas is often pointed out as being the key factor of stone decay. However, not only acid rain, but also polluted gases and dusts deposit deleterious constituents. Groundwater can potentially be rich in ingredients from several sources like deicing salts, fertilisers or other leaching residues from the soil. Unusually high levels of salt may result from the building's function (for example stables, purification plants) or from a single event in the building's history, and in this case the problem may be confined to a specific area.

In some cases, actions intended to preserve, clean or restore masonry can have instead deleterious effects. Chemicals in proprietary cleaning compounds are a potential source of soluble salts if not thoroughly rinsed from building facades. In particular, care must be taken in using alkaline cleaners and paint strippers based on sodium hydroxide.

Decay mechanisms The main mechanism of deterioration is the same for all salts. When salts crystallize (or freeze), they expand, building up pressure, which is sufficient to cause spalling and delamination. The parameters needed to describe the porous nature of the solid are obtainable from water imbibition, capillary rise, and pore-size distribution measurements. The most typical decay patterns are failure due to crystallization, hydration, increasing equilibrium moisture content due to hygroscopicity.

It is difficult to generalize but micro-porous materials usually tend to be of inferior durability. Open textured materials with larger pores, in contrast are more durable. Sandstones, especially when having a calcium carbonate binder (calcareous sandstones) tend to be more susceptible than other sandstones. More dense and less porous sandstones, are much less susceptible to salt related damage. High fired vitrified ceramic materials are more resistant than low fired porous ceramics. In most cases, typically joints are also affected. Often the zone of deterioration only affects the outer brick front, which is observed to be between 0.5 and 1 cm thick.

2 Complex resistivity

Electrical conductivity and polarizability are fundamental physical material properties. The interaction of electromagnetic fields with matter is described by Maxwell's equations. The total current \mathbf{J}_t can be distinguished as "conduction current", \mathbf{J}_c , where charges are moved over distances larger than the order of atomic dimensions, and displacement current, \mathbf{J}_d , which refers to the reorientation of bound charge over distances which are on the order of angstroms (Fuller and Ward, 1970; Pelton et al., 1983). According to that Maxwell's second equation may be written:

$$\nabla \times \mathbf{H} = \mathbf{J}_c + \mathbf{J}_d = \mathbf{J}_t \quad (2.1)$$

where

$$\mathbf{J}_d = \frac{\partial \mathbf{D}}{\partial t}, \quad (2.2)$$

with \mathbf{H} being the magnetic field strength, and \mathbf{D} the dielectric displacement field. In the general case of non-linear, anisotropic and inhomogeneous matter, the dielectric displacement field \mathbf{D} and \mathbf{J}_c are dependent on position, direction and field strength. For low current densities ($\mathbf{J} < 10^{-2} A/m^2$), constant temperature and pressure, the relationship between current density and electrical field \mathbf{E} is observed to be linear and hence, the two quantities are proportional. If the investigated sample is large enough to be considered homogeneous, the constant of proportionality is independent of position. In the limit of a linear, isotropic and time-invariant response the relations of relevant material's properties reduce to:

$$\mathbf{D} = \epsilon^* \mathbf{E} \quad (2.3)$$

and

$$\mathbf{J}_c = \sigma^* \mathbf{E} \quad \text{or} \quad \mathbf{E} = \rho^* \mathbf{J}_c, \quad (2.4)$$

where ϵ^* is the dielectric permittivity, σ^* the electrical conductivity and ρ^* its reciprocal value electrical resistivity. Equation 2.4 is known as Ohm's law. The electrical conductivity and hence the resistivity, can only be considered real if the relation between \mathbf{J}_c and \mathbf{E} is completely independent of time, which is almost never observed for anything other than electronic components. In other words, for a time dependent electric field, the current density and dielectric displacement at a particular time t are not merely a function of the actual field, but may also be influenced by polarization phenomena due

to former field values. A much more general description of the relation of electric field and resulting currents, therefore, considers the proportionality constants to be complex functions of frequency (Pelton et al., 1983). As \mathbf{D} , \mathbf{J}_c and \mathbf{E} are vectors then, in general ϵ^* , σ^* and ρ^* are non-linear tensor functions, that depend on temperature and pressure. However, for the sake of simplicity and since all materials investigated within the scope of this thesis can be treated as linear, homogeneous and isotropic, they reduce to scalar functions of the angular frequency. In this case they are real material constants.

$$\mathbf{D}(\omega) = \epsilon^*(\omega)\mathbf{E}(\omega) \quad (2.5)$$

Considering a time-dependent electric field $\mathbf{E}(t) = \mathbf{E}_0 e^{i\omega t}$, where $i = \sqrt{-1}$, $\omega = 2\pi f$ is the angular frequency and f the technical frequency, and differentiating eq. 2.2 with respect to time yields the relationship between displacement current density and electric field as follows:

$$\mathbf{J}_d(\omega) = i\omega\epsilon^*(\omega)\mathbf{E}(\omega). \quad (2.6)$$

This means that, in general, Maxwell's second law (eq. 2.1) in the frequency domain must be written:

$$\mathbf{J}_T(\omega) = \sigma^*\mathbf{E}(\omega) = [1/\rho^*(\omega) + i\omega\epsilon^*(\omega)]\mathbf{E}(\omega), \quad (2.7)$$

with the total current density \mathbf{J}_T being:

$$\mathbf{J}_T(\omega) = \nabla \times \mathbf{H}. \quad (2.8)$$

The term relating current density and electrical field strength in eq. 2.7 is called an electrical transfer function (Olhoeft, 1985). Both dielectric permittivity as well as electric conductivity are complex and frequency dependent, and consequently they can be written as:

$$\epsilon(\omega)^* = \epsilon'(\omega) - i\epsilon''(\omega) \quad \text{and} \quad \sigma(\omega)^* = \sigma'(\omega) + i\sigma''(\omega) \quad (2.9)$$

where $\epsilon'(\omega)$ and $\sigma'(\omega)$ are real and $\epsilon''(\omega)$ and $\sigma''(\omega)$ imaginary parts, respectively.

It is worth noticing, that all polarization phenomena can be explained by dielectric permittivity entirely omitting out-of-phase (imaginary) conductivity. However, other authors have shown that, if this is done, the dielectric permittivity must be larger than 10^8 to produce phase angles of 10 mrad in $100 \Omega m$ materials at 100 Hz. Pelton et al. (1983) state that this would physically require a charge separation by distances of the order of centimeters rather than the order of angstroms and that any charge that is able to travel such large distances is more appropriately called *free* instead of *bound*. By defining free and bound charges and restricting bound charge to the order of angstrom displacements,

the dielectric constant is effectively limited to values between 1 and 80. Hence, the effect of displacement currents is usually ignored measuring at frequencies less than 10^5 Hz.

2.1 CR parameter and related quantities

Complex resistivity instruments measure the resistivity magnitude and phase. When these measurements are made as a function of frequency, they are called spectral induced polarization (SIP) or electrical impedance spectroscopy (EIS) measurements. Typically the frequency range of SIP measurements is from 1mHz to 1kHz. The resistivity magnitude and phase shift (Fig. 2.1) of a sample are recorded relative to a reference resistor upon stimulus with an alternating current.

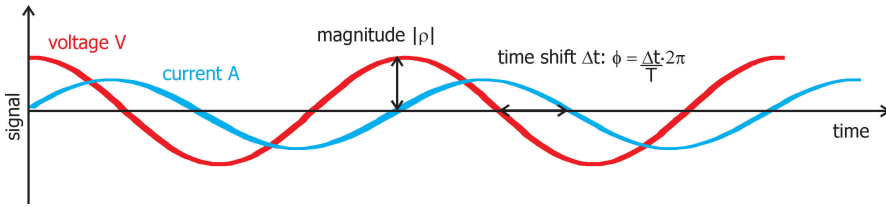


Figure 2.1: Complex resistivity signal for a distinct frequency. The applied voltage (V) causes a subsequent current (A) signal, which is shifted in time. The amplitude ratio of the two signals is the resistivity magnitude (Ωm due to geometrical considerations of sample diameter and length) and their time shift is related to as phase angle ϕ (mrad or deg).

Usually results are presented in terms of magnitude ($|\rho|$) and phase (ϕ), these parameter are related to real (ρ') and imaginary (ρ'') component of resistivity as follows:

$$\rho^* = |\rho|e^{i\phi} = \rho' + i\rho'' = \frac{1}{\sigma^*}, \quad (2.10)$$

$$|\rho| = \sqrt{\rho'^2 + \rho''^2}, \quad (2.11)$$

$$\phi = \arctan \left[\frac{\rho''}{\rho'} \right]. \quad (2.12)$$

Results may also be presented in terms of conductivity, the reciprocal value of resistivity. It is important to note, that the real component (or in-phase, energy loss) represents ohmic conduction, whereas the imaginary component (or out-of-phase, energy storage) represents the much smaller polarization term. In practice σ^* and ρ^* are derived from the measured resistance R of a sample:

$$\rho^* = R \frac{A}{L} \quad (2.13)$$

where the ratio A/L is the geometric constant of a sample with sides of length L , which are perpendicular to faces of area A .

Although the bulk and surface conduction (σ_{bulk} and σ_{surf}) mechanisms do not strictly act in parallel (e.g. Lesmes and Friedman, 2005), a simple parallel-model, as shown in Fig. 2.1 has several advantages. One major advantage is that the formation factor, F , as well as the surface conductivity of a material may be estimated very easily from a linear plot of the effective medium conductivity σ_{bulk} versus fluid conductivity σ_w . F , which is an intrinsic measure of a formation, is then just the inverse slope of the linear portion of σ_{bulk} versus σ_w at high fluid conductivities and σ_{surf} can be estimated from the extrapolated y-intercept at zero fluid conductivity (Waxman and Smits, 1968; Lesmes and Friedman, 2005).

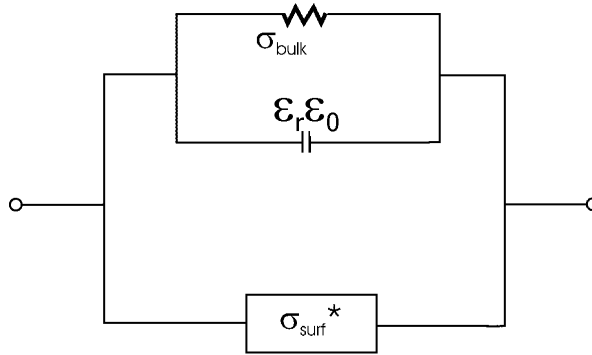


Figure 2.2: Equivalent circuit for the electrical response of rocks and soils after Lesmes and Frye (2001). Electrolytic conduction in the bulk pore is assumed to be purely resistive, the high frequency dielectric constant ϵ_r represents the high frequency dielectric constant, and σ_{surf}^* is the complex conductivity.

$$\sigma_{bulk} = \frac{\sigma_w}{F} + \sigma_{surf}. \quad (2.14)$$

Waxman and Smits (1968) obtained an empirical model based on their measurements on shaly sands, that takes the effects of lithology and solution chemistry into account to compute the surface conductivity:

$$\sigma_{surf} = \frac{BQ_v}{F}, \quad (2.15)$$

where B is the equivalent ionic conductance and Q_v is the cation exchange capacity per unit volume. B is strongly dependent on the fluid chemistry. Sen et al. (1988) developed a modified Waxman-Smits-model, in which the empirical parameter B is only a function of the solution conductivity σ_w and the cementation index M :

$$B = \frac{1.93M}{1 + 0.7/\sigma_w}. \quad (2.16)$$

Theoretically an effective medium theory has to be used to describe the complex electrical properties of porous media. Even though it is very likely that it does not satisfy

the true electrical mechanisms, according to Lesmes and Frye (2001) a more simplistic alternative is to model bulk and surface conductivity mechanisms as parallel conduction paths (Wyllie and Southwick, 1954; Waxman and Smits, 1968; Vinegar and Waxman, 1984). Using an equivalent circuit as shown in Fig. 2.1, the complex conductivity response of the sample is given by:

$$\sigma^* = [\sigma_{bulk} + \sigma'_{surf}(\omega)] + i[\omega\epsilon_r\epsilon_0 + \sigma''_{surf}(\omega)], \quad (2.17)$$

with ϵ_r the high frequency dielectric constant and ϵ_0 the permittivity of free space. At low frequencies, where CR phenomena are typically measured, $\omega\epsilon_r\epsilon_0 \ll \sigma_{surf}(\omega)$ and the low frequency complex conductivity response of a sample reduces to:

$$\sigma^* = [\sigma_{bulk} + \sigma'_{surf}(\omega)] + i\sigma''_{surf}(\omega). \quad (2.18)$$

The quadrature conductivity is only a function of the surface conductivity, whereas the real conductivity is a function of both the bulk and the surface conductivity mechanisms (Fig. 2.1). The bulk properties are independent of frequency. However, the complex surface conduction term σ^*_{surf} is frequency dependent. At very low frequencies the real component of the surface conductivity approaches a constant value $\sigma_{surf}(dc)$:

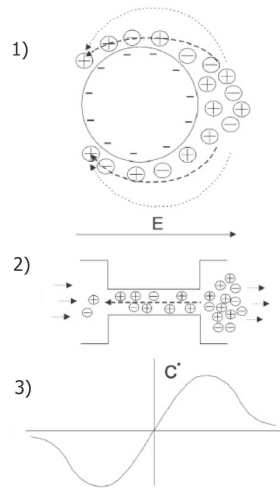
$$\lim_{\omega \rightarrow \infty} \sigma'_{surf}(\omega) = \sigma_{surf}(dc) = \frac{e\mu_s\Sigma_t S_0}{f}, \quad (2.19)$$

where e is the electronic charge, μ_s is the effective surface ionic mobility, Σ_t the mineral surface charge density, S_0 a weighted surface-to-volume ratio, and f is a geometric factor characterizing the tortuosity of the surface, which is similar, but not necessarily equal to the formation factor (Lesmes and Frye, 2001; Revil and Glover, 1998). For higher frequencies the real and imaginary part of the surface conductivity increase.

2.2 Electrochemical polarization

Conrad Schlumberger first noted that when an electrical field is applied to the Earth, it changes the charge distribution over various time scales that cause an imaginary or quadrature voltage response, similar to the charge up effect of a capacitor. This phenomenon was called induced polarization (IP) and could be observed in the time domain as well as later in the frequency domain. Historically, IP methods have been used mostly to explore for metallic ore deposits. However, it has been observed, that as well non-metal-bearing, ion-conductive and SiO_2 based materials have significant IP responses, which can be of reasonable value to access structural and perhaps chemical characteristics (Titov et al., 2004; Kemna et al., 2004; Lesmes and Friedman, 2005). In this thesis rather the term complex conductivity or CR will be used than IP, however, both terms describe to the same phenomenon. Ohmic conduction in non-metallic rocks is ionic, occurring through the pore-filled electrolyte and by ion migration in the EDL forming at the grain-fluid interface. The macroscopic conductivity of a saturated or partially saturated

Figure 2.3: Schematic of ion-conductive zones in porous rocks after Titov et al. (2004). (1) Excess and deficiency in ion concentration around a polarized spherical negatively charged particle. The solid arrow shows the direction of the electrical field, the dotted shows the diffusion flow of both, anions and cations and the dashed arrow shows the local diffusion flow near the surface mostly by cations. (2) Excess and deficiency along a polarized pore throat. (3) Schematic distribution of the ion concentration around a polarized spherical particle or along a polarized pore throat. C^* denoted the excess concentration produced by the polarizing field.



porous medium with insulating grains is the superposition of two mechanisms: a bulk conduction due to the migration of ions in the interconnected pore space and a surface conduction, which corresponds to electrical conduction in the vicinity of the fluid/grain interface. When such material is subject to an external electric field, ion diffusion takes place leading to charge excess and deficiency in ion concentration. In metal- and clay-free materials polarizations occur due to tangential ion displacement in the electrical double layer on the water-wet surface. In other words ionic mobility contrasts either within the EDL or at the interfaces between wide and narrow ("selective") pores are considered to be the predominant cause. A schematic distribution of the ion concentration after application of a polarizing electric field is shown in Fig. 2.3. Marshall and Madden (1959) recognized that two main causes of low-frequency induced polarization exist and they classified these as electrolytic polarization and electrode polarization .

Electrolytic polarization is considered to be due to various ion diffusion processes. Marshall and Madden (1959) proposed that this electrolytic polarization was mainly membrane polarization caused by ion selective zones in the rock, which reduce the mobility of either the positive or negative ions in the pore-fluid, causing charge to build up. It has often been postulated since that these membranes could possibly be caused by clouds of ions around clay particles and pore walls (Telford et al., 1990), but Marshall and Madden (1959) did not specify the exact cause of these membranes within a rock. A representation of the concepts of membrane polarization as given in Dukhin and Shilov (1974) is depicted in Fig. 2.3. Membrane polarization is generally much weaker than electrode polarization. Charges are dragged around a charged particle or accumulated at pore restrictions and relax back, when the polarizing field is switched off or changes its direction.

Electrode polarization occurs in ore containing rocks and is due to charge build up at the faces of the metallic minerals, where the electric current transmission changes from

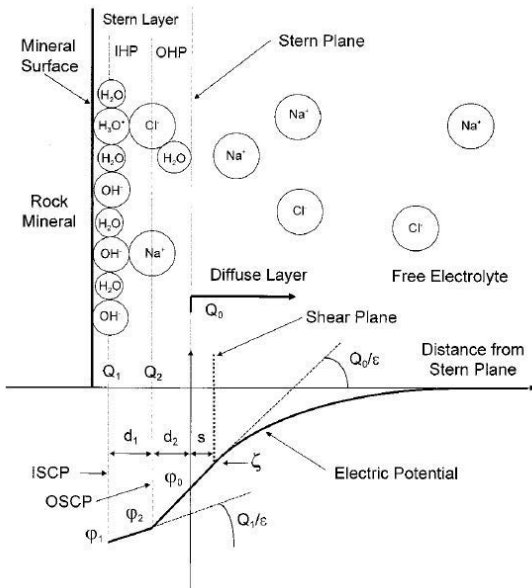


Figure 2.4: Three layer model of the electrical double layer as shown in Lorne et al. (1999). IHP: Internal Helmholtz plane; OHP: outer Helmholtz plane; ISCP: internal surface charge plane, OSCP: outer surface charge plane. The zeta-potential is defined as the electric potential at the shear plane, located at a distance s from the Stern plane.

electrolytic, in the pore fluid, to electronic in the conductive mineral. Minerals producing significant polarization are mostly those containing sulfides or magnetite.

The building materials that are examined within the course of this work do not contain considerable amounts of ore mineralizations. If polarization is observed, these effects will most likely be due charge separations in the bulk and/or mobility contrasts at the fluid/grain interface.

2.2.1 Electrical double layer

The formation of an electrical double layer at interfaces is a general phenomenon. In the interface the cohesion forces binding the individual particles together in the bulk of each condensed phase are significantly reduced. Particles that had a certain number of nearest neighbors in the bulk have a smaller number of such neighbors at the interface, where particles from the other phase become new neighbors.

The electrical double layer is divided into three regions that interact only electrostatically, i.e. the matrix, the fixed layer (or Stern layer) and the diffuse layer. A picture of an EDL is given in Fig. 2.4. Both the fixed and the diffuse parts of the electrical double layer (EDL) are polarized when subject to an external electrical field. According to Lesmes and Frye (2001) the relative contribution of the two regions of the EDL to the overall electrochemical polarization of the particle is primarily determined by the relative amounts of charge in each of them.

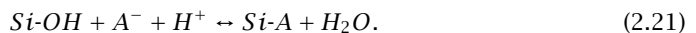
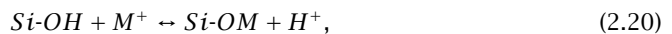
2.2.2 Surface chemistry

Recently considerable research has been done on the possible length scale of the observed polarization phenomena and the actual polarization mechanism involved (Scott, 2006, and the citations therein). Two main theories evolved: Lesmes and Frye (2001), Scott and Barker (2005), Chelidze and Gueguen (1999) and Ulrich and Slater (2004) argue that a charge build-up occurs caused by the excess of ions moving at different speeds in the double layer along the surface of the grains. There are others (Titov et al., 2002) who argue that, on meeting a pore restriction (pore throat), ions in the fluid encounter varying resistances to their movement causing charge build-up.

Even though there is no universal model recent publications make it seem more likely to assume that polarization is dominated by contrasts in ionic mobility in the EDL rather than membrane polarization as a result of ion slowdown at pore throats. Lesmes and Frye (2001) conclude from effective medium simulations that the diffuse layer polarization is likely to have a negligible effect relative to the fixed layer polarization upon the electrical impedance of Berea sandstone. Scott (2006) investigated the change in CR behavior after saturating sandstone samples with agar gel instead of water while keeping the ionic strength constant. These samples did not show major changes in their specific polarization behavior, even though the mobility of the ions in the bulk pore fluid was reduced dramatically by the gel. Assuming that the gel did not affect the properties of the EDL as much, this adds weight to the argument that the electrical double layer at the wet matrix is where polarization originates.

The electric double layer is formed due to the presence of static charges on the inner surfaces. Generally a dielectric surface charges when it is in contact with a polar medium by chemical reaction, ionization or ion absorption. This influences the distribution of ions in the bulk solution. Silica and other quartz based materials usually have negatively charged inner surfaces, when saturated with fluids at $\text{pH} > 3$. That is due to the equilibrium constants of the protonation and deprotonation reactions of silanol groups (a brief description is outlined in chapter C in the appendix). The equilibrium state of these reactions and the resulting surface charge density depends on the concentration of H^+ ions. All brines that have been used as saturating fluids in the experiments here had pH values between 7 and 12 (appendix Fig. C.5). As a consequence, positive ions in the liquid get attracted to the wall, whereas negative ions get repelled from it.

However, this simple picture is complicated by other ions than H^+ from the electrolyte, that also participate in the surface absorption (Fig. 2.4). For example, for a salt MA the following chemical reactions have to be considered (Davis et al., 1978; Lorne et al., 1999):



Because the adsorbed ions M^+ and A^- have a finite size (Fig. 2.4), they will actually generate a charge density Q_2 which is located at a distance d_1 from the plane of charge density Q_1 and at a distance d_2 from the Stern plane. Such charge distribution results in the assumption of a three layer model as first outlined by Davis et al. (1978). However, according Revil and Glover (1998) the Stern layer can be assumed somewhat simpler as just one region of fixed ion absorption. Following this idea, the electrical double layer is divided into three regions that only interact electrostatically: the matrix, the fixed (or Stern) layer and the diffuse layer. Both the fixed and the diffuse part of the EDL are polarized when subject to an external electrical field. In such materials net surface conduction is characterized by the sum of three contributions (e.g. Revil and Glover, 1998): (i) conduction within the electrical diffuse layer, which makes a negligible contribution to the total specific surface conduction. (ii) conduction in the Stern layer, which varies significantly with the salinity of the pore fluid at low salinities (10^{-6} - 10^{-3} mol/L), but becomes independent of salinity at higher salinities. (iii) a mechanism operating directly on the mineral surface, independent of salinity, and perhaps associated with proton transfer. Moreover Revil and Glover (1998) state that at salinities higher than 10^{-3} mol/L at 298° K the specific surface conductance of quartz is equal to $8.9e10^{-9}$ S.

From the publication of Revil and Glover (1998) mentioned earlier and according to Lesmes and Morgan (2001) it can be deduced that the two parameters, that define the surface chemistry are the surface charge densities in the diffuse (Σ_d) and the fixed part (Σ_f) of the EDL, respectively. These charges are in balance with the total charge Σ_t that is on the solid surface of the grains themselves. Σ_t varies with ionic strength of the solution and pH. Σ_d and Σ_t can be inferred from electrochemical measurements, Σ_f is taken to be their difference:

$$\Sigma_t = \Sigma_f + \Sigma_d. \quad (2.22)$$

However, up to the present publications on surface chemistry properties of building stones are unknown to the author. The total surface charge Σ_t can be measured by potentiometric titration. The surface charge density in the diffuse part of the EDL can be computed from zeta-potential experiments (James and Parks, 1982):

$$\Sigma_d = -\sqrt{8k_B T \epsilon_r \epsilon_0 n^0} \sinh\left(\frac{ze\zeta}{2k_B T}\right), \quad (2.23)$$

where n^0 is the concentration of each ion in a symmetric electrolyte, z is the ionic charge, ϵ the dielectric permittivity and ϵ_0 the dielectric permittivity of a vacuum, ϵ_r the dielectric constant, k_B the Boltzmann's constant, T the absolute temperature and the ζ the zeta-potential. This equation is valid, when the thickness of the double layer (Debye length) is small relative to the radius of the curvature of the particle. The Debye length ($1/\beta$) is given by:

Table 2.1: Debye lengths β in [nm] at various concentrations of aqueous solutions at 298 ° K according to eq. 2.27. The charge type of the electrolyte is given as charge of the cation dash charge of the anion in the headerline.

c [mol/L]	charge type of the electrolyte	
	1-1	1-2
10^{-5}	96.1	55.5
10^{-4}	30.4	17.5
10^{-3}	9.61	5.55
10^{-2}	3.04	1.75
10^{-1}	0.96	0.56
1	0.30	0.18

$$\beta = \sqrt{\frac{2n^0 z^2 e^2}{\epsilon \epsilon_0 k_B T}} \quad \text{or} \quad \beta = \sqrt{\frac{N_A e^2 I}{\epsilon \epsilon_0 k_B T}}. \quad (2.24)$$

The Debye length is directly proportional to the square root of the ionic strength of the electrolyte solution being

$$I = \frac{1}{2} \sum_i z_i^2 c_i \quad (2.25)$$

and for water at 298 ° K:

$$\beta = 9.6223 \times 10^{-9} I^{-0.5} \quad \text{m}, \quad \text{or} \quad (2.26)$$

$$\beta = 0.30428 I^{-0.5} \quad \text{nm}. \quad (2.27)$$

Equation 2.26 is valid for basic SI units (that is I in mol/m^{-3} , β in m), whereas eq. 2.27 (I in mol/L , β in nm) is more practical. Some illustrative values of the Debye lengths at different salt concentrations (ionic strengths) are tabulated in Table 2.1. In Fig. 2.5 the Debye screening length is shown as a function of salt concentration for the four salts that have been used as deterioration agents in this study. For the salt concentrations used in this work the thickness of the EDL is on the order of 0.01 to 0.3 μm and hence, too narrow to block pore throats of around 5 to 80 μm . However, to be able to explain, why the controlling factor in CR properties should be the pore throat when polarization is dominated by EDL ion diffusion, it is suggested in Scott and Barker (2003) that the contribution of the surface conduction is greater in the throat simply because of their relative size in it.

Generally, as ionic strength increases, the double layer thickness will become compressed, resulting in a decreased zeta-potential and reduced electroosmotic flow. The

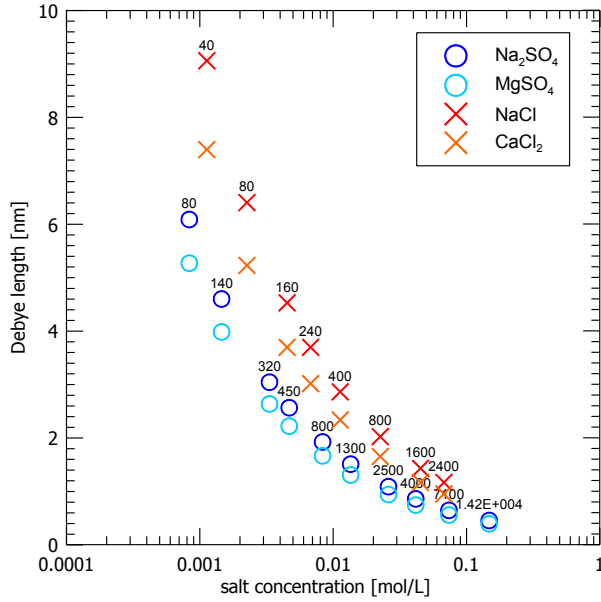


Figure 2.5: Debye lengths as a function of salt concentrations for Na_2SO_4 and $NaCl$ (monovalent cations) and $MgSO_4$ and $CaCl_2$ (divalent cations). The Debye length of salts with monovalent cations are larger compared to salts with divalent cation at the same concentration. Black labels denote the salt concentrations in units of parts per million (ppm).

ionic strength of the solution is the most important parameter in determining such properties of the component ions as their activities and mobilities (Oldham and Myland, 1994). The mobility μ_i of an ion i measures how easily it responds to an electric field. Similarly the diffusivity D_i measures how easily that ion responds to a concentration gradient. Nernst-Einstein's law describes the relationship between these two transport parameters as follows:

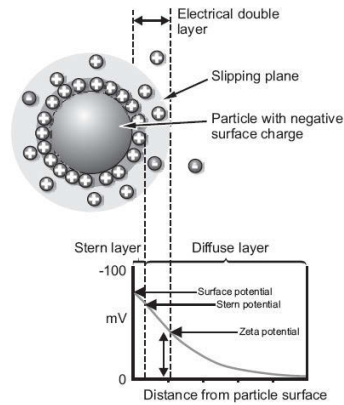
$$\mu_i = \frac{|z_i|e}{k_B T} D_i. \quad (2.28)$$

Ion mobilities are usually given in [$m^2V^{-1}s^{-1}$], which is plausible, when regarded to as quotient of an ion's velocity and the strength of the electrical field it is moved by. Though eq. 2.28 is exact only for a solute ion at extreme dilution, this law provides a useful approximation at higher concentrations too (Oldham and Myland, 1994).

2.3 Zeta-potential and electrokinetic phenomena

A solid particle, that is brought into contact with a liquid phase, develops a net surface charge. This surface charge may derive from a variety of mechanisms, such as the dis-

Figure 2.6: The liquid layer surrounding the particle exists as two parts: an inner region (Stern layer), where the ions are strongly bound and an outer (or diffuse) region, where the ions are less firmly attached. When a particle moves, ions within a notional boundary of the diffuse layer will move with it, any ions beyond this boundary do not travel with the particle. This boundary is the surface of hydrodynamic shear or slipping plane. The electrical boundary at this plane is referred to as the zeta-potential.



sociation of ionic surface groups, the absorption of charged material from solution, or unequal dissolution of ions from an ionic crystal lattice.

The charge separation at the interface of particle and liquid gives rise to several dynamic or so called electrokinetic phenomena, such as electrophoresis, electroosmosis, streaming potential and sedimentation potential. The driving force of all these phenomena has been found not to be truly the surface charge per se, but rather the net charge of the liquid that is hydrodynamically bound between the particle surface and the rest of the fluid (Matec Applied Science, 2006). This area of interface is called slipping or shear plane and the potential at this interface is the zeta-potential (Fig. 2.6).

When a colloidal dispersion is exposed to an alternating electrical field, the zeta-potential of the particles will cause them to oscillate. It follows, that if there is a density difference between the particles and the liquid, this oscillation will generate a momentum to the liquid and trigger an acoustic wave. One way to measure this acoustic wave is the measurement of the Electrokinetic Sonic Amplitude (ESA), which is the pressure amplitude generated by the colloid per unit electric field strength. ESA has SI units of Pascals per volt per meter and is analogous to electrophoretic mobility, which is particle velocity normalized by the applied electric field.

The zeta-potential is proportional to the charge on the capillary wall, which itself is pH dependent. Therefore, the electroosmotic flow (EOF) mobility will vary according to the buffer pH, such that at high pH of the EOF mobility will be significantly greater than at low pH.

The binding constants for cation adsorption on quartz are not well known. In their paper on the *Theory of zeta potential* Revil et al. (1999) state with reference to Scales et al. (1990), that the electrokinetic behavior of silica is likely to be very similar to the one of muscovite, for which data could be obtained. They follow, that the sorption of cations upon the surface of silica, mica and aluminosilicates is primarily controlled by the ionic

charge and the hydrated radii (ions with smaller hydrated radii are sorbed more strongly). This implies, that monovalent cations, that are adsorbed on the surface of silica grains, will generally be replaced by divalent or trivalent cations. Ions with large hydraulic radii are replaced by this with smaller ones (Revil et al., 1999, and citations herein). At 25° C, for monovalent ions, the selectivity or binding energy sequence is:

$$Li^+ \sim Na^+ < K^+ < NH_4^+ < Rb^+ < Cs^+ \quad (2.29)$$

(weakest < strongest binding)

Also Revil and Glover (1998) report a similar but reverse sequence for the surface mobility β_s of adsorbed cations:

$$Li^+ \sim Na^+ > K^+ > NH_4^+ > Rb^+ > Cs^+ \quad (2.30)$$

(highest mobility < lowest mobility)

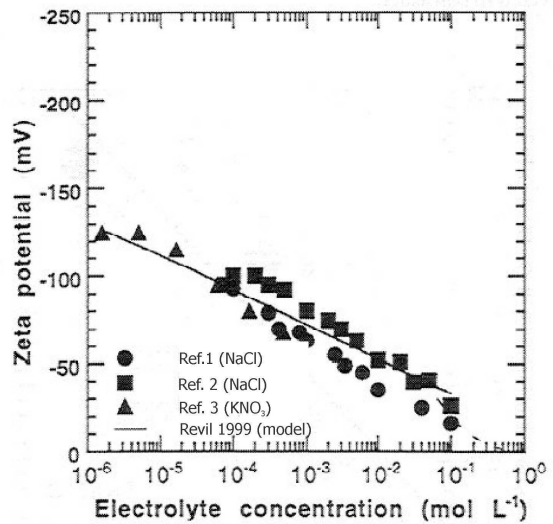
This observation is contrary to what would have been expected if the hydration status of cations at the mineral surface would be similar to the hydration state in aqueous solution. Surface mobilities are not correlated to hydrated radii of ions. However, a slight but positive relation between surface mobilities and crystalline radius is found, which could indicate a modification of the hydration status of adsorbed cations in the Stern layer.

Revil et al. (1999) and Pride and Morgan (1991) both investigated the variation of ζ and Σ_t with salinity for quartz. The former state, that at pH 7 and for Na^+ , the gradient of the zeta-potential with logarithm of fluid salinity is independent of surface site density and the surface site dissociation constant, but only depends on temperature. Their model predictions are in fairly good agreement with the available empirical results. They state, that at 25°C the gradient is ≈ 20 mV per tenfold change in the concentration of a 1:1 monovalent electrolyte. Figure 2.7 compares the prediction of a model developed by Revil et al. (1999) and analytical zeta-potential measurements at various electrolyte concentrations.

Table 2.2: Ion mobilities at extreme dilution in aqueous solution at 298 K. (after Oldham and Myland (1994))

cation	$\mu_i [m^2 s^{-1} V^{-1}]$	anion	$\mu_i [m^2 s^{-1} V^{-1}]$
H^+	362.5×10^{-9}	OH^-	204.8×10^{-9}
K^+	76.2×10^{-9}	Cl^-	79.1×10^{-9}
Na^+	51.9×10^{-9}	SO_4^{2-}	82.7×10^{-9}
Mg^{2+}	55.0×10^{-9}		
Ca^+	21.4×10^{-9}		

Figure 2.7: Variation of the ζ -potential with electrolyte concentration measured for silica surfaces and 1:1 electrolyte. Source: Revil et al. (1999). Results of different publications are plotted: Ref.1: Gaudin and Fuerstenau (1995), Ref.2: Li and de Bruyn (1966), Ref.3: Watillon and de Backer (1970), as well as the model prediction of Revil et al. (1999).



2.4 Interpretation of CR data

2.4.1 Relaxation models

Every charge separation is called polarization absolutely independent from its scale of occurrence. Going from small to large some of the main polarization causes are the shifting of electric fields around individual atoms, the realignment of dipolar molecules and ionic diffusion. These different processes act at different speeds when an electric field is applied. It takes a finite time after the application of an electric field for the charges to realign or redistribute themselves and a finite time for the charges to return to equilibrium after cessation of that field. This time is known as a relaxation time. When an alternating sinusoidal field is applied with a period much longer than a particular relaxation time, that process will seem to happen almost instantaneously, and not contribute to the out-of-phase response. When the period is much shorter than the relaxation time, then there will be no significant charge movement and therefore no contribution to the out-of-phase response. When the period is the same as the relaxation time, then there will be a maximum out-of-phase response. A polarization with a single relaxation time, τ , and an exponential decay can be characterized by a classic Debye relaxation (Pelton et al., 1983):

$$\epsilon^* = \epsilon_\infty + \frac{\epsilon_s - \epsilon_\infty}{1 + (i\omega\tau_D)}. \quad (2.31)$$

This relaxation has a maximum energy dissipation, or out-of-phase response, at a critical frequency $f_c = 1/2\pi\tau_D$. The loss peak is symmetric with a half width of 1.14 decades (Kremer and Schönhal, 2003). However, in most cases the half width of measured loss peaks is much broader than predicted by the Debye relaxation and moreover their shape is asymmetric. This is called a non-Debye relaxation behavior. The most important models, which has been proposed to describe non-Debye resistivity and dielectric spectra will be discussed in the following.

Cole-Cole family of models All mathematical models that have been used to describe CR spectra share three main features: there is a low frequency asymptote, a dispersive region and a high frequency asymptote. The dispersive region is considered to be centered around a typical frequency, which can be related to a particular relaxation time, τ . However, for heterogeneous media the classical Debye relaxation is observed to be only a simplification. A broadening of the response function can be described by the sum of many relaxation times with a log normal distribution according to the Cole-Cole model:

$$\epsilon^* = \epsilon_\infty + \frac{\epsilon_s - \epsilon_\infty}{1 + (i\omega\tau)^{1-\alpha}} - i\frac{\sigma_s}{\omega}, \quad (2.32)$$

where α is the distribution function exponent (Cole and Cole, 1941). Additional exponents can be added to make the function asymmetrical. Following Pelton et al. (1983) the complex electrical behavior of most earth materials can be best described using modified, however, Cole-Cole like impedance models. All common mathematical expression

that belong to this impedance Cole-Cole family are listed in Table 2.3. The most general model is presented on the very bottom and all others are simplifications or special cases. The generalized Cole-Cole model becomes the Cole-Davidson model when $c = 1$ and becomes the Cole-Cole model when $a=1$. The case $c = 0.5$ is called Warburg model after the $(i\omega)^{-0.5}$ behavior of Warburg impedances; and finally when $c = 1$ the expression reduces to the common Debye model. Generally, the models can either be fitted as a single or a multiple set of relaxation terms. In terms of impedance eq. 2.31 becomes:

$$Z(\omega) = R_0 \left[1 - \sum_{k=1}^{k=n} m_k \left(1 - \frac{1}{1 + (i\omega\tau_k)^{c_k}} \right) \right] \quad (2.33)$$

where $Z(\omega)$ is the complex impedance, R_0 the dc-resistivity, ω the angular frequency of the polarizing current. m is the chargeability corresponding to the polarization immediately after the switch-off of the harmonic electrical field. It describes the magnitude of the polarization effect. At high frequency the resistivity magnitude has an asymptote of $R_0(1-m)$, whereas at low frequency the asymptote is simply R_0 . According to Lesmes and Frye (2001) the polarization magnitude is best represented by the normalized chargeability, m_{norm} , which is given by

$$m_{norm} = \sigma_{DC} * m. \quad (2.34)$$

τ is the time constant of the relaxation process and is an indication of the position of the peak, f_c , i.e. the frequency at which the phase peak reaches its maximum value:

$$f_c = \frac{1}{2\pi\tau(1-m)^{1/2c}}. \quad (2.35)$$

The model parameter c is a dimensionless exponent and gives the slope of the left (or right -c) hand side of the phase spectrum in a double logarithmic plot. The width of the dispersion increases as the value of c decreases. Generally, the phase angle of the complex resistivity depends only on m , τ and c and is completely independent of R_0 (Pelton et al., 1983).

A somewhat problematic aspect of using the Cole-Cole model to interpret impedance data is the fact that its parameters are mutually interrelated as can be seen from eq. 2.35 (Major and Silic, 1981). The peak position f_c shifts toward higher frequency when m increases. An experimental evidence of this has been given in Vanhala (1997), where the author states, that when m is large and c very small, the fundamental relationship $\tau \sim 1/(2\pi f_c)$ disappears.

Table 2.3: Overview of simple relaxation models after Pelton et al. (1983). The last two columns indicate the low and high frequency phase angle asymptotic slopes.

Name	Model function	$\omega \rightarrow 0$	$\omega \rightarrow \infty$
Debye	$R \left[1 - m \left(1 - \frac{1}{1+i\omega\tau} \right) \right]$	1	1
Warburg	$R \left[1 - m \left(1 - \frac{1}{1+(i\omega\tau)^{1/2}} \right) \right]$	0.5	-0.5
Cole-Cole	$R \left[1 - m \left(1 - \frac{1}{1+(i\omega\tau)^c} \right) \right]$	c	$-c$
Generalized Cole-Cole	$R \left[1 - m \left(1 - \frac{1}{((1+i\omega\tau)^c)^a} \right) \right]$	c	$-ac$

2.4.2 Constant Phase Model

For spectral induced polarization measurements that may not reveal variation in phase angle a simpler two parameter model may be used to fit the available data. For this reason the constant phase angle model is widely used. Börner observed a constant phase angle (CPA) behavior for clayey sandstones (Börner, 1992), gneisses and amphibolites (Börner et al., 1993) and similarly for clayey sands and silts (Börner et al., 1996). The CPA model can be written as:

$$\sigma^*(\omega) = \sigma'(\omega) + i\sigma''(\omega) \quad (2.36)$$

and

$$\sigma^*(\omega) = \sigma_0 \left(\frac{i\omega}{\omega_n} \right)^{1-p}, \quad (2.37)$$

where σ_0 is the magnitude of the complex conductivity measured at an arbitrary frequency, ω_n typically equivalent to 1 Hz, and p is the dispersion parameter. p describes both the phase angle $\phi = (1-p)\pi/2$ and the rate of change for the conductivity amplitude with increasing frequency. The CPA model has only two free parameters (σ_0 and p) and they can be obtained in one single complex electrical scan. From eq. 2.37 the relationship between the frequency exponent $(1-p)$ and the phase angle follows from:

$$\tan\phi = \frac{\sigma''(\omega)}{\sigma'(\omega)} = \frac{\sigma_0''}{\sigma_0'} = \tan \left[\frac{\pi}{2}(1-p) \right] \quad (2.38)$$

and

$$\phi = \frac{\pi}{2}(1-p). \quad (2.39)$$

In terms of real and imaginary parts, the CPA model can be written as:

$$\sigma'_0 = \sigma_0 * \cos \left[\frac{\pi}{2} (1 - p) \right]$$

$$\sigma''_0 = \sigma_0 * \sin \left[\frac{\pi}{2} (1 - p) \right]$$

with σ'_0 and σ''_0 being frequency independent quantities. Börner and Schön (1991) empirically found a linear link between the specific surface S_{por} and σ'' based on complex resistivity measurements on unconsolidated sediments:

$$S_{por} = b(\sigma''_{1Hz}),$$

where S_{por} is in μm^{-1} and σ''_{1Hz} is in S/m and $b = 10^{-11} S^{-1}$. The specific surface S_{por} is defined as:

$$S_{por} = \left[\frac{1 - \Phi}{\Phi} \right] S_M d_M, \quad (2.40)$$

where Φ is the porosity, S_M the surface area per mass [m^2/g] and d_M the grain density [g/cm^3] and, S_{por} therefore is in μm^{-1} . The surface area per matrix mass S_M can easily be measured using the nitrogen absorption (BET) method.

As stated, for example in Börner et al. (1996), retention properties of rocks can be characterized by the cation exchange capacity CEC of the silicate matrix. Knowledge of the imaginary component of the conductivity enables the estimation of CEC relative to the pore volume (CEC_{por}) directly from electrical measurements (Vinegar and Waxman, 1984). CEC_{por} is related to S_{por} by:

$$CEC_{por} = s S_{por}. \quad (2.41)$$

Using a Kozeny-Carman like equation Börner et al. (1996) were also able to derive information on the hydraulic permeability k of their unconsolidated materials, using:

$$k = \frac{a}{F S_{por}^b}, \quad (2.42)$$

where a and b are empirical constants and F is the formation factor, which will be explained in detail in the next section.

Generally it should be emphasized, that all the above mentioned empirical response functions lack supporting physical models: they are merely means of representing the behavior in terms of mathematical functions.

2.5 Water saturation

In the free pore space, where surface conduction is negligible, the parameters that govern the effective electrical conductivity are length, cross section and connectivity of the conduction paths. Archie's empirical law is the most widely used relationship for the

prediction of the effective electrical resistivity responses of water saturated (geological) materials (Archie, 1942):

$$\sigma_{bulk} = \frac{\sigma_w}{F}. \quad (2.43)$$

The resistivity formation factor F is an intrinsic measure of material microgeometry and related to grain shape and pore space topology. Moreover, F is often related to tortuosity T , which is for a curved as opposed to a straight pore (where pore length = sample length, T equals 1) defined as "path prolongation" after Winsauer and Shearin (1952):

$$T = \frac{length_{capillary}}{length_{sample}}. \quad (2.44)$$

Wyllie (1957) found tortuosity T and porosity Φ to be correlated by Archie's formation factor as:

$$T = \frac{a}{\Phi^M}. \quad (2.45)$$

If σ'_{surf} is negligible, i.e. for a high salinity pore fluid, low surface area or in clay-free rocks, the formation factor can simply be computed as the ratio of σ_w/σ_{bulk} . Archie termed the exponent M the cementation index as he found it increases with increasing cementation:

$$F = \Phi^{-M}. \quad (2.46)$$

Usually M ranges between 1.3 for unconsolidated sands to 2.0 for consolidated sandstones. Other authors related M to an effective grain shape and reported of increasing M values as the grain shape became less spherical (Jackson et al., 1978), while grain size was observed to have little effect.

Accounting for the non-linear relationship observed on many rock materials, Archie's law was modified introducing a surface conduction term in parallel with the bulk conduction, which refers to the migration of ions through the bulk pore solution (e.g. Schön, 1996):

$$\sigma_{eff} = \frac{\sigma_w}{F} + \sigma_{surf} \quad (2.47)$$

The effects of saturation on the conductivity responses was empirically found to enter according to the following power law:

$$\sigma_{eff}(S) = \sigma_w S^n + S^v \sigma_{surf} \quad (2.48)$$

Both conductivity components are dependent on water saturation (and salinity), however, not in the same way. Waxman and Smits (1968) specified firstly the reduction of

cross section area for conduction paths in the water phase and secondly the increasing concentration of counter ions near the grain-water interface. According to that, the saturation exponents of the interface term were expected to be less than the bulk conduction exponents. Neither an obvious correlation between the two nor to other intrinsic physical properties have been observed so far. It also has been shown by Ulrich and Slater (2004) for unconsolidated sands, that the saturation history like subsequent drying and imbibition cycles can effect the CR characteristics. Their evaporative as well as pressure drainage experiments verified, for unconsolidated sands having negligible clay content, that polarization is less affected by saturation than conduction. During evaporation the polarization magnitude approximates a power-law saturation dependence, which is consistently less than the equivalent conduction exponent. Neither one of the exponents was observed to correlate particularly to any lithologic property of the sample. Ulrich and Slater (2004) suggest instead, that fluid chemistry governs polarization during the desaturation process as opposed to lithologic properties.

The publication of Binley et al. (2005) gave evidence of how saturation changes Cole-Cole type spectra of sandstones. They observed the relaxation time τ to decrease one or two orders of magnitude between saturations of 100 - 25 %. Since bigger pores would dewater first, they related the τ altering to a decrease of the hydraulically effective pore throat size. The phase magnitude did not show any specific trend associated with reducing saturation. In contrast, Münch et al. (2006) reports the relaxation time τ to increase about one order of magnitude during desaturation of unconsolidated sands. Since for saturated media τ could be shown to closely correlate with hydraulic permeability k , this author hence hopes to be able to also deduce hydraulic permeability estimates for vadose soils.

3 Salt experiments

3.1 Experimental procedure

3.1.1 Sample selection and characterization

Laboratory samples were acquired from 21 different types of common building stones including both natural as well as fabricated materials. Sandstones and limestone were and still are widely used by builders. Obviously, any natural rock, even sometimes when obtained from the same locality, can inevitably differ in their properties because of variability in the composition and texture. So, three German sandstones as well as one French limestone were selected making sure, that these included some considerable petrophysical variety. In fact, man-made, industrially fabricated materials may not differ as largely in their chemical compositions and properties, but, there is broad diversity of stones available on the market. To constrain the number of experiments to manageable limitations, it seemed appropriate to include six sand-limestones, nine bricks (fired the historical way), and one aerated concrete to the program.

The petrophysical properties of the materials were investigated alongside to the actual CR studies. Table 3.1 lists all the properties, that were accounted for and the tests applied to measure them. The specific surface area S_{por} was measured using the nitrogen absorption BET method. Mercury injection capillary pressure (MICP) tests were analyzed to determine the pore size distributions including significant pore space parameter like the dominant pore throat size D_0 and porosity Φ . The dominant pore throat diameter was determined as the diameter, that corresponds to the pressure stage, where the differential intrusion of mercury into the sample was highest (compare Fig. A.1 in the appendix). The mineral content for materials (groups) was determined in X-ray diffractometry as well as the analysis of thin sections using a polarizing light optical microscope. A detailed description of the petrophysical investigations is given in the appendix in section A, page 119 ff.

3.1.2 Sample preparation

Cylindrical samples of 20 mm diameter and 70 mm length were extracted from larger stone blocks or bricks. These samples were dried (sandstones and limestone at 40°C to preserve the potential clay minerals inherent, other materials at 105°C) and then saturated under vacuum with brines containing Na_2SO_4 , $NaCl$, $MgSO_4$ and $CaCl_2$. According to restaurateurs five deterioration levels of salts in a building stone can be differentiated. These are tabled in Table 3.2. To cover the entire spectrum of damage states possible, the samples were saturated with varying concentrations from 0.8 to 140.0 mmol/L,

hence, ranging from "unloaded" to "highly loaded". A general summary of the physical characteristics and material/brine combinations realized is given in Table 4.1. For a more detailed list specifically outlining each sample/brine combination refer to Fig. C.1 in the appendix C.

All four salts are widely recognized as primary causes of irreversible damages of many modern and historical buildings. Two sodium salts Na_2SO_4 and $NaCl$ were chosen to study the effect of the different anions, while saturated explicitly with the same amount of salt. The same holds for $MgSO_4$ and $CaCl_2$, which have been included to investigate the role of the cation in the solution.

Before the electrical measurements were performed, it was waited for possible solving processes to take place. The conductivity of the solutions in the beakers, in which the samples were kept after saturation, was regularly checked. Only when no significant conductivity change was observable CR measurements were started assuming the samples reached some chemical equilibrium with the saturating fluid.

Table 3.1: Examination methods for the petrophysical and mineralogical characterization.

Method	Aim
BET-nitrogen absorption	specific surface
Mercury injection capillary pressure	dominant pore throat diameter
Scanning electron microscope (SEM)	grain texture
Light optical microscope (thin sections)	mineral phases and grain shape
X-ray diffractometry	mineral phases

Table 3.2: Deterioration levels of salts. Source: Arendt and Seele (2001)

Deterioration level	Sulfate in M.%	Chloride in M.%	Nitrate in M.%	concentration in mmol/kg
0 - unloaded	< 0.024	< 0.009	< 0.016	< 2.5
1 - low	< 0.077	< 0.028	< 0.05	< 8.0
2 - medium	< 0.24	< 0.09	< 0.16	< 25.0
3 - high	< 0.77	< 0.28	< 0.5	< 80.0
4 - very high	> 0.77	> 0.28	> 0.5	> 80.0

Table 3.3: Physical characteristics of the building material samples under investigation. The cross in the salt column marks those materials that were investigated in the salt concentration study. Abbreviations: AD - distilled water.

Short symbol	Material type	Φ [%]	S_{por} [μm^{-1}]	D_0 [μm]	AD	Na_2SO_4	Mg_3O_4	NaCl	CaCl_2
Pa	aerated concrete	71.89	54.81	75.17	x	x	x	x	x
S	sandstone	18.77	10.73	22.79	x	x	x	x	x
C	sandstone	21.70	50.80	18.25	x	x	x	x	x
B	sandstone	19.10	69.17	0.99	x	x	x	x	x
SV	limestone	34.00	3.36	3.02	x	x	x	x	x
K	sand-limestone	29.88	37.42	20.40	x	x	x	x	x
Ka	sand-limestone	31.10	25.77	28.38	x				
Kb	sand-limestone	26.49	19.89	0.02	x				
Kc	sand-limestone	25.04	23.96	0.02	x	x	x		
Kd	sand-limestone	29.60	22.57	28.34	x				
Ke	sand-limestone	33.18	20.42	20.41	x				
Ha	historic brick	25.16	5.19	3.41	x	x	x	x	x
Hb	historic brick	35.90	2.41	5.98	x				
Hc	historic brick	32.00	3.49	6.69	x				
Hd	historic brick	38.09	5.99	0.71	x	x			
He	historic brick	27.74	1.72	9.36	x	x	x	x	x
Hf	historic brick	31.90	5.66	7.48	x				
Hg	historic brick	32.68	3.69	8.37	x				
Hh	historic brick	32.91	9.21	7.49	x				
Hi	historic brick	37.08	1.35	10.47	x				
TOb	historic brick	23.13	6.78	4.77					
T	modern brick	18.01	4.99	1.24	x				
Mo	mortar	19.20	-	~ 1					
Ce	cement	16.87	-	~ 1					

3.1.3 Cell and impedance devices

Complex resistivity measurements were acquired in the frequency range of 1mHz - 1kHz. Four electrode measurements were made using two different measurement devices throughout the course of this thesis. Initially measurements have been made using a SIP 256c device in combination with remote reference units (Radic Research, 2007). The complex resistivity and phase shift are measured across a sample relative to a shunt resistor. The input impedance is $> 10^9 \Omega\text{m}$ to enable measurements also on highly resistive samples. The major part of the experiments, however, were obtained with a Solartron 1260 A Impedance/Gain-Phase Analyzer. The device had to be provided additionally with an operational amplifier, which uses a pre-amplification to increase the input impedance to approximately $10^9 \Omega\text{m}$ on the sensing leads (Analytical, 2007). All measurements were conducted in an environmental chamber at $298 \pm 0.5^\circ\text{K}$.

For minor polarizable samples, reproducibility can be problematic. Considerable effort was made into the design of a sample holder to permit accurate CR measurements of both saturated and unsaturated specimen. In case of unsaturated specimens it is difficult to maintain adequate electrode coupling and so contact resistances become substantial. Test measurements showed on different water, brine and agar gel samples, that phase errors may be significant. Unacceptable phase changes can arise from electrode wire sitting between the current electrodes, that is directly in the electric field of the sample. Placing the electrodes in fluid or gel filled chambers outside of the electric field significantly enhances the quality of the measurements. Consequently, the best sample holder geometry has been found a four-point set-up, where the current and potential electrodes are placed somewhat away from the sample. A sketch of the cell is shown in Fig. 3.1, a photograph and a detailed description can be found in the appendix (Fig. B.1). The results of a number of test measurements show that residual phase errors can arise from the cell itself, but can be considered negligible for frequencies below 100 Hz. The phase errors of this cell is in the order of $\pm 0.5 \text{ mrad}$ and depends somewhat on the coupling medium.

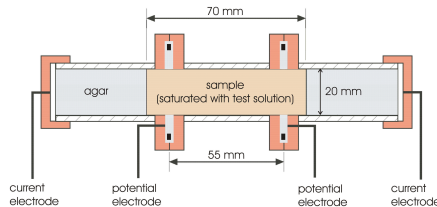


Figure 3.1: Scheme of the measurement cell used. As potential leads serve German Silver wires sitting in PVC chambers. As current electrodes were used stainless steel caps at the front and end of the cell. Electrodes were coupled either with agar gel or water to the specimen.

3.2 Material type

3.2.1 CR spectra

Figure 3.2 shows the phase spectra of the selected building materials saturated with distilled water (abbreviation used: AD, fluid conductivity prior to saturation $\sigma_w = 0.2$ mS/m). Some building materials show significant polarization effects, others do not. Sandstones, sand-limestones, aerated concrete or bricks are markedly to moderate polarizable having phases ranging from -12 to -2 mrad. Materials, that could not be found to have truly significant polarization are concrete and mortar.

Sandstones Figure 3.2 (top left) shows, how differently sandstones can behave upon saturation with distilled water. Bentheimer and Cottaer sandstone have clear phase peaks, Baumberger sandstone does not. Thin sections and Xray diffractometry results showed that clay minerals appear to be most abundant in Cottaer sandstone. Contrary to the Bentheimer, in Cottaer sandstone clay not only lines the pores, but also appears in broad intergranular bands. Baumberger sandstone must more appropriately be referred to as a siliceous marl, it has a very high calcite content (50-70%) and some quartz, that is cemented with illite, but no kaolinite and little, if any, montmorillonite. It has often been argued that those materials with very broad pore size distributions (PSD) would generate polarization along a large number of characteristic length scales (wide range of relaxation frequencies) and hence, probably have flat spectra as opposed to those where obviously one pore throat size dominates all the others. Looking at the PSD of the three sandstones here (Fig. A.1 (top) in the appendix) shows surprisingly, that Cottaer sandstones actually has a broad distribution of pore sizes, however, also has a peak in the phase spectrum. Bentheimer as well as Baumberger sandstones have only one very dominant pore size, however, the first has a clear phase peak and the latter a sloping and flat phase curve. This results indicate, that the size of the dominant pore may be crucial as well as the mineral content; if the dominant throat size happens to be very small, potentially no clear peak results.

Sand-limestones The complex resistivity responses of six sand-limestone samples saturated with distilled water are presented in Fig. 3.2 (lower left). Compared with the brick samples the phase angles are clearly higher and peak frequencies lower. According to the results of the MICP tests, the sand-limestones have bimodal pore size distributions (Fig. A.1 (center) in the appendix). One group of dominant pore throats has a diameter of about $20 \mu\text{m}$, whereas the other group is very small with only $0.02 \mu\text{m}$. Understanding that dominant pore throats have a strong influence on the peak frequency and basing on the correlation of the two, only the first group is expected to appear in the SIP frequency range. Assuming an extrapolation of the results can be done into the higher frequency range such very small pores are likely to generate polarizations at some MHz (compare Fig. 3.5).

Bricks Nine brick samples were saturated with distilled water, eight of which were fabricated the *historic way*, one sample is a modern brick. From Fig. 3.2 (lower right) it appears, that bricks generally have very low polarization effects and phase angles are usually found to be less than -5 mrad (absolute values) below 100 Hz. This is only about two or three times more than the measurement accuracy. Some bricks show Cole-Cole like phase maxima at frequencies around 1-2 Hz. Others have flat spectra, showing a constantly decreasing phase angle from 50 to 0.001 Hz. Pore size distribution analyzes for all bricks are given in Fig. A.1 (bottom) in the appendix.

Other materials Fig. 3.2 (top left) shows the phase spectra of distilled water saturated aerated concrete, limestone, mortar and concrete samples. Aerated concrete has a high porosity around 70% and pore throat sizes of 75 μm . Its CR curve possesses therefore its peak at very low frequencies, that is here 12 mrad around 0.01 Hz. The limestone sample has dominant pore throats similar to the bricks, however, a higher specific surface. Its CR phase spectrum is flat at -4 mrad. The mortar and concrete samples are not observed to be significantly polarizable. They have flat phase curves and maximum values below -2 mrad (absolute values).

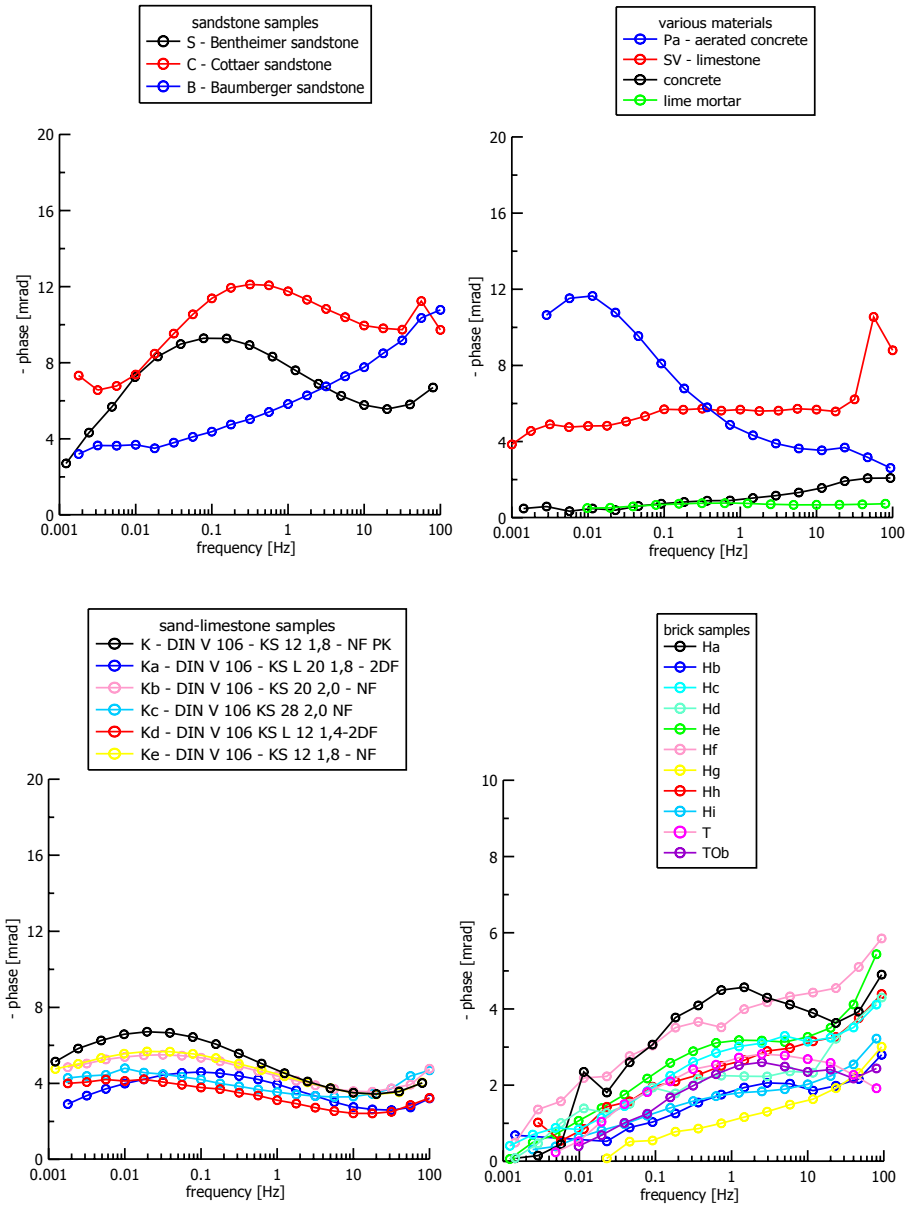


Figure 3.2: CR phase spectra of three different materials classes: Top left: sandstones, top right: aerated concrete, limestone, mortar and concrete, bottom left: sand-limestones, bottom right: historic and modern fired clay bricks. All samples were saturated with distilled water.

3.2.2 CR parameter and lithology

Many authors (e.g. Börner et al., 1996) have tried to establish a link between CR and electrical active interface is described by the surface-area-to-porosity ratio S_{por} . As the majority of the CR responses in this study did not conform to a constant phase angle behavior it seemed inappropriate to use a defined (arbitrary) frequency. So, as a representative measure of the CR spectra used here is the peak phase for each sample. Figures 3.4 and 3.3 prove the relationship between σ'' and S_{por} . Previous work has shown that σ'' is primarily controlled by the total specific surface area S_{por} within a sample (Börner and Schön, 1991; Börner et al., 1996; Slater et al., 2006), however, the investigated materials were mostly unconsolidated media. Scott (2003), Binley et al. (2005) as well as Breede (2006b), who all worked with consolidated sandstones, report for their samples only a weak correlation between S_{por} and σ'' . Latter authors mention the fluid chemistry may have substantial influences on this relation, too.

Scott and Barker (2003) show a convincing correlation of dominant pore throat D_0 and the frequency at which the peak phase angle occurs for a range of sandstones obtained from sites across the UK. For the building materials investigated here the position of the peak phase correlates inversely with the dominant pore throat size on a log-log scale, which is visualized in Fig. 3.5. It is also shown that the magnitude of the polarization (peak phase value) increases with increasing pore throat size (Fig. 3.6). As concretes and mortar usually have pore sizes in the 0.050 - 1 μm range (Neville, 1997), it seems very unlikely that these materials can be appropriately investigated with CR. This observation is supported by the results of other authors, for example Vanhala (1997), who correlated polarization with grain size. The present data indicate materials with pore sizes smaller than 10 μm will have polarizations less than -1 mrad (at low salt concentration) and thus, signal amplitudes may quickly fall below the detection limit.

The relation of dominant pore size D_0 and specific surface S_{por} and imaginary conductivity σ'' is illustrated in Fig. 3.7 and 3.8, respectively. Both diagrams indicate, that these parameters do not correlate strongly. In contrast to the data presented here, most natural Earth materials normally exhibit a clear inverse relationship between D_0 and S_{por} .

Figure 3.3: Imaginary component of the complex electric conductivity σ'' specific versus surface S_{por} as measured on building material samples saturated with distilled water and results of previous works by other authors.

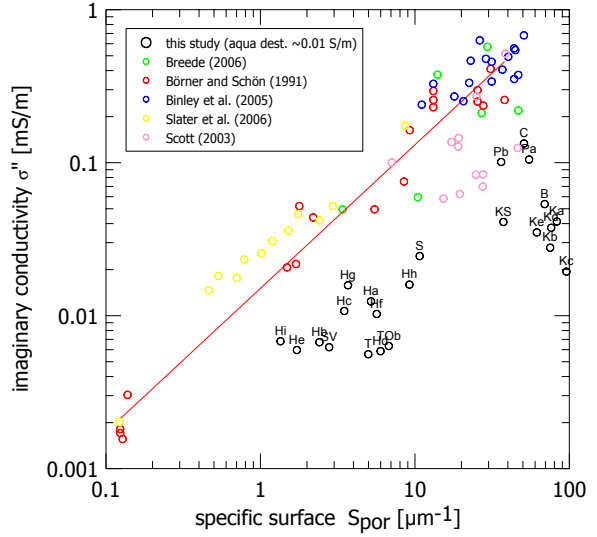
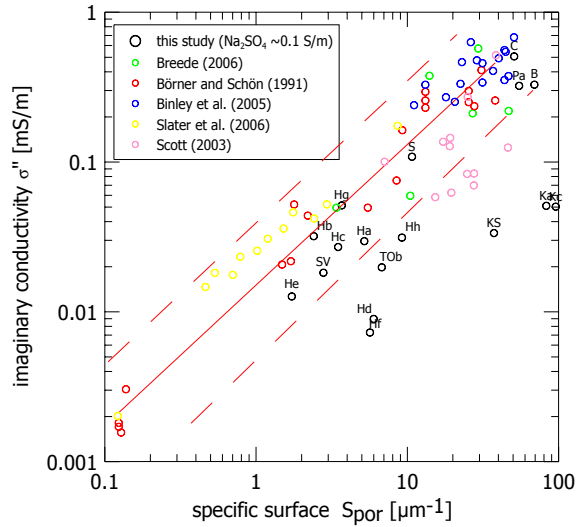


Figure 3.4: Imaginary component of the complex electric conductivity σ'' specific versus surface S_{por} as measured on building material samples saturated with Na_2SO_4 and results of previous works by other authors. The red lines enclose 68% of the data (Gaussian standard deviation).



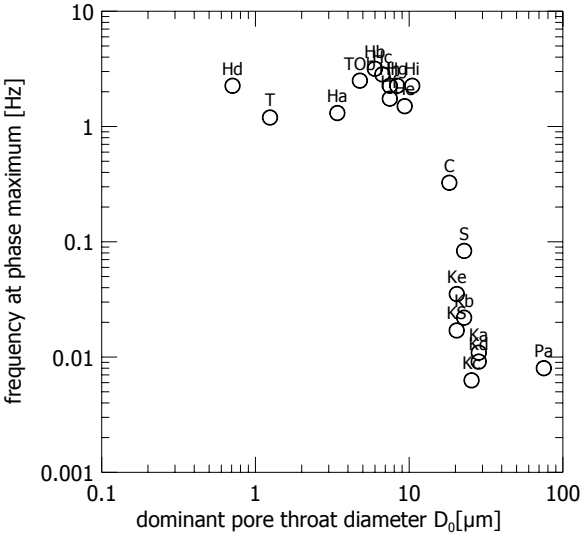


Figure 3.5: Frequency at which the maximum phase value was observed after saturation with distilled water versus dominant pore throat diameter (MICP).

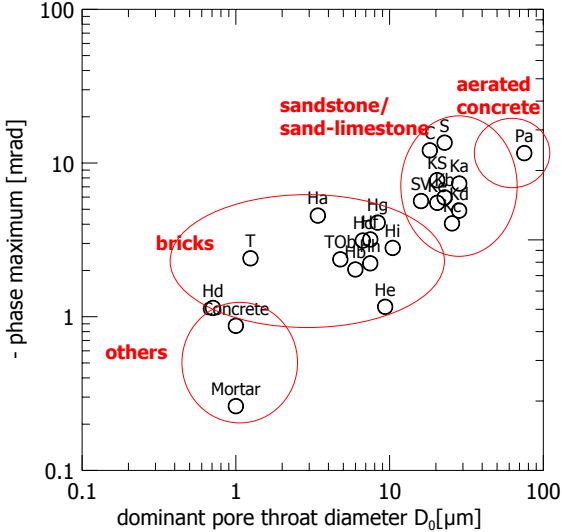


Figure 3.6: Maximum phase value as measured for each material after saturation with distilled water versus dominant pore throat diameter (MICP).

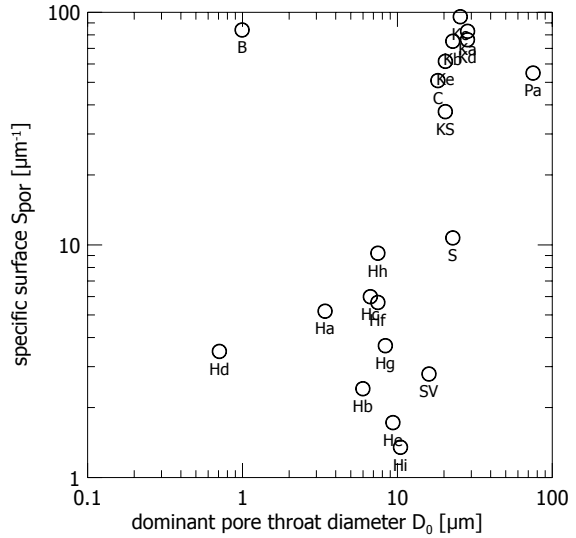


Figure 3.7: Variation of specific surface S_{por} with dominant pore throat diameter D_0 .

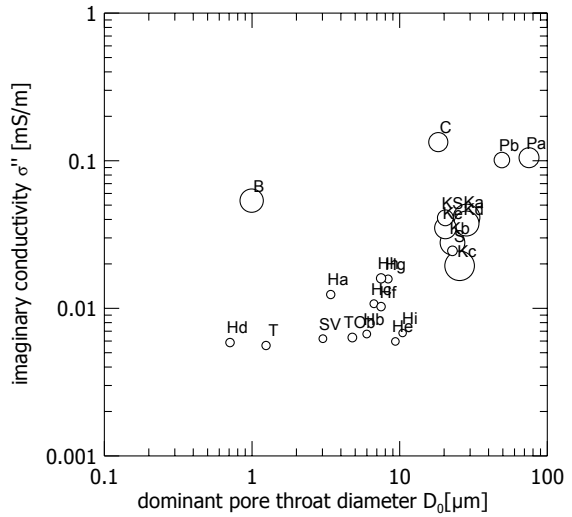


Figure 3.8: Imaginary conductivity σ'' at peak frequency as a function of the dominant pore throat diameter D_0 , increasing bubble sizes denote increasing specific surface S_{por} . Measurement results for samples saturated with distilled water.

3.3 Salt type and concentration

Sandstones

Figure 3.9 shows the CR spectra of Bentheimer sandstone samples at varying sulfate and chloride concentrations. The Bentheimer sandstone results conform to a Cole-Cole type of relaxation. At very low Na_2SO_4 concentrations the phase peak reaches maximum values of -45 mrad. With rising salt concentration of the fluid the polarization decreases. When saturated with $NaCl$ instead, the peak phase is not as high at similar salt concentrations. Comparing the results of $MgSO_4$ and $CaCl_2$ with the equivalent concentrations of the corresponding sodium salt, polarizations are significantly lower for divalent salts. Generally, for all salts the phase peak is observed to shift towards higher frequencies for higher salt concentrations.

Other sandstones behaved differently while saturated with the same brines. For the sodium salts Cottaer sandstone shows first an increasing and later on, at fluid concentrations of about 400 ppm (0.0113 mol/L), a declining phase peak (Fig. 3.10). For $MgSO_4$ or $CaCl_2$ brines the maximum phase is almost independent of salinity up to concentrations of 800 ppm. While the position of the peak phase for the sodium salts moves clearly to lower frequencies, for the other salts it remains constant.

The Baumberger sandstone does not follow a Cole-Cole type relaxation type and shows flat phase spectra. Similarly to Cottaer sandstone, they first increase and for higher fluid salinities decrease (Fig. 3.11). Again, for the salts containing divalent cations the polarization is almost constant for all salt concentrations.

Other materials

Figure 3.12 shows the spectra for the French Savonnières limestone, which is as well a natural building stone. As in the case of Baumberger sandstone, they do not show a Cole-Cole type behavior. This material possesses straight phase spectra of almost no slope (close to CPA behavior). Polarization values are generally relatively low and quickly fall below -6 mrad, which is the maximum phase with distilled water as pore fluid. As with the sandstones, polarizations after saturation with a divalent cation salt is considerably lower compared to results after saturation with a salt containing a monovalent one.

Figure 3.13 shows the spectra of three other materials for brines at varying Na_2SO_4 concentrations. The materials shown here are a sand-limestone (a), an aerated concrete (b) and two historic bricks (c and d). The spectra show generally all the same behavior as Bentheimer sandstone. Decreasing phases for increasing salinities. All materials besides the historic brick Hd have a peak phase that moves towards higher frequencies when the salinity increases. The results were not strongly dependent on brine type, so the results of the other salts are not shown here.

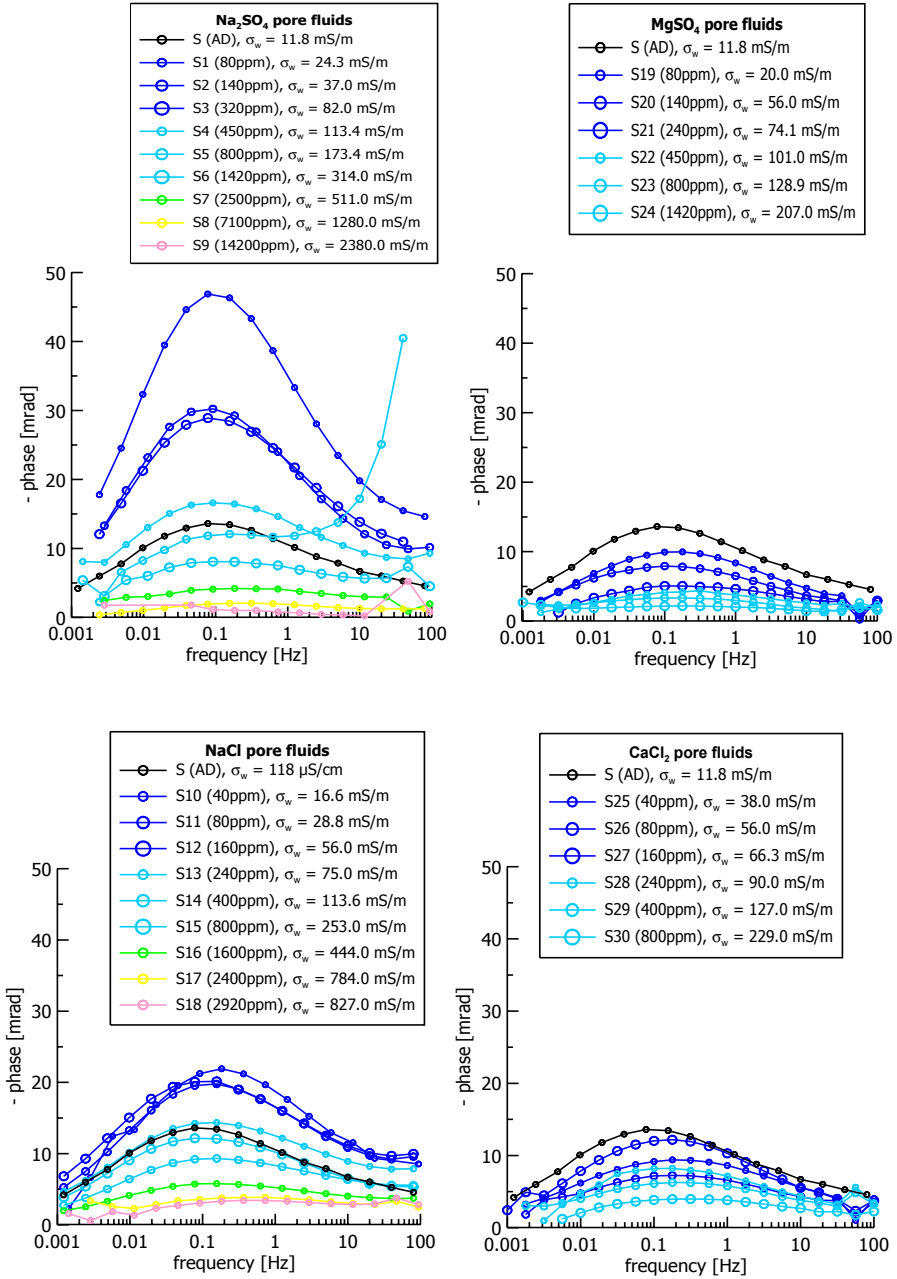


Figure 3.9: Bentheimer sandstone, CR phase spectra measured on samples with varying sulfate and chloride concentrations. From top left to bottom right: Na_2SO_4 , $MgSO_4$, $NaCl$, $CaCl_2$.

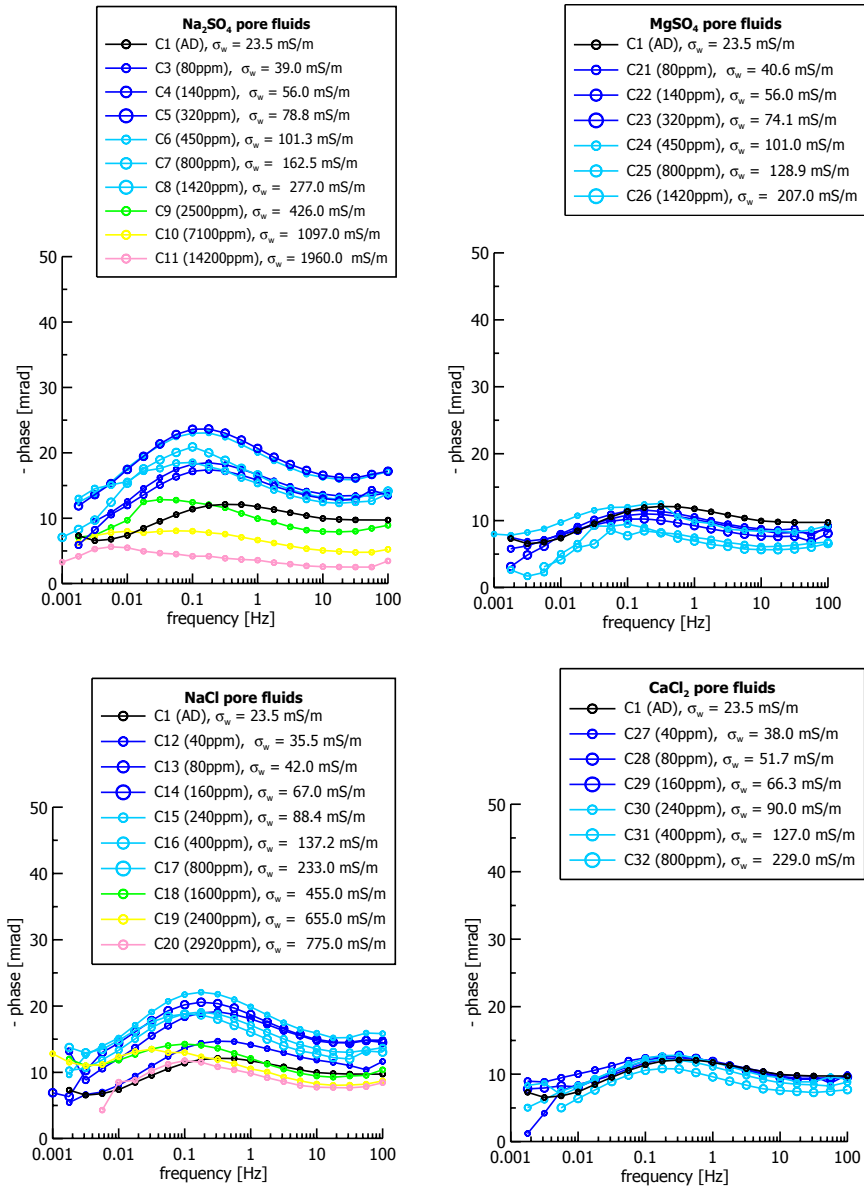


Figure 3.10: Cottaer sandstone, CR phase spectra measured on samples with varying sulfate and chloride concentrations. From top left to bottom right: Na_2SO_4 , $MgSO_4$, $NaCl$, $CaCl_2$.

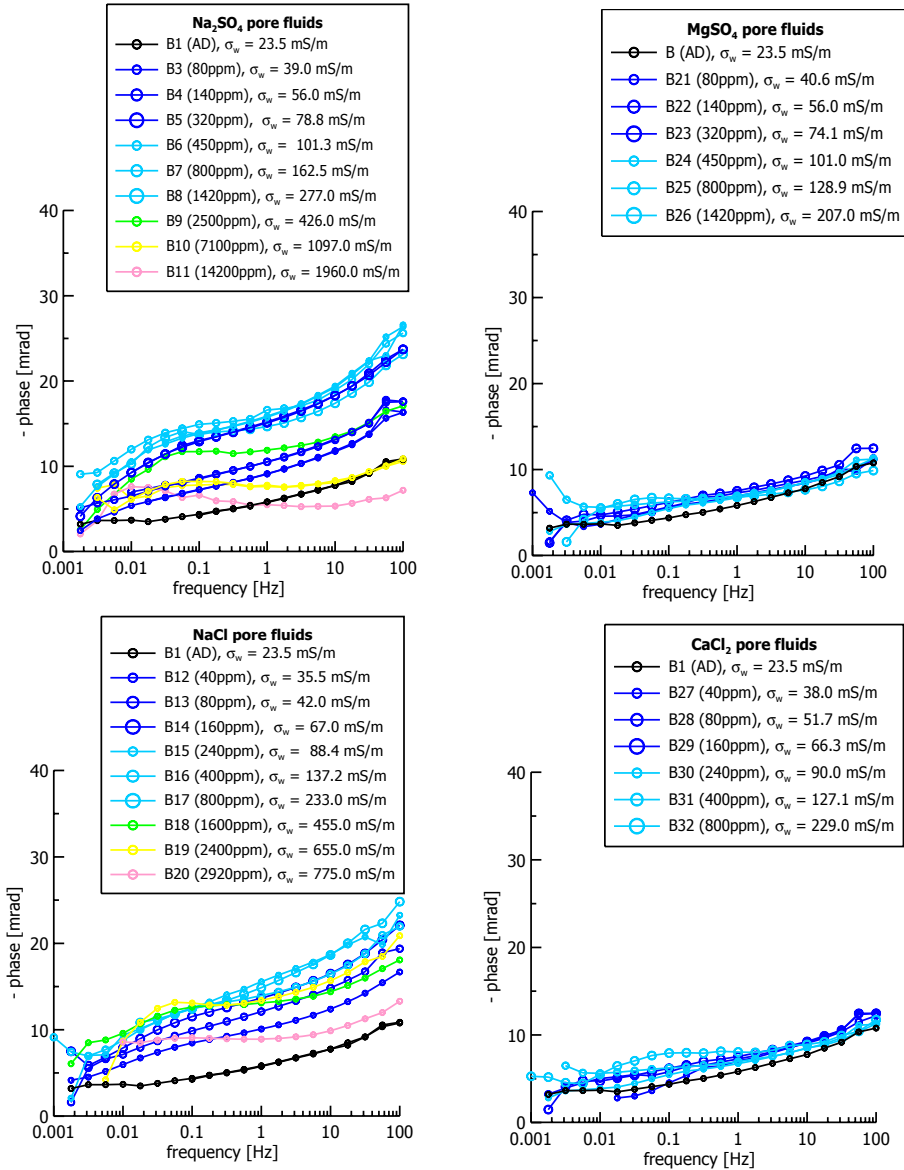


Figure 3.11: Baumberger sandstone, CR phase spectra measured on samples with varying sulfate and chloride concentrations. From top left to bottom right: Na_2SO_4 , MgSO_4 , NaCl , CaCl_2 .

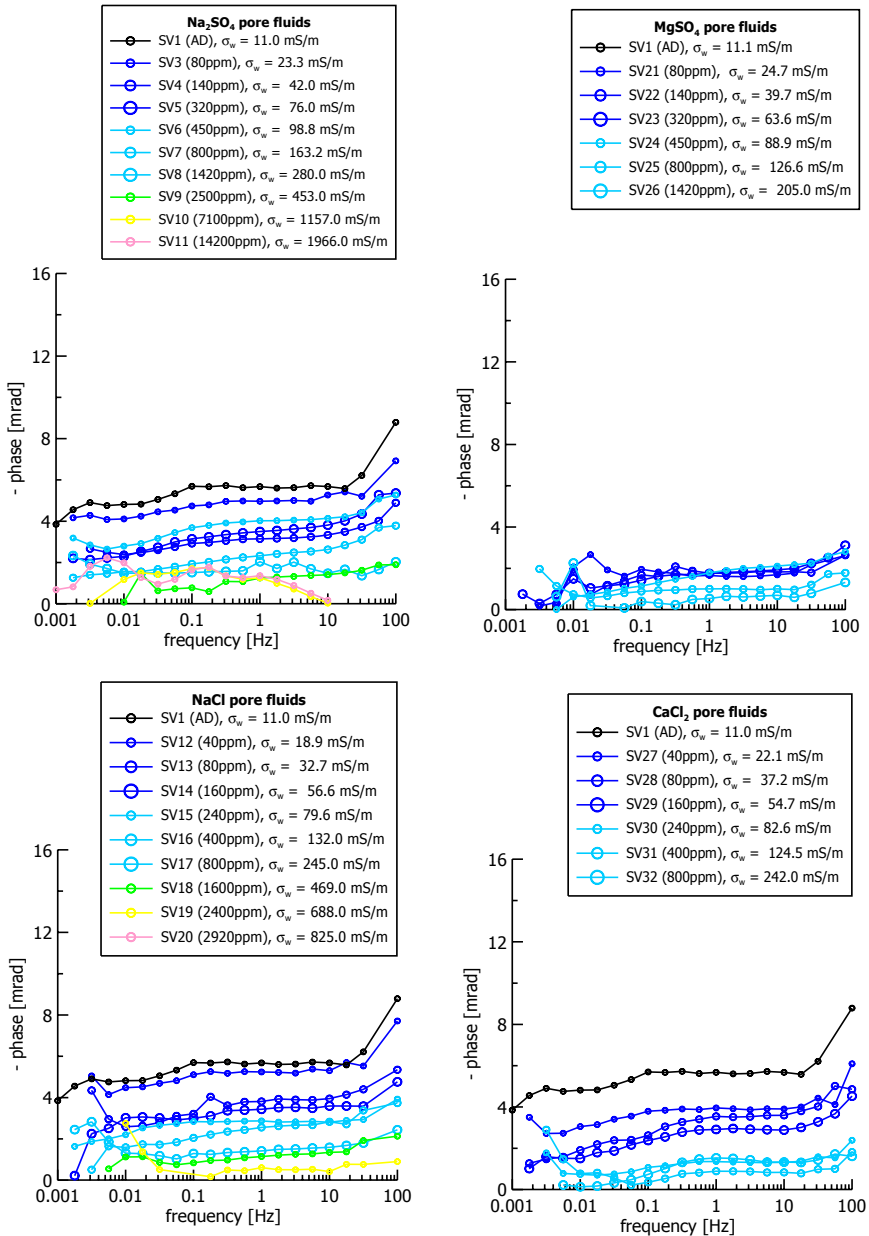


Figure 3.12: Savonnières limestone (SV), CR phase spectra measured on samples with varying sulfate and chloride concentrations. From top left to bottom right: Na_2SO_4 , MgSO_4 , NaCl , CaCl_2 .

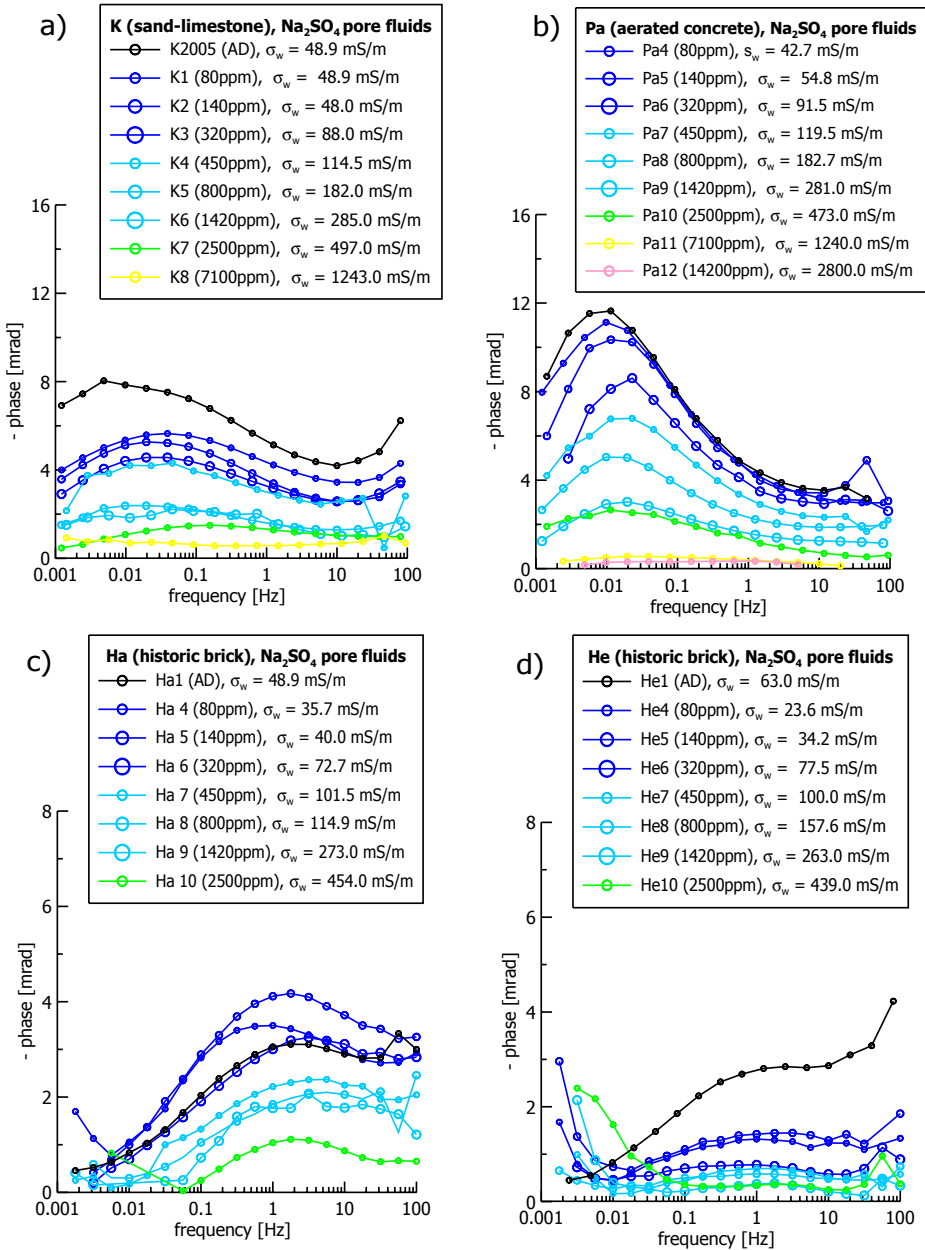


Figure 3.13: CR phase spectra of a) fabricated sand-limestone (K), b) aerated concrete (Pa), c) historic brick samples (Ha) and d) historic brick sample He. All samples were saturated with Na_2SO_4 brines of the same concentrations.

3.4 Conductivity components σ' and σ''

In saturated porous materials the dominant current path is usually through the bulk pore fluid and surface conductivity is a much smaller effect. Therefore, at high fluid salinities, CR parameter tend to be masked by the bulk conductivity. The imaginary conductivity seems to be more suitable than the phase to observe surface chemical effects, since it is a function of surface conduction only. The formation factor F (as defined in eq. 2.14) describes the decrease in conductivity of a water volume caused by the non-conducting matrix (Schön, 1996). In fact F depends on porosity, tortuosity and constrictivity, but for practical reasons a direct correlation of F and Φ is often assumed (second Archie's law, Archie, 1942). The correlation of F and Φ for the materials investigated in this study is given in Fig. 3.14. As reported by other authors an exponential correlation is found with M being typically around 1.3. Table 3.4 summarizes the formation factors obtained for the different brines used in this study as well as the mean value, which is used in the plot in Fig. 3.14 as well as the interface conductivities σ_q .

Figures 3.15 through 3.16 show real and imaginary conductivity as well as their ratio σ''/σ' as a function of fluid conductivity for all materials discussed above. Generally, real and imaginary components increase with increasing salinity. However, the imaginary conductivity seem to reach at least for some materials a certain maximum value, after that it starts to decrease again. The increase in surface conductivity results probably from an increase in surface charge density with increasing solution concentration. At higher concentration, an ion excess appears to result in ion-ion interactions that reduce their effective mobility. Lesmes and Frye (2001) state, this effect may be analogous to the decrease in solution activity at high ionic strengths due to ion-ion-interactions in the bulk pore solution.

Vinegar and Waxman (1984) measured similar behavior of the imaginary conductivity on shaly sandstones when they varied the salinity from 0.01 M to 2 M NaCl. They argued that at high salinity the diffuse part of the EDL is compressed, making it easier for anions to migrate through the clay blockages thus decreasing the magnitude of the membrane polarization effect. Instead, Lesmes and Frye (2001) explain their results just in terms of the electrochemical polarization of the EDL and state that at high salinity simply the effective mobility of the ions decreases. As a conclusion they draw to isolate the surface conductivity using effective medium models (Lesmes and Morgan, 2001). It should result that if a reduction in surface ionic mobility in the EDL is responsible for the decrease in imaginary conductivity, then the real part of the surface conductivity should decrease, too. However, if instead increased anion mobility (for example at clay blockages) is responsible, then the real part should increase at high salinity. In the unpublished PhD work of Flath (1989) the author reported, that the quadrature component of NaCl brine saturated shaly sandstones from the Helsby Formation reach their maximum at fluid conductivities between 1000 and 10000 mS/m. Her observation is consistent with the results of the experiments presented here.

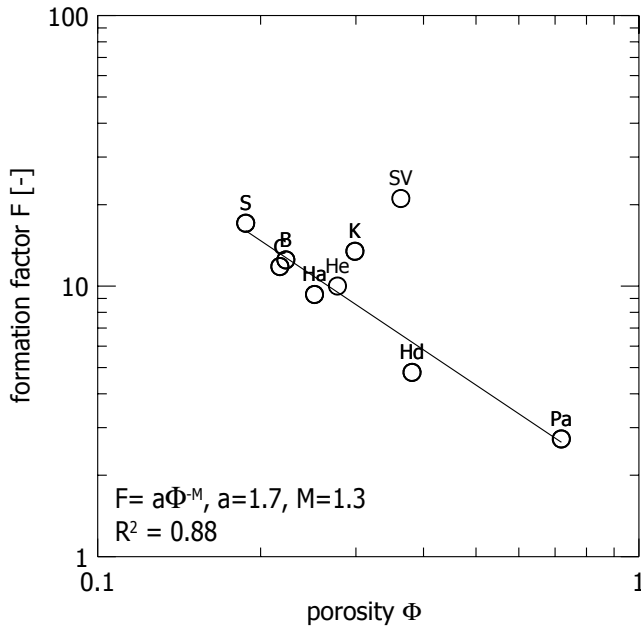


Figure 3.14: Formation factor F versus porosity Φ for the different building materials.

Table 3.4: Formation factors F and interface (intercept) conductivities σ_q in [mS/m] of the building material samples under investigation as obtained in the multiple salinity measurements.

	Pa	S	C	B	SV	K	Ha	He
$F (Na_2SO_4)$	3.12	22.10	14.34	15.23	18.29	28.49	6.60	10.01
$F (MgSO_4)$	2.64	12.24	11.61	12.95	30.14	7.70	9.93	-
$F (NaCl)$	2.41	21.05	11.61	12.65	16.71	7.56	10.54	-
$F (CaCl_2)$	-	12.89	9.68	9.15	19.31	10.03	10.17	-
F (average)	2.72	17.07	11.81	12.49	21.07	13.45	9.31	10.01
$\sigma_q (Na_2SO_4)$	29.06	1.54	12.43	13.85	1.23	5.94	3.27	3.30
$\sigma_q (MgSO_4)$	21.57	1.94	13.95	13.63	3.36	1.92	0.80	-
$\sigma_q (NaCl)$	16.69	4.20	11.22	12.30	1.92	2.44	1.10	-
$\sigma_q (CaCl_2)$	-	2.90	12.80	10.64	0.28	2.92	2.15	-
σ_q (average)	22.44	2.64	12.60	12.61	1.70	3.30	1.83	3.30

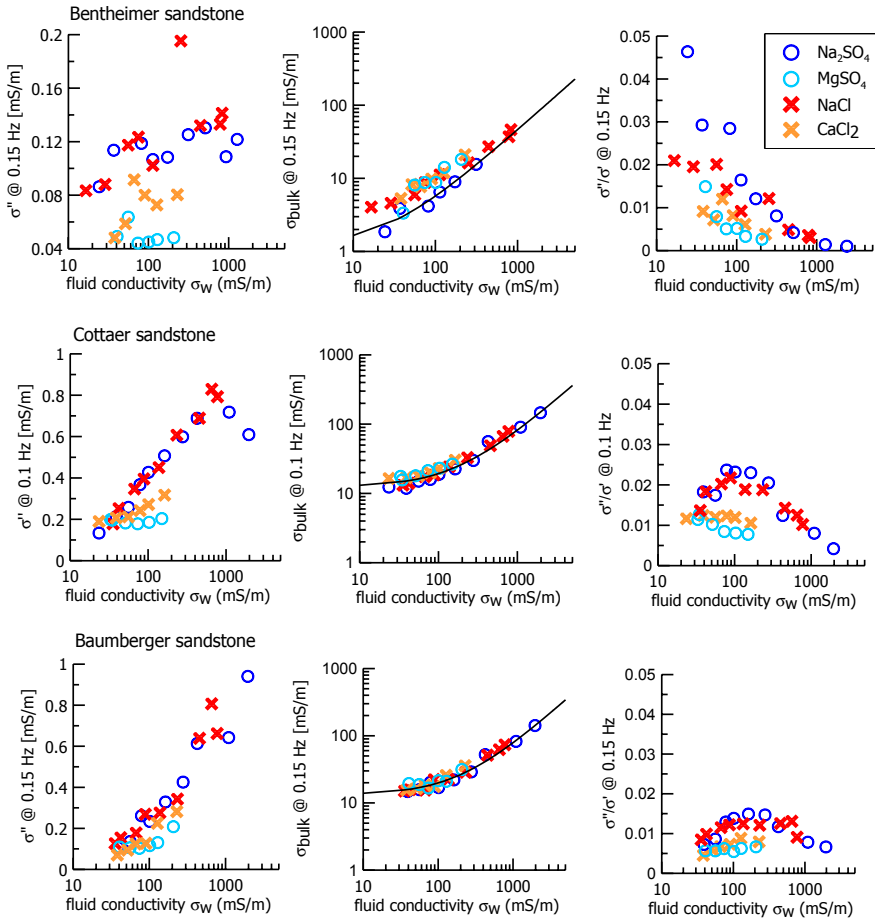


Figure 3.15: Imaginary part (left), bulk (middle) conductivity and ratio of imaginary and real conductivity (right) versus fluid conductivity for three different sandstones.

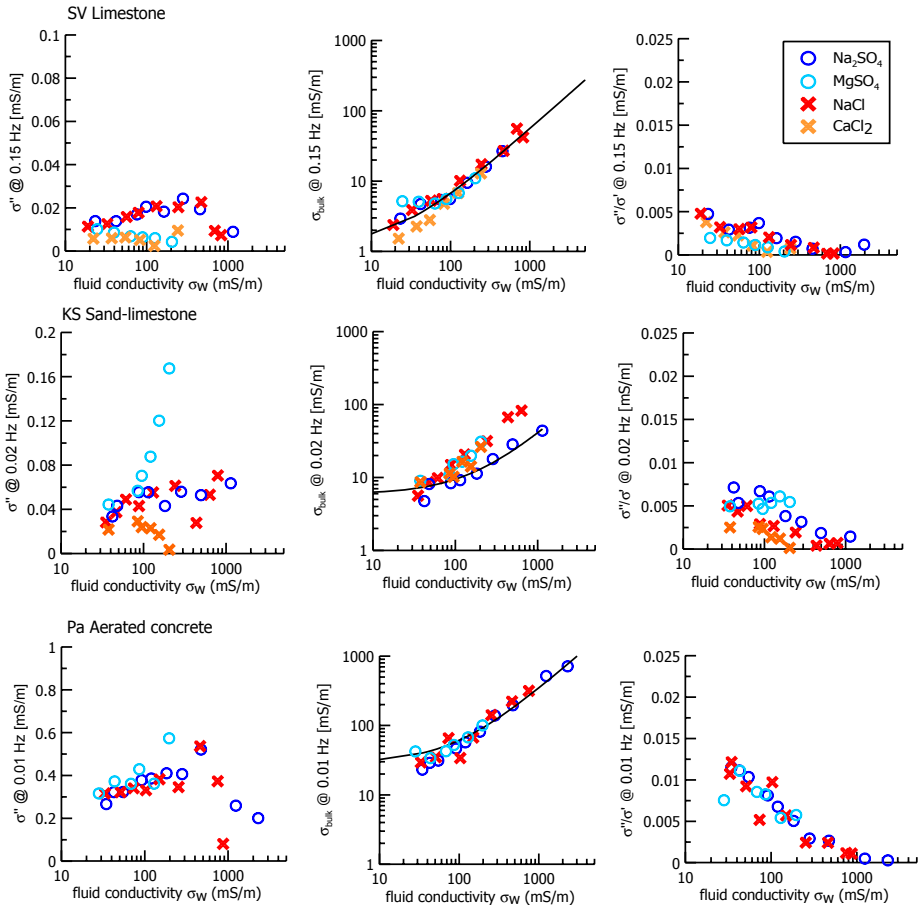


Figure 3.16: Imaginary part (left), bulk (middle) conductivity and the ratio of imaginary and real conductivity (right) versus fluid conductivity for a limestone sample, a sand-limestone and an aerated concrete.

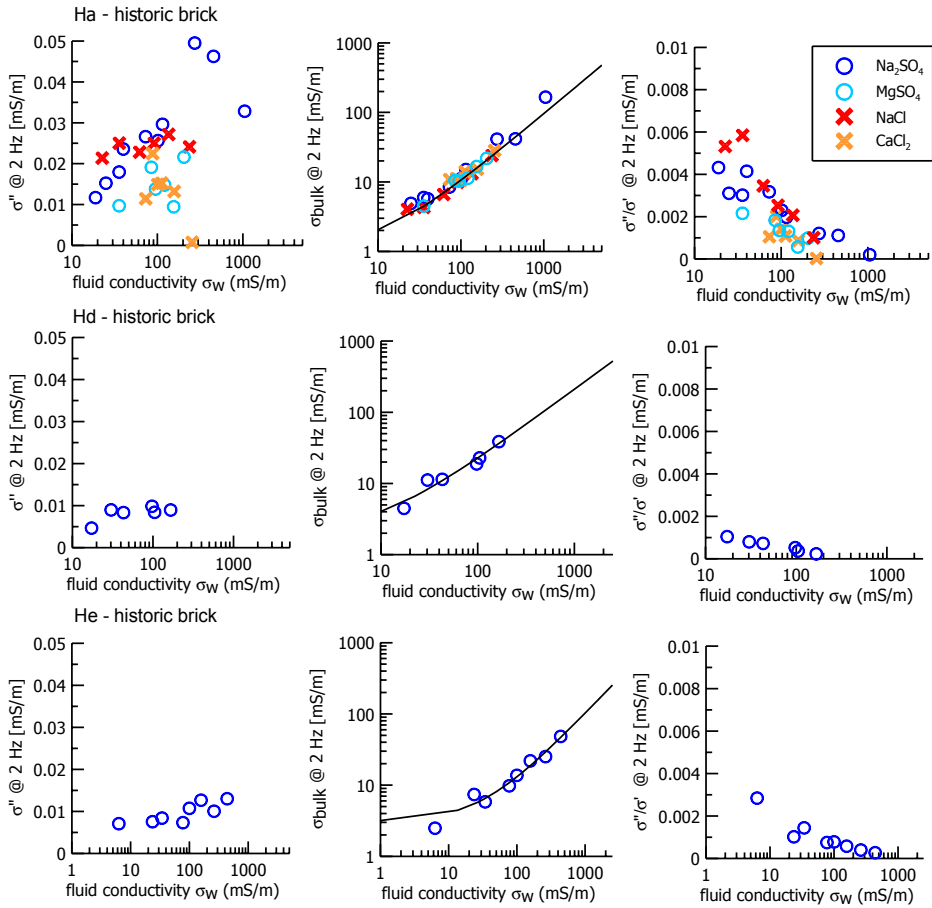


Figure 3.17: Imaginary part (left), bulk (middle) conductivity and the ratio of imaginary and real conductivity (right) versus fluid conductivity for three different bricks.

3.5 Cole-Cole modelling

For materials, which consistently complied to a Cole-Cole relaxation type, CR spectra were interpreted using the SpecFit routine provided by Kemna (Kemna, 2000). This program implies the data can be represented by the superposition of 2 or 3 Cole-Cole terms (eq. 2.33). It should be noticed (and it was mentioned earlier - compare section 2.4.1), that a major drawback of interpreting complex resistivity with Cole-Cole type models is the interrelation of their parameters. However, this kind of model has been widely accepted and is often used in existing literature. The results are thoroughly discussed below.

Figure 3.18 through 3.20 show the fitted low frequency relaxation Cole-Cole parameters as a function of fluid conductivity σ_w . For most materials the relaxation time τ (3.18) decreases for higher salt concentrations. In this figure power-laws were fitted to the Na_2SO_4 pore fluid results, and table 3.5 summarizes the exponents of all material/salt combinations. Another way to present the data is shown in Fig. C.4, where for each fluid one diagram compares the results of all materials. It appears, that just the clay-rich Cottar sandstone shows a positive correlation, for all others tau decreases with increasing fluid conductivity. According to Sen (1981), models based on effective media theories predict that the dispersion of the conductivity response will shift to higher frequencies (and thus, to lower relaxation times τ) with increasing solution conductivity. Münch et al. (2005) and Münch et al. (2006) report observations from salinity dependent CR measurements on unconsolidated sands, showing a decreasing power-law correlation between τ and fluid salinity. The exponents ranged between -0.05 and -1.84 and are, hence, about similar to what has been observed here. Moreover, for sands they also found the power-law to depend on grain size. These authors argue that with increasing salinity the EDL thickness would decrease and result in lower relaxation times.

Table 3.5: Power law fit results of relaxation time τ versus fluid conductivity (Fig. 3.18.)

Sample	Na_2SO_4	$NaCl$	$MgSO_4$	$CaCl_2$
S - Bentheimer	-0.354	-0.076	0.261	-0.206
C - Cottar	0.384	0.553	0.432	0.319
Pa - aerated concrete	-0.537	-0.079	-0.312	-
Ha - hist. brick	-0.442	-0.075	0.199	-
KS - sand-limestone	-0.423	-0.128	-0.047	-0.439

Figure 3.19 shows the normalized chargeability parameter m_{norm} in the Cole-Cole model increases for all materials and salts with increasing salinity. For the same concentrations the normalized chargeability of the $MgSO_4$ and $CaCl_2$ saturated samples is usually lower compared to those saturated with Na_2SO_4 and $NaCl$. The only material for which this observation does not apply is sand-limestone. Lower m_{norm} values for the salts with divalent cation are in good agreement with the assumption that these ions are attached stronger to the pore walls than monovalent ion - as has been mentioned in the

previous section.

Figure 3.20 shows fluid conductivity and the Cole-Cole exponent c does not show a clear relationship. While there seems to be a general trend of somewhat decreasing c values for increasing fluid conductivity, the relationship is weak and obviously of limited practical value.

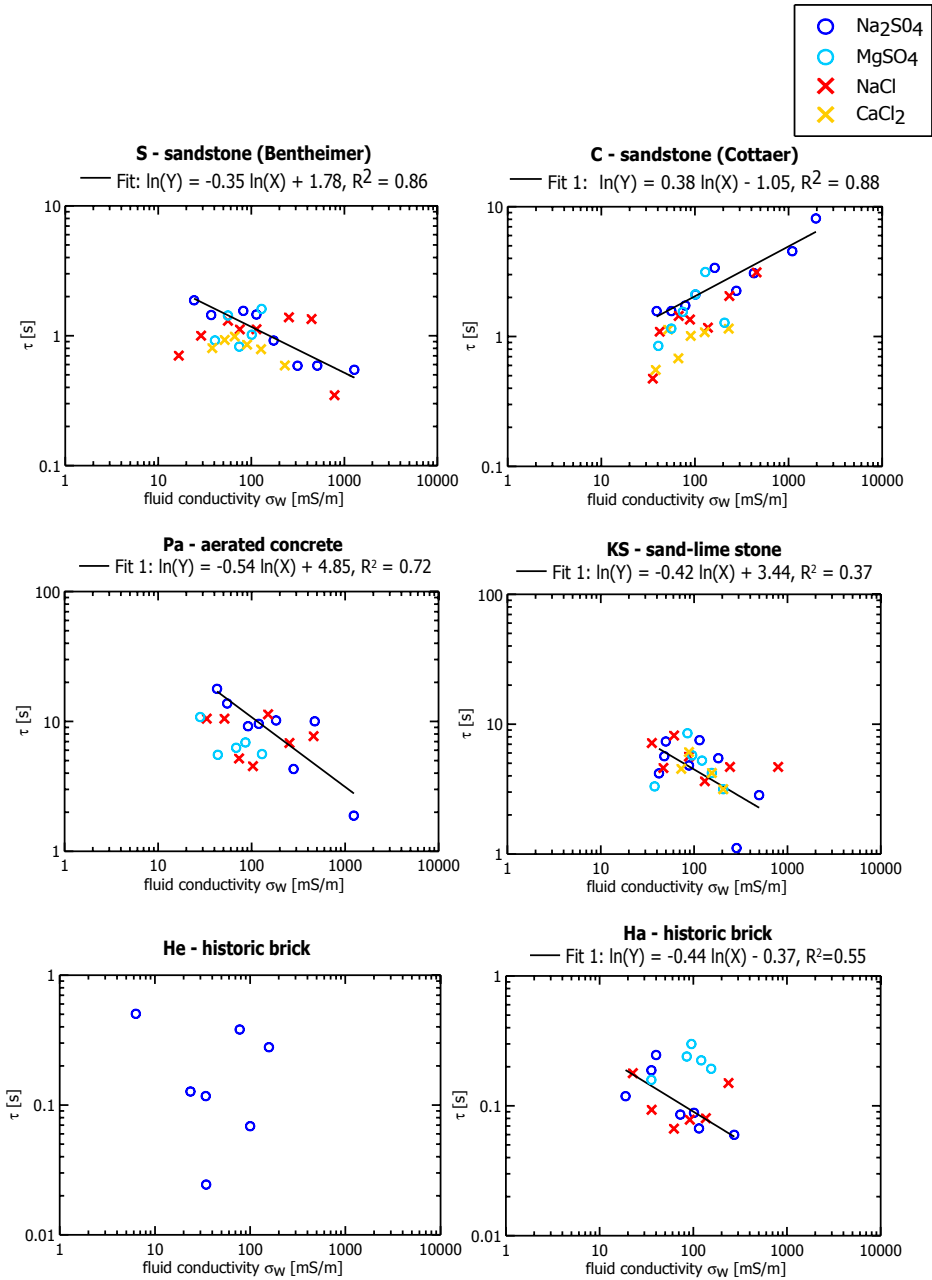


Figure 3.18: Relaxation time τ as resulting from the C-C data fitting routine SpecFit for the low relaxation term versus fluid conductivity.

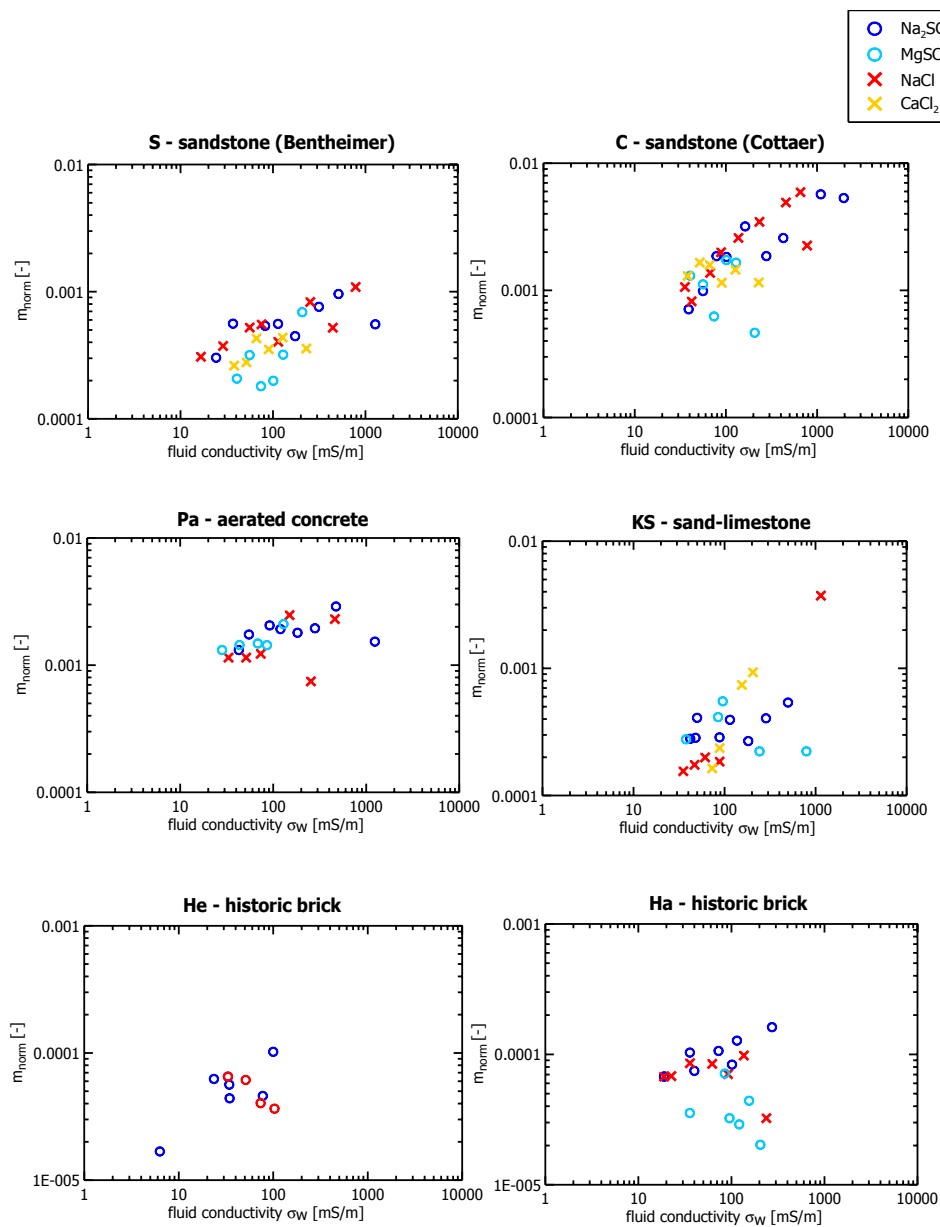


Figure 3.19: Normalized chargeability m_{norm} as resulting from the C-C data fitting routine SpecFit for the low relaxation term versus fluid conductivity.

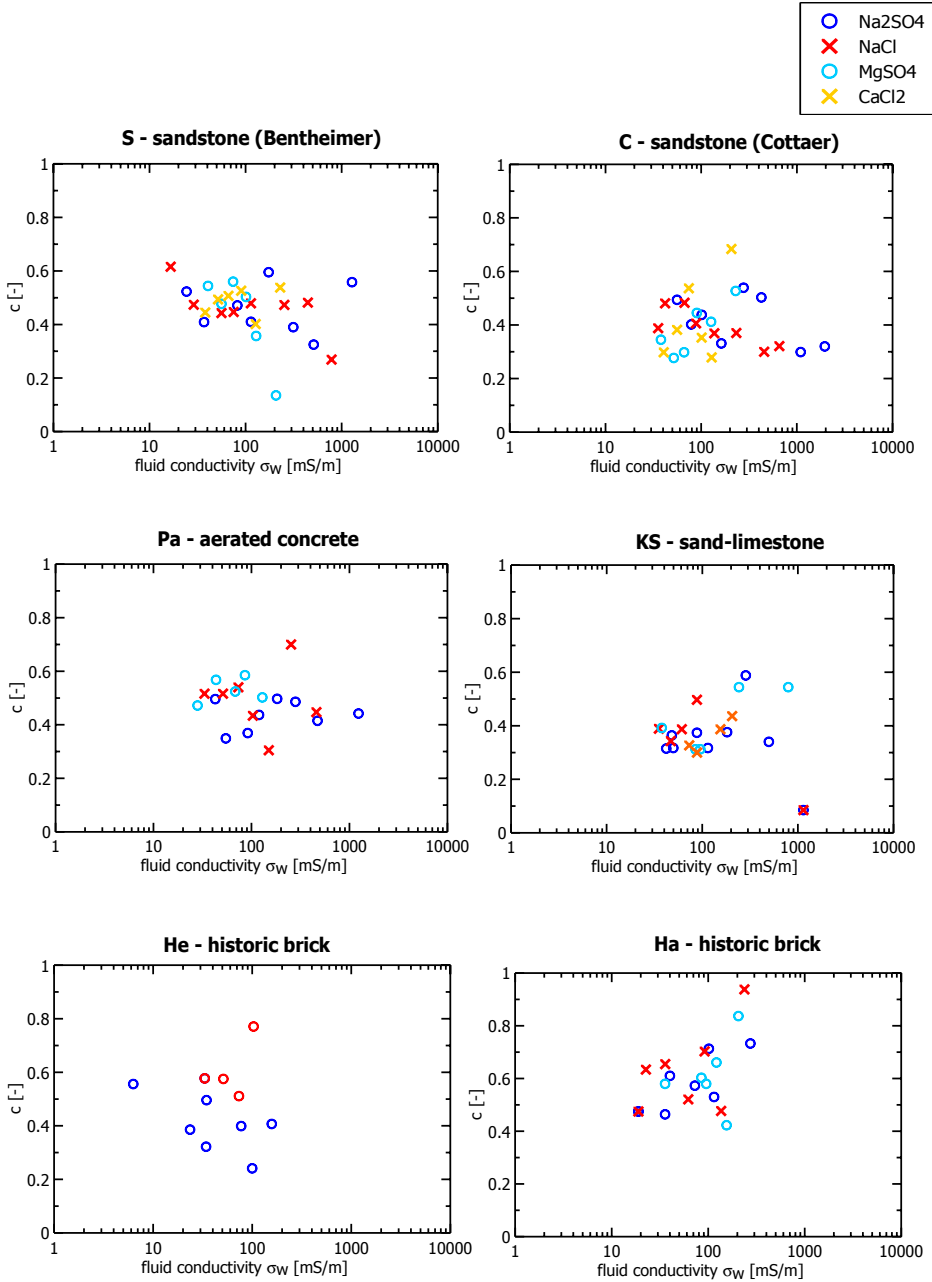


Figure 3.20: Cole-Cole exponent c as resulting from the C-C data fitting routine SpecFit for the low relaxation term versus fluid conductivity.

3.6 Comparison distilled water / tap water

In addition to the above presented salt experiments it has been reckoned useful to compare specifically the results of distilled and tap water saturated samples. The reason being that two very typical sources for water damages in building stones are leakages due to improper tubing and rainwater ingress. Either one causes particular damage patterns and requires specific care. If the water source and hence, type of degradation expected is not obvious, non destructive testing methods could provide valuable information. A study on a series of samples saturated with distilled water, which in terms of ion content and chemistry is very similar to rain water, and tap water has been conducted. Distilled water has originally a conductivity of $\sigma_w \sim 0.001 \text{ S/m}$, whereas the tap water used (sample saturation was realized at TU Berlin, Germany) had a conductivity of $\sigma_w \sim 0.7 \text{ S/m}$.

For the great majority of the materials, the polarization magnitude (phase angle) noticeably decreases as the ion content increases (see Fig. 3.21). Also does the resistivity magnitude. Only for two materials, that is Cottaer and Baumberger sandstone, phase angles elevate.

Figures 3.22 and 3.23 compare the real and imaginary components of the electrical conductivity as measured for distilled and tap water samples. For all samples but some of the bricks the imaginary components σ'' increase when saturated with tap water. The bricks for which the imaginary conductivity decreased with ion content are the types He, Hf, Hg, Hh, Hi. Reasons of which might be the mineralogy and/or pore geometry of the particular material. However, as yet it seems less favorable to assume geometrical features originating such behavior, since no major differences in average pore throat diameters nor BET specific surface values could be found.

The only material for which a higher real (bulk) conductivity has been measured as saturated with distilled water is the sand-limestone type Kc. One possible explanation could be, that this material is highly dissolvable and distilled water a reactive fluid resulting in a highly conductive fluid after reaching a solvation equilibrium.

Generally it seems possible to distinguish distilled water from tap water damages using CR. The resistivity (or conductivity) magnitude by itself yields probably enough information, if calibration data are available for the material(s) involved. However, an important parameter in assessing the damage source by fluid conductivity is definitely the contact time the object has had with the fluid at the time of investigation. The longer the material is exposed to water and solvation processes could take place the more challenging it will be to discriminate different damage sources, because the ion-less rain water will quickly solve ions from the fabric and become very similar to tap water.

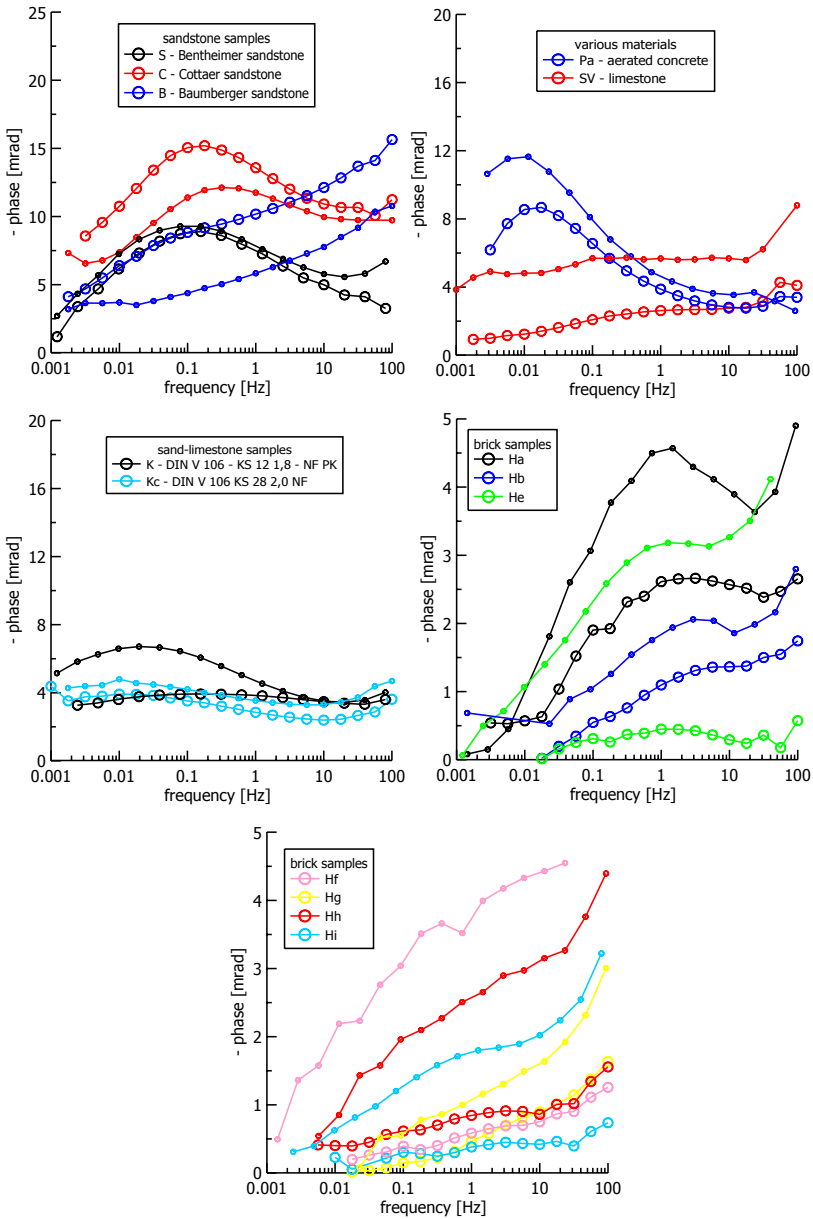


Figure 3.21: CR phase spectra of saturated building materials. Results of samples saturated with distilled water (small circles) are compared to saturations with tap water (big circles).

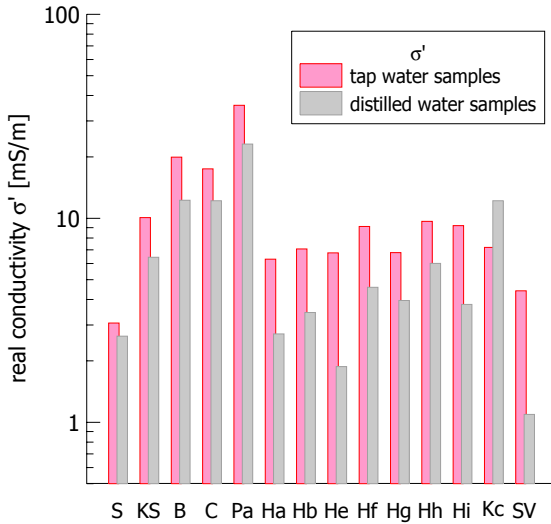


Figure 3.22: Real components of the electrical conductivity for samples saturated with distilled (grey) and tap water (pink) respectively.

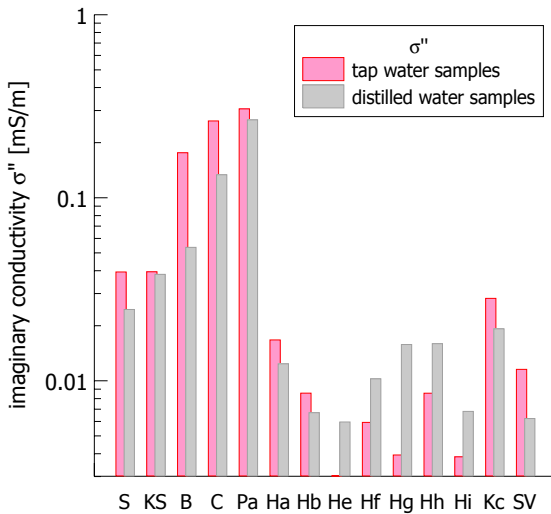


Figure 3.23: Imaginary components of the electrical conductivity for samples saturated with distilled (grey) and tap water (pink) respectively.

Figure 3.24: Change of the real conductivity component σ' between distilled and tap water saturated samples.

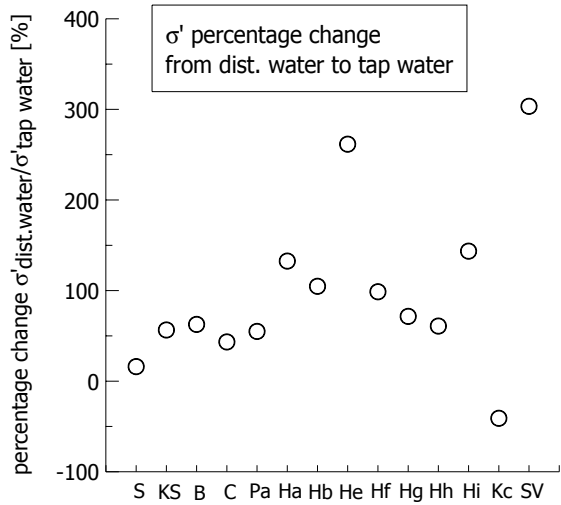
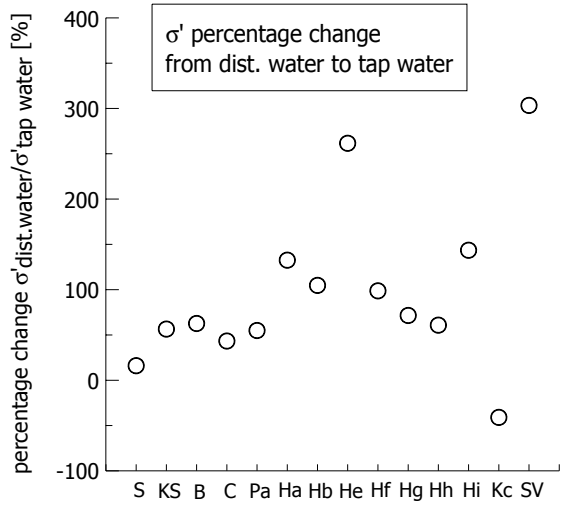


Figure 3.25: Change of the imaginary conductivity component σ'' between distilled and tap water saturated samples.



3.7 Summary

A total of 21 building stone samples have been saturated with distilled water and brines of four salts in up to eight concentrations ranging from 0.8 - 147 mmol/L. It has been noted that some building materials are polarizable and show various types of different CR behavior when saturated. Some spectra conform to the classic Cole-Cole relaxation, others exhibit no polarization peak, but flat spectra and a weak polarization decrease towards lower frequency.

The parameter obtained from C-C models may be useful to deduce information on pore surface area and dominant throat size. Figure 3.26 depicts the results of this study and data reported in Binley et al. (2005), Scott and Barker (2005) and Breede (2006b), who all used synthetic (ground) waters as pore fluids. The ion contents of the fluids used are listed in Table 3.6, the bulk electrical resistivities generally resulted to be around 0.1 S/m.

Table 3.6: Ion concentrations c in mol/L as used for CR measurements and data shown in Fig. 3.26.

ion	this study	Binley et al. (2005)	Scott (2006)	Breede (2006b)
Cl^-	-	0.0009	0.0034	0.0086
NO_3^-	-	0.0114	-	-
SO_4^-	0.0083	0.0009	0.0003	-
Na^+	0.0166	0.0009	0.0060	0.0086
Mg^{2+}	-	0.0009	0.0007	-
Ca^{2+}	-	0.0057	0.0006	-
σ_w [S/m]	0.16	0.1	0.078	0.18

The power-law correlation between C-C relaxation time τ and dominant throat diameter D_0 with a slope of 2 was predicted by many authors like Schwarz (1962), Fixman (1980) or Titov et al. (2002), since for electrochemical polarization the relaxation frequency is related to some critical length scale l (that is, pore throat radius in consolidated materials or grain radius in unconsolidated materials):

$$\tau = \frac{l^2}{4D_i} \quad (3.1)$$

with D_i being the diffusion constant in m^2/s . However, the correlation between pore throat sizes and relaxation time should be used cautiously. The presented power-law fit has only a coefficient of determination R^2 of 0.53. The relaxation time τ scatters and varies over three orders of magnitude for a two order range of pore throat diameter. A few datum points do not follow the general trend, one of which being a sandstone sample measured by Breede (2006b). According to the author (oral communication) one possible explanation for this might be that this particular sandstone is very heterogenous. It has a broad pore throat size distribution and hence, the dominant pore throat diameter (MICP)

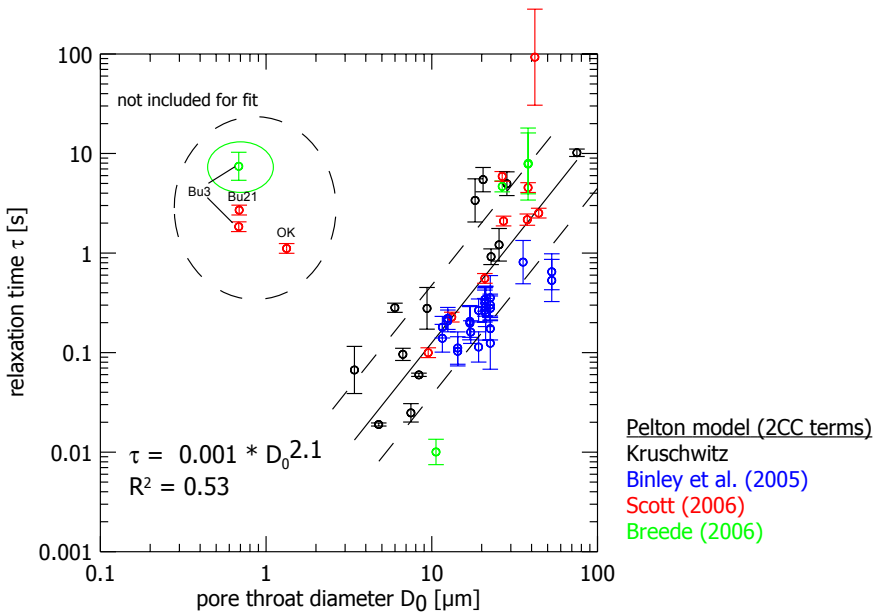


Figure 3.26: Correlation of relaxation time τ and pore throat diameter D_0 . Black: Results presented in this study. Blue: results presented by Binley et al. (2005), red: results presented by Scott and Barker (2005), green: results presented in Breede (2006b). The two dashed lines enclose 68% of the data (Gaussian standard deviation).

might not be truly representative. There is at least two more samples, that do not fit in the general trend, which belong to Scott's data basis (red pattern). Unfortunately, for his data were no further mineralogical details available. Generally, fluid salinity and chemistry (if no chemical reactions take place in the sample), however, seem to have only minor effect on this universal relationship. Figure C.3 compares the results obtained in this study for the 800 ppm Na_2SO_4 brines and distilled water and they clearly follow the same trend.

The results of the salt study show how responsive polarization (expressed as imaginary conductivity) is to changing the ions in the pore fluid. As for each material the specific surface area, roughness and the general chemical surface composition is constant in this experiment, it seems a logical step to assume the surface charge density and the effective mobility of the ions in the fixed and diffuse layer of the EDL primarily determine the magnitude of the CR response. It is evident, that the imaginary component σ'' of the conductivity as well as the resistivity phase angle ϕ are related to pore fluid chemistry. Generally, even when small quantities of divalent salts (here $MgSO_4$ and $CaCl_2$) are added to the solution, the imaginary conductivity is far less compared to the salts with monovalent cations (here Na_2SO_4 and $NaCl$). Divalent cations like Mg^{2+} and Ca^{2+} will probably shield the negative charge of the EDL more efficiently, and their bondage to

the inner surface is stronger compared to Na^+ . This becomes evident in the conductivity plots in Fig. 3.15 through 3.16. In contrast, interpreting CR responses in terms of changing diffusion properties is not straight forward. As can be seen in Fig. 3.27 the diffusion coefficients of $MgSO_4$ and $CaCl_2$ in bulk solution are lower compared to the two sodium salts. These values were reported by Lobo (1984) for bulk solutions and may not hold for diffusion along the EDL, but presumably the general trends apply for diffusion along the surface. Lobo's results, however, cannot explain why very similar CR responses were measured for Na_2SO_4 and NaCl, since these two salts take different diffusion coefficients according to his observations.

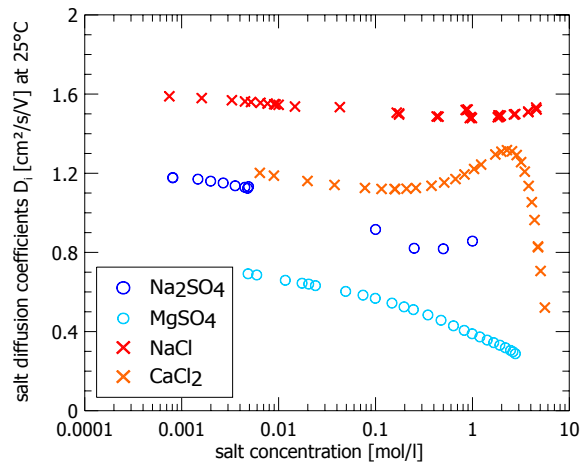


Figure 3.27: Diffusion coefficients D_i of aqueous salt solutions at 25° C after Lobo (1984).

Since no electrochemical information of the EDL properties are available the results are, as yet, inconclusive. The correlation between relaxation time τ and salt concentration of the saturating fluid is tentatively attributed to changes of ion mobility and diffusion coefficients of the fixed layer. The results encourage the study of surface chemical properties as a function of salt content and type. To improve the practical value and predictive use of complex resistivity measurements the theoretical understanding of the EDL and the particular changes with fluid salinity seem to be essential.

4 Saturation experiments

Recent publications evidenced that both the fluid chemistry as well as the saturation greatly alter the CR behavior of porous media. Obviously, real leakages in buildings will very likely result in a spatial distribution of changing water contents rather than a fully saturated locally confined area. This chapter discusses how CR properties of the building material samples change during evaporative drying after saturation with distilled water and intermediate saline brines.

4.1 Experimental Procedure

It has been recognized for example by Ulrich and Slater (2004) in their study on unconsolidated sands that the particular drying procedure (drainage, evaporation) influences the CR responses. Here the focus is whether any measurable change in CR behavior is apparent under one desaturating regime. To simulate desaturation similar to how would be in a building, unsaturated samples were prepared using evaporative drying. The saturation was determined by weighing the sample after each measurement. Agar was used as coupling medium in order to prevent water to be sucked back from the cell into the sample. However, with decreasing water content the measurements can get very noisy, since coupling to the sample becomes more difficult. It has been found that measurements of better reliance and also at lesser water contents can be made if Ag-AgCl electrodes are employed for the voltage measurement (compare Fig. B.2 in the appendix).

4.2 Results

4.2.1 CR Spectra

The characteristic length scale of relaxation is generally inversely related to an effective pore size. Therefore it was expected the polarization peak would shift to higher frequency (smaller pore size) with reducing saturation as larger pores drain preferentially (compare Binley et al. (2005)).

For a great majority of materials no such behavior was observed. Instead a very common desaturation effect was that the phase peak vanished very quickly for lower water contents resulting in flat and downwards (decreasing absolute phase values) shifting spectra. An example of such behavior is given in Fig. 4.1 (top) as measured for a sample of Cottaer sandstone originally saturated with distilled water. Generally, the pore fluid did not seem to have a large effect on CR properties during desaturation, implying that the saturating fluid chemistry is a second order effect and pore geometry, texture or perhaps clay content are more important. Like the Cottaer the Bentheimer and Baumberger

sandstones showed decreasing phases and disappearing phase peaks, if existent at full saturation.

The brick sample type Ha and aerated concrete Pa are the only samples investigated having peak phase CR characteristics throughout all partial saturations. While for the brick samples phases first increase and later decrease (see Figure 4.1 (center)), for aerated concrete they just decrease (bottom). The maximum phase shifts for the brick sample to lower and for aerated concrete towards higher frequency.

Looking at the low frequency ends of the spectra in Fig. 4.1 it is noticeable that the amplitude curves for some saturation levels decrease with frequency. This would mathematically correspond to a positive phase value (real and imaginary component of the conductivity are a Hilbert transformation pair), which is improbable for the materials investigated and mismatches with the actually measured phases shown in the same figure on the left. This unusual effect is explained by a real conductivity change of the sample during the time of the measurement. It is likely that the partially saturated samples have taken up water from the agar-gel used for the electrical contact to the electrodes. To account for this changing water content during the measurement, the saturation was always calculated by the Archimedes' weighing principle after finishing the measurement. This final water content was used to determine the saturation degree.

4.2.2 Cole-Cole parameters

Figure 4.2 shows the variation of the fitted Cole-Cole parameters as a function of saturation for the two samples Pa and Ha being the only two materials having Cole-Cole c type CR spectra throughout detwatering.

The variation of relaxation time τ with saturation is given in Fig. 4.2 (top). For aerated concrete τ shows only weak correlation, and for the brick sample τ increases with throughout desaturation as opposed to data published in Binley et al. (2005) (sandstone samples, same figure, green pattern), where the authors state, that relaxation time may be implicitly linked to some length scale influencing hydraulic conductivity. Hence, at least in case of the brick samples, the argumentation of Binley et al. (2005) it is unlikely to hold: for this material either multiple effects superpose resulting in a lack of obvious correlation of the hydraulically effective pore radius and the peak phase position as it dewateres. Other effects influencing the CR properties are changes in fluid chemistry (increasing salinity) and double layer properties (the geometrical side of which will be discussed in chapter 6.2.5 (modelling)). In fact, according to Pelton et al. (1978) $\tau \propto \sigma_{DC}^{-1/c}$, which implies, that for a constant c τ increases due to the conductivity decrease associated with reducing saturation. This is also what Münch et al. (2006) reported for measurements on sieved and washed, clay-free sands. In this work the pore fluid conductivities were very small around 4 mS/m.

The chargeability m versus saturation shows a decrease for aerated concrete and an increase for the brick sample. Again, the results of Münch et al. (2006) are included

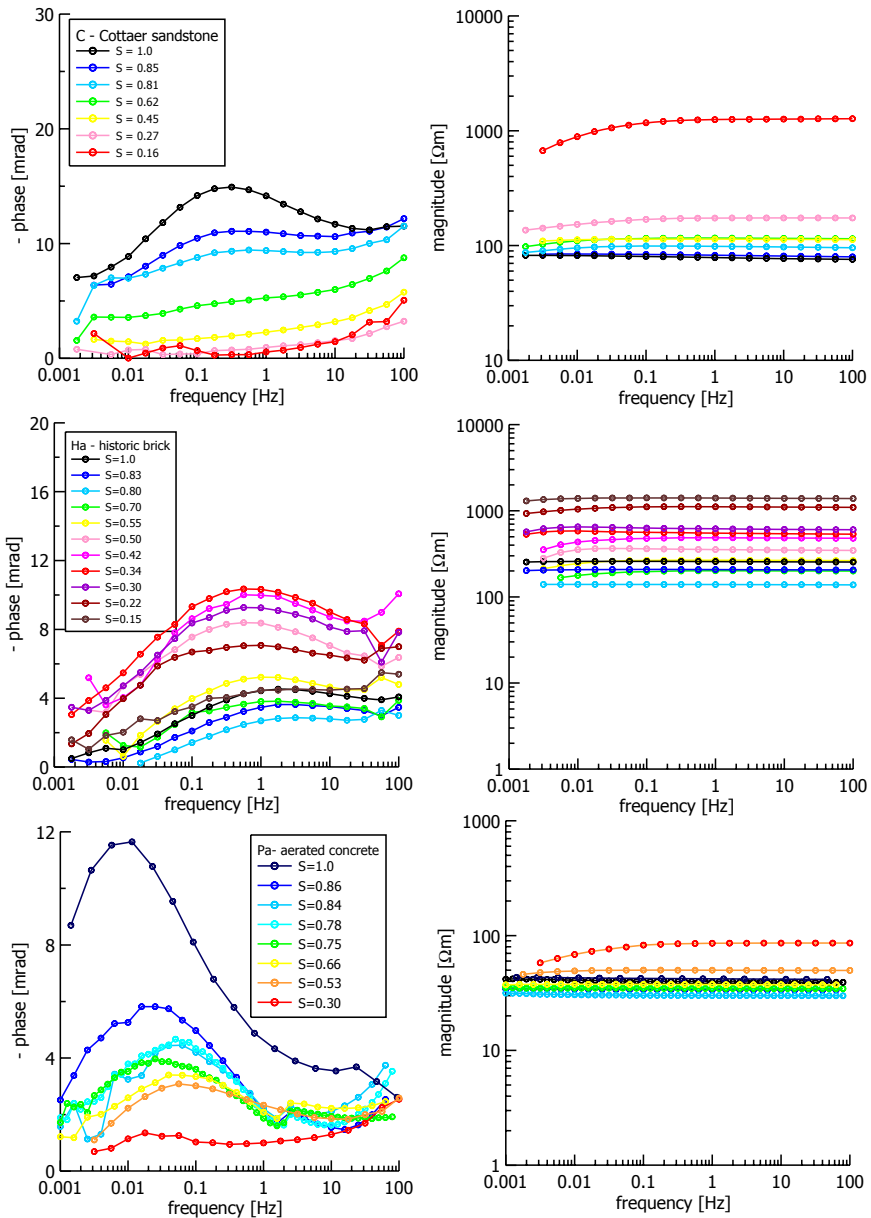


Figure 4.1: CR spectra (phase left, magnitude right) for a Cottaer sandstone sample (C, top) and a historic brick sample (Ha, center) and an aerated concrete (Pa, bottom) under different water saturations. All samples were originally saturated with distilled water.

in the figure and, in case of the brick, evidence the similarity of the data obtained on macroscopically different materials. Contrary, for both aerated concrete and brick the normalized chargeability (compare eq. 2.4.1) decreases significantly with reducing water content, for the first, however, more rapidly than for the latter. The Cole-Cole exponent c (Fig. 4.2 bottom) does not correlate to saturation for either of the two materials.

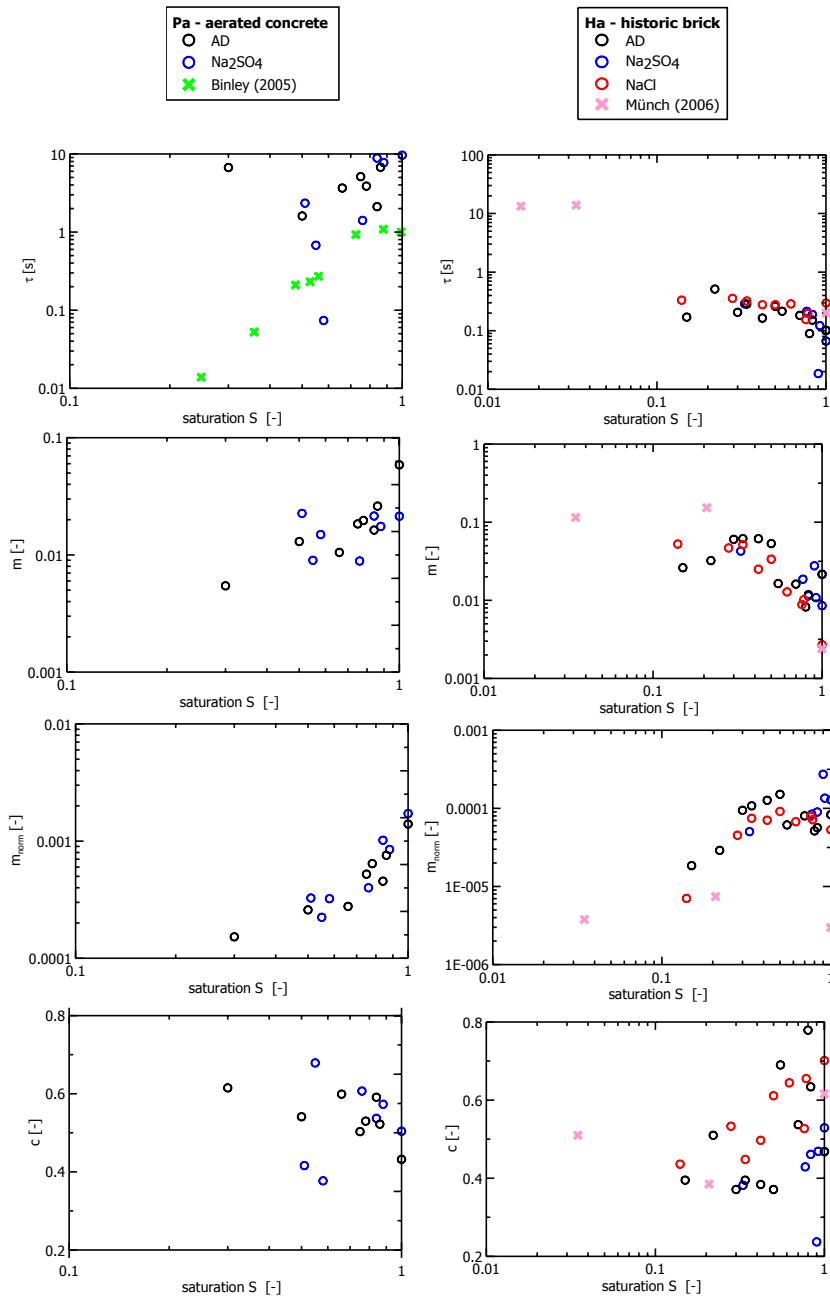


Figure 4.2: Variation of the C-C relaxation time, τ , normalized chargeability, m_{norm} , and C-C exponent, c , with saturation for aerated concrete (Pa (left)) and historic brick (Ha (right)) samples.

4.2.3 Saturation exponents

In Fig. 4.3 and 4.4 the real and imaginary conductivities are shown as a ratio during evaporation to the saturated value and denoted as σ'_{norm} and σ''_{norm} respectively. Both quantities obey mostly first-order power law dependence on saturation. For Cottaer sandstone five samples of different fluid chemistries have been desaturated resulting in very similar CR curves and saturation exponents for all for salts as well as distilled water respectively (compare Fig. 4.3 top). Hence, since the fluid chemistry does not seem here to change the general desaturation pattern, for all other materials exemplarily three samples were desaturated: one being saturated with distilled water, one with ~ 0.01 M Na_2SO_4 (800ppm) and one with ~ 0.01 M NaCl (400ppm). For all three sandstones as well as for the aerated concrete the imaginary conductivity σ'' decreases more rapidly than the real component σ' . Only for the brick and limestone samples are the saturation exponents for the polarization magnitude consistently lower than for the real conductivity. Values obtained for the three pore fluids (distilled water and ca 0.01 M NaCl and Na_2SO_4) are summarized in Table 4.1.

As opposed to the publications of Ulrich and Slater (2004), and other citations therein, in this study many sample-salt solution combinations showed the imaginary conductivity to decrease more rapidly than the real components. Such behavior results in Archie's second law (eq. 2.48) in higher saturation exponents for the imaginary part (ν) than for the real part (n). This, however, contradicts the general understanding that polarization would be less affected by saturation than bulk conduction. Even though some variability as been observed for different pore solutions, each material showed either a clear $\nu < n$ or $\nu > n$ behavior. Figure 4.5 plots the two saturation exponents against each other. For materials obeying $\nu < n$, data plot above the dashed line, materials where $\nu < n$ plot below.

Table 4.1: Physical characteristics and saturation exponents of the real (n) and imaginary (ν) conductivity components as determined in evaporative desaturation experiments.

Short symbol	Material type	Φ [%]	S_{por} [μm^{-1}]	D_0 [μm]	AD		Na_2SO_4		$NaCl$	
					n	ν	n	ν	n	ν
S	sandstone	18.77	10.73	22.79	0.73	2.57	1.98	3.64	1.59	2.57
C	sandstone	21.70	50.80	18.25	1.29	3.43	1.36	2.98	0.50	2.29
B	sandstone	19.10	69.17	0.99	0.61	1.75	0.90	1.74	0.68	1.79
Pa	aer. concrete	71.89	54.81	75.17	0.75	2.31	1.48	2.29	-	-
SV	limestone	33.99	2.79	3.02	(0.18)	(0.32)	0.86	0.54	0.90	0.55
Ha	historic brick	25.16	5.19	3.41	1.16	0.80	1.71	1.14	2.32	1.43

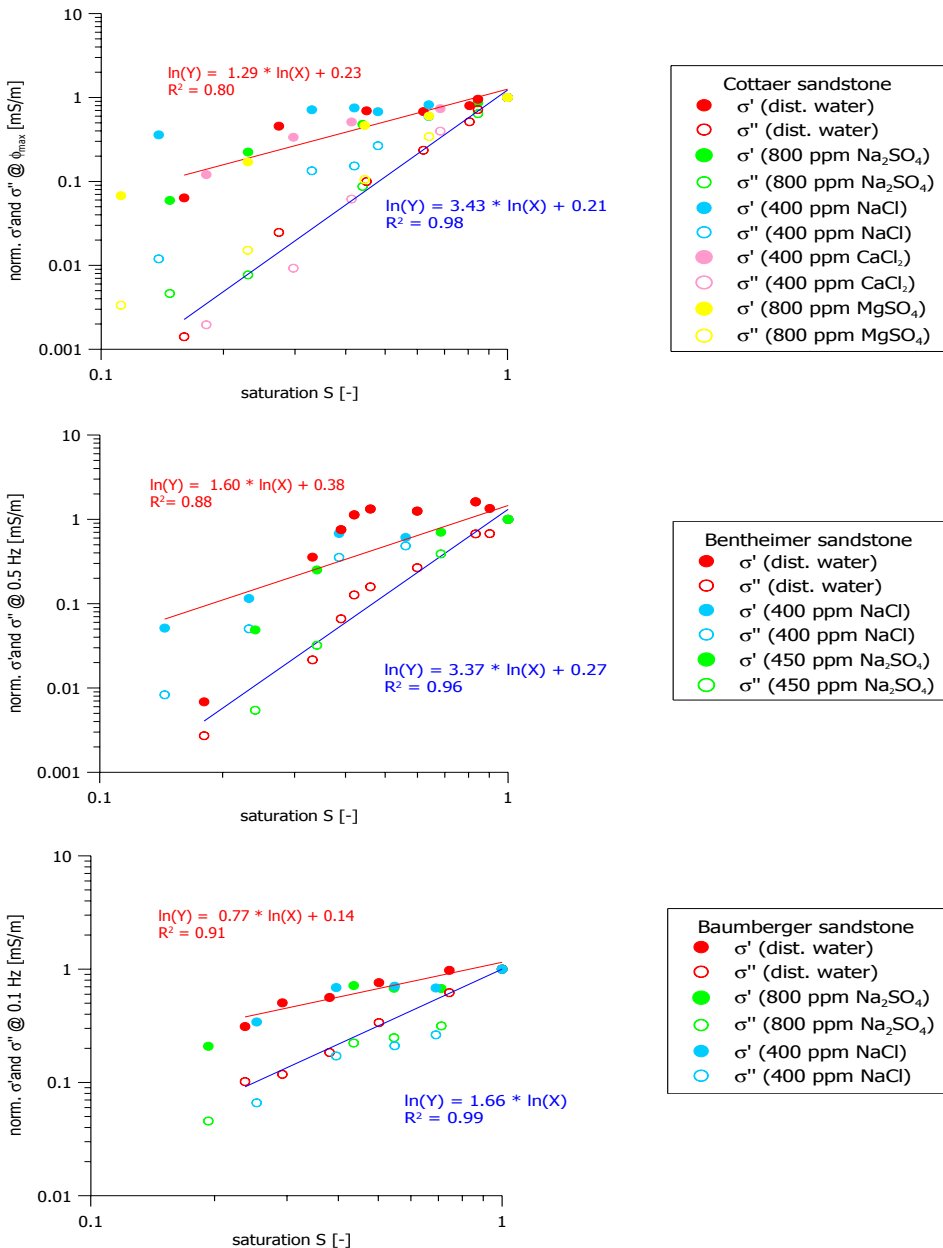


Figure 4.3: Dependence of the real and imaginary conductivity on saturation during evaporative drying. Top: Cottaer sandstone, middle: Bentheimer sandstone, bottom: Baumberger sandstone. The lines show power law fits from which saturation exponents were estimated.

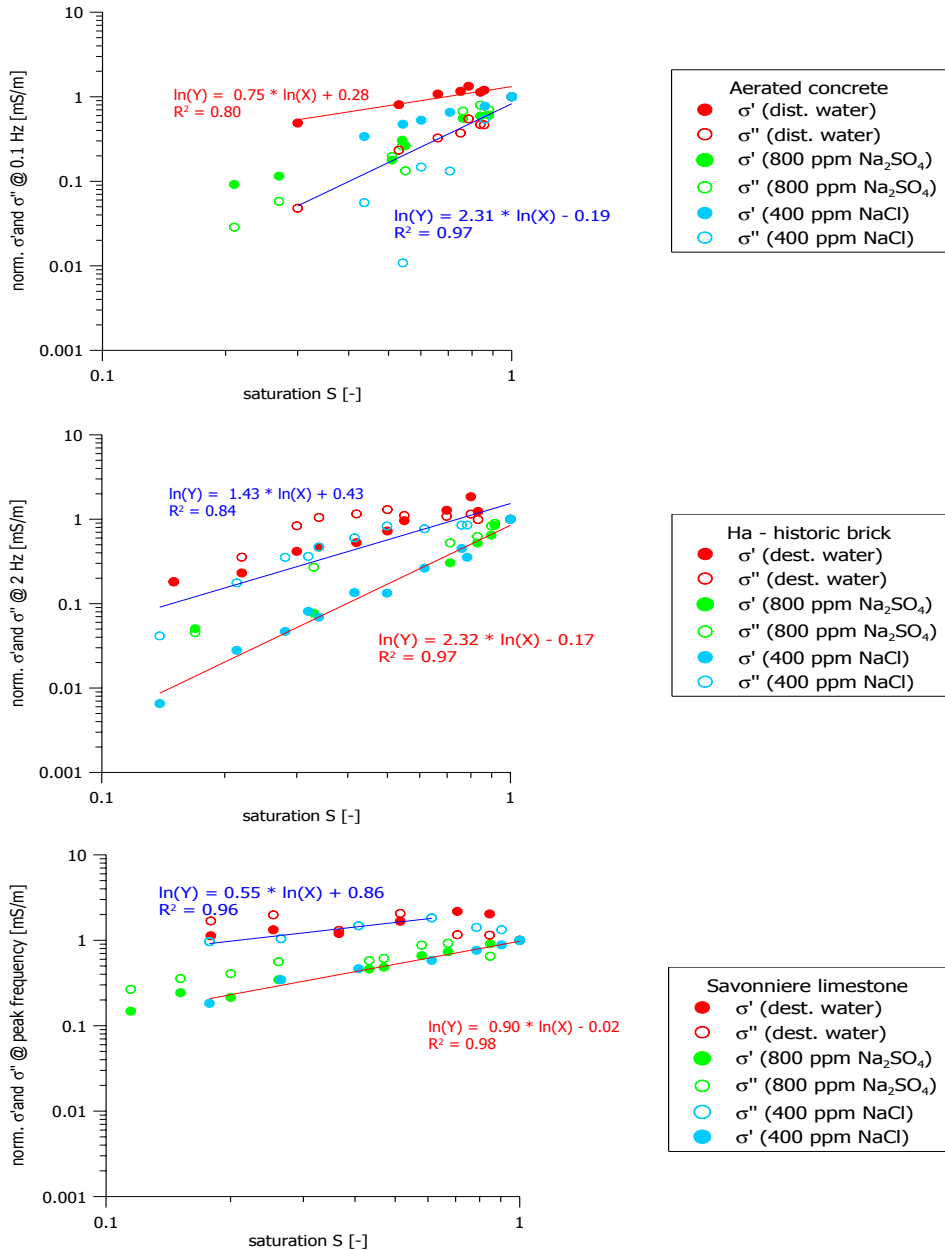


Figure 4.4: Dependence of the real and imaginary conductivity on saturation during evaporative drying. Top: Aerated concrete, middle: historic brick (Ha), bottom: Savonniere limestone. The lines show power law fits from which saturation exponents were estimated.

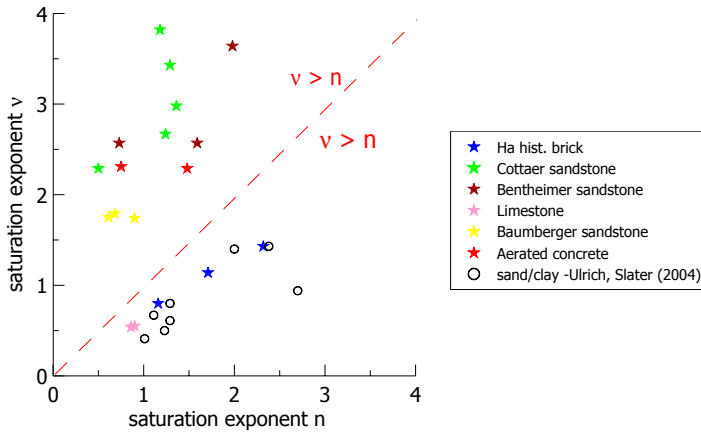


Figure 4.5: Saturation exponents n (real component σ') versus v (imaginary component σ''). The black circles show the results measured by Ulrich and Slater (2004) on unconsolidated sands.

4.3 Summary

In this chapter the effect of reducing saturation on CR behavior has been investigated for six building stone samples. To simulate circumstances as they are most likely in case of a water/salt damage in a real building the samples were evaporatively dried accepting consequently that the fluid salinity increases for each experiment step. It was observed that, irrespective of the original fluid chemistry for most materials the normalized quadrature surface conductivity component decreases more rapidly than the real component. Even clay-rich sandstones did not maintain surface rather than electrolytical conduction for reducing fluid saturations, nevertheless clay minerals do have an irreversible water content. Only for the (mostly amorphous) brick and limestone samples the quadrature conductivity is consistently higher (twice) than the real one, which is the according to the few publications as yet addressed "expected" behavior. Evaluating the entirety of the results in this study and published by other authors, it seems inconclusive to simply assume parameters like porosity, specific surface or dominant pore (grain) size to govern the desaturation pattern. Ulrich's unconsolidated sands had high porosities between 25-40% and as well did the sandstones used in Binley et al. (2005). Contrary, in this study it is the low porosity samples that show "normal" behavior. Binley's samples had similar pore throat sizes like the "abnormal" behaving samples here. The only, nevertheless weak, coherency to be noticed might be, that the normalized quadrature conductivity saturation exponents increased with increasing specific surface (clay content) of the samples.

The C-C parameters τ and m (or m_{norm}) change during desaturation. However, there does not seem to be a universal relationship between the two. In fact, for most materials, which showed C-C relaxation responses at full saturation, the peaks quickly flatten with reducing saturation. For the aerated concrete, which is the sample with the highest

porosity and biggest pore throat size, τ and m are observed to decrease with reducing water content. Oppositely, for the material with the smallest effective porosity and pore size, τ and m increase slightly. In both cases the fluid salinity naturally increases during the evaporative drying procedure, consequently the salinity effect on CR is the same. As discussed in the previous chapter an increasing salinity usually results in a τ and m drop, which could explain the observation for the aerated concrete. In case of the brick other effects must be superimposed and masking this.

5 Electroacoustic experiments

An important problem occurring for the interpretation of CR data is determining the relative contributions of fixed layer and diffuse layer polarizations to the polarization response. The correlation between relaxation time τ and salt concentration of the saturating fluid is tentatively attributed to changes of ion mobility and diffusion coefficients and charge densities in the fixed and diffuse parts of the electrical double layer. However, the electrical and chemical properties and how they change with fluid chemistries is not yet well understood.

Lesmes and Morgan (2001) state that "effective" polarization is primarily a function of the relative amounts of charge in each of the phases. Based on the analysis of effective medium model responses they deduct for Berea sandstone, that fixed layer polarization is much more efficient, since the charge density ($\Sigma_f = 4.8 \times 10^{17} \text{ eq/m}^{-2}$) is nearly an order of magnitude larger than the diffuse charge density ($\Sigma_d = 2.7 \times 10^{16} \text{ eq/m}^{-2}$).

To get an estimation at least of the surface charge densities in the diffuse layer and to observe how it changes with salinity and salt type, electroacoustic measurements on electrolytic suspension were made. The analysis of zeta-potential variations is an important indicator of charge distribution in the diffuse part of the double layer. The charge density of the fixed layer (Σ_f) is most commonly calculated as the difference of total surface charge (Σ_t) (as measured in potentiometric titration experiments) and the diffuse layer surface charge (Σ_d):

$$\Sigma_f = \Sigma_t - \Sigma_d. \quad (5.1)$$

5.1 Zeta-potential

When a porous material having a net surface charge is subject to an electric field, a part of the electric double layer is set into motion, giving rise to a flow of liquid through the capillary system. In case of a negatively charged surface, positive counterions in the diffuse layer will move in the direction of the cathode, dragging the liquid along with them. On the other hand, solvent molecules, which are located close to the wall within the surface of shear, will not move under the influence of an electric field. This surface of shear is assumed to coincide with the outer Helmholtz plane and the corresponding potential in this plane is called the zeta-potential.

The velocity of the liquid rises from a value of zero at the surface of shear to a limiting value, v_{eo} , at an infinite distance from the wall, that is, the point at which the concentration of the positive counterions equals the bulk concentration. The relation between the

electroosmotic velocity, v_{eo} , and the zeta-potential, as derived by Smoluchowski, is given by:

$$v_{eo} = -\frac{\epsilon_0 \epsilon_r \zeta}{\eta} E, \quad (5.2)$$

where E is the applied electric field strength, ζ is the zeta-potential, and η its viscosity, assuming that ϵ and η have the same values in the double layer as in the bulk solution.

The thickness of the double layer ($1/\beta$, compare eq. 2.1) depends upon the concentration of ions in solution and can be calculated from the ionic strength of the medium. The higher the ionic strength, the more compressed the double layer becomes. The valency of the ions will also influence double layer thickness: a trivalent ion such as Al^{3+} will compress the double layer to a greater extent in comparison with a monovalent ion such as Na^+ .

Electrophoresis:

When an electric field is applied across an electrolyte, charged particles suspended in the electrolyte are attracted towards the electrode of opposite charge. Viscous forces acting on the particles tend to oppose this movement. When an equilibrium is reached between these two forces, the particles move with constant velocity. This velocity (likewise referred to as *electrophoretic mobility*) is dependent on the strength of the electric field or voltage gradient, the dielectric constant of the medium, the viscosity of the medium and the zeta-potential. zeta-potential is related to the electrophoretic mobility by the Henry equation:

$$U_E = \frac{2\epsilon\zeta f(\kappa a)}{3\eta}, \quad (5.3)$$

where U_E is the electrophoretic mobility, and $f(\kappa a)$ the Henry function.

The zeta-potential has been observed to be sensitive to the valence of the ions and is approximately reduced by the charge of the cation, unless specific absorption takes place like in case of Al^{3+} (Lorne et al., 1999).

O'Brien (1988) developed the theory how to use a sound wave signal to estimate the dynamic (frequency dependent) mobility. For thin double layer systems in dilute suspensions this quantity can be related to the static (dc) mobility and, hence, the zeta-potential of the particles. The assumption, that the double layer thickness is thin compared to the particle radius is usually valid, if their radius is greater than $0.1 \mu m$, which is the case for all investigated materials. O'Brien (1988) pointed out, that for particles, for which the dielectric permittivity is small compared to that of water, the dynamic mobility, μ_d , is related to the zeta-potential by the simple formula:

$$\zeta = \frac{\mu_d \eta}{\epsilon} |G(\alpha)^{-1}| = \frac{ES\Delta\eta}{\epsilon c \Delta d \phi' G_f} |G(\alpha)^{-1}|. \quad (5.4)$$

$G(\alpha)$ is the frequency and size-dependent inertial contribution to the dynamic mobility, given by:

$$G(\alpha) = \left[1 - \frac{i\alpha(3 + 2(d_m - d_0)/d_0)}{9 \left(1 + (1 - i)\sqrt{\left(\frac{\alpha}{2}\right)} \right)} \right]^{-1} \quad (5.5)$$

with d_m being the solid's density and d_0 that of the solvent. ν is the kinematic viscosity of the suspension medium ($= \eta/d_0$). The function G varies from a value of 1 for particles of size less than about $0.1 \mu m$ to about 0.5 for particles of radius $1 \mu m$ and down to as little as 0.05 for a radius of $10 \mu m$.

Equation 5.4 is the Helmholtz-Smoluchwski equation modified by the factor $|G(\alpha)^{-1}|$, a damping term which is a function of the frequency ω of the electric field:

$$\alpha = \frac{\omega a^2}{\nu}, \quad (5.6)$$

where a is the particle sizes present in the suspension. For a solid suspension the measured ESA signal is a combination of two signals: one for the solid and one for the background ionic solution. The effect of electrolyte solution is discussed in Desai et al. (1993) and a correction procedure proposed. The ion signal is, in most cases, relatively small, but their background can require correction, when the ionic strength is very high or the measurements are made close to the isoelectric point (iep). Hackley and Malghan (1993) state, that a blank measurement of the ion signal from an equivalent solution followed by a simple subtraction procedure will generally suffice as background correction. The ion signal is nearly pH independent in the range from pH 5 to 9.

Another factor, that may need correction is the effect of particle size if materials with a broad particle size distribution are investigated (James et al., 1992). It is necessary to estimate an effective size to input into the measurement software so that the calculated zeta-potential can be as accurate an estimate as possible. Robert Hunter discusses a program (gcac1cfu1.wk1) to determine effective radii of materials of somewhat broad particle size distributions in a Matec Application Note (Hunter, -). Since this routine could not be made available through the course of the investigations reported here the parameter d_{50} as inferred from light scattering has been used instead; a procedure that is in agreement with Dr. Vincent Hackley, NIST, (oral communication).

Experimental Setup

The electroacoustic measurements reported here use the electrosonic analysis (ESA) method and were carried out on the ESA 9800 (Matec Applied Science, 2006) instrument. The measurement cell assembly of the system contains a SP80 sensor, a 300 ml Teflon sample cell and a Teflon cell head, probes for pH, temperature and conductivity as well as an overhead impeller mixer. The SP-80 probe consists of two parts, that is the main probe body and a removable end cap. The main probe body sensor consists of an acoustic delay line with a piezoelectric transducer mounted on one end and a solid gold electrode

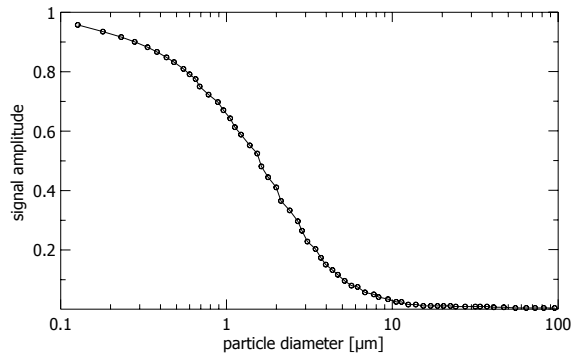


Figure 5.1: Signal loss of zeta-potential in electroacoustic measurements as a function of particle size after Flatt and Ferraris (2002).

laminated to the other. The cross bar of the probe cap forms the second electrode and it is positioned plane and parallel to the electrode of the main body of the sensor. The electrode spacing is an odd integer multiple of one half the acoustic wavelength in the colloid. The sample flows in to fill the region between the electrodes. In this device a 1 MHz alternating electric field is applied to the colloid causing an oscillatory particle motion which generates sound waves.

Sample preparation

Sample materials were crushed down to $150 \mu\text{m}$ grains using mortar and pestle. These grains were grind further in a micronizing mill until average particle sizes in the range of $1\text{-}10 \mu\text{m}$ were achieved with 80% of the material being smaller than $5.5 \mu\text{m}$. The particle size distributions of the materials were determined using light scattering prior to each measurement. Figure A.1 in the appendix shows the results, from which the median particle size d_{50} was inferred. For the measurement a requisite weight of electrolyte solution is added to a known weight of sample material. The suspension was magnetically stirred until well mixed and then dispersed using an immersion-type ultrasonic horn for a period of about 2-3 minutes.

For the sake of completeness, should be noted, that particle size, if larger than about 50 nm, can be a problem for electroacoustic measurements (Dr. V. Hackley (NIST), oral communication). If the particles are very large (bigger than a few microns), this effect is difficult or impossible to account for. A graph showing how the particle size in suspension attenuate the measured zeta-potential is given in Fig. 5.1. Since all particles used in this experiment were $3 \mu\text{m}$ or less in size, it is, however, assumed, that the data quality is reasonable.

Data Analysis

For the suspensions used here the background¹ corrections were only very small. Nevertheless, they have been made for each salt and each material (software setup) respectively.

Fig. 5.2 illustrates the zeta-potentials as measured for Cottaer sandstone in $NaCl$, Na_2SO_4 , $CaCl_2$ and $MgSO_4$ suspensions as a function of electrolyte conductivity (salt concentration). The effect of changing valence of the dominant cation in the suspension is striking. The zeta-potential is found to decrease for monovalent salts from approximately -60 to 0 mV for electrolyte conductivities up to 1000 mS/m (that is salt concentration up to 0.01 mol/L). For divalent salts it is generally significantly smaller at equivalent concentrations. As an example, the background measurements for Cottaer sandstone are illustrated in Fig. 5.2 (bottom). With increasing ion content the scattering effect of the salt ions in solution increases.

The results of $NaCl$ and $CaCl_2$ solutions for all materials investigated are compared in Fig. 5.3. Table 5.1 gives the measured zeta-potentials for each, when saturated with distilled water as well as $NaCl$ and $CaCl_2$ solution. As for Cottaer sandstone, divalent cations reduce for all the zeta-potential much more even when only a small quantity of salt is added. This observation is generally in agreement with the discussion in Lorne et al. (1999) and the, herein cited, three layer EDL model published in Davis et al. (1978). Divalent cations shield the negative charge of the EDL more efficiently than monovalent ones.

As inferred from streaming potential measurements Lorne et al. (1999) report the effect of changing cation types for crushed Fontainebleau sandstone to be apparently not solely dependent on the actual ionic radius. They observed the zeta-potential for Na^+ to be consistently smaller than for Li^+ and K^+ , while the size of the lithium ion is about half the size of the potassium ion. For divalent cations the observed zeta-potentials were ordered according to their ionic size, $\zeta(Mg^{2+}) > \zeta(Ca^{2+}) > \zeta(Ba^{2+})$.

It is known, that zeta potential generally depends largely on the pH of the suspension². For the results presented here, the focus is how zeta potential varies with salt content and type, however, the variation of zeta potentials and pH are given for each measurement in Fig. C.7 in the appendix. It can be seen, that for $NaCl$ and Na_2SO_4 the pH did not change throughout the test series. For the divalent salts some pH variation is apparent, however, since even the largest pH changes were only within 0.5 pH units, they have been neglected.

¹Background means usually the supernatant of a powder suspension, however, since not enough sample material was available to do so, the background as used here was distilled water plus salt; the author is aware that this approach does not account for possible dissolving ions from the powders

²Imagine a particle in suspension with a negative zeta-potential, if more base is added to this suspension then the particles will tend to acquire a more negative charge. If acid is then added to this suspension a point will be reached where the negative charge is neutralized and any even further addition of acid may cause a build up of positive charge. Hence, zeta-potential curves will be positive at low pH and lower or negative at high pH.

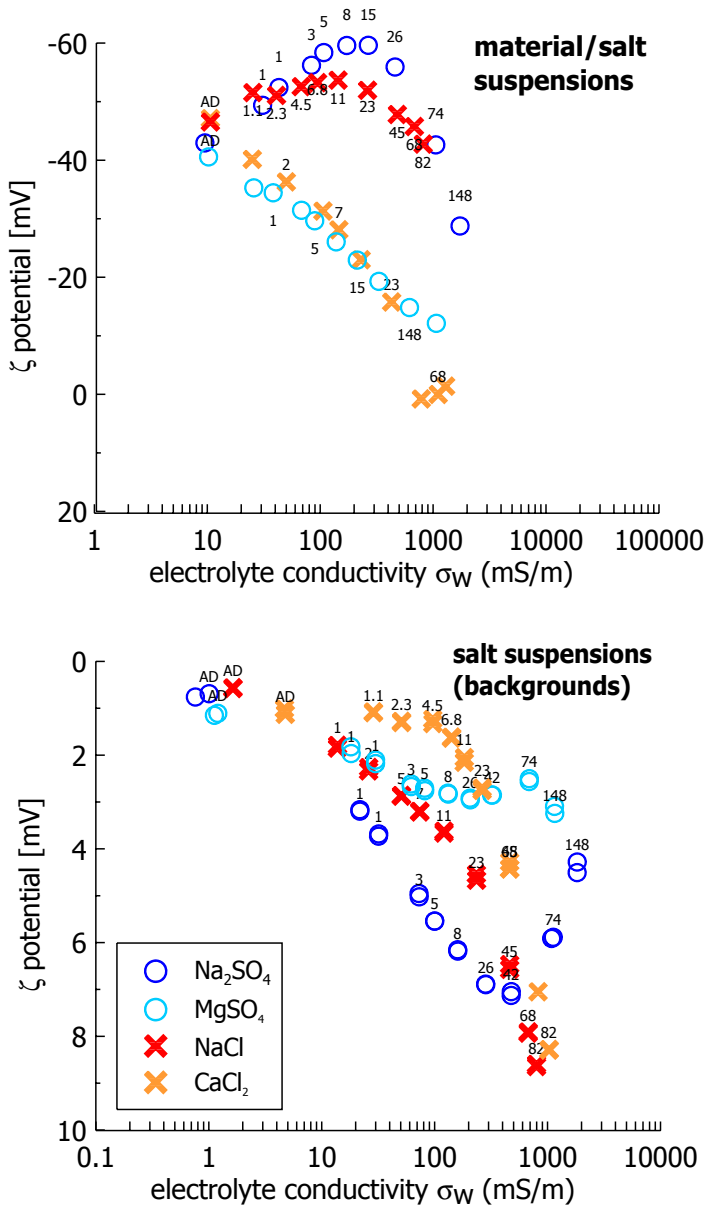


Figure 5.2: Top: zeta-potential inferred from electroacoustic measurements using crushed and micronized Cottaer sandstone, as a function of suspension conductivity. Bottom: zeta-potential inferred from electroacoustic measurements using only ionic solutions and *no* material powders. The results of different ions varying in valence are compared. Black labels denote the salt concentration in units mmol/L.

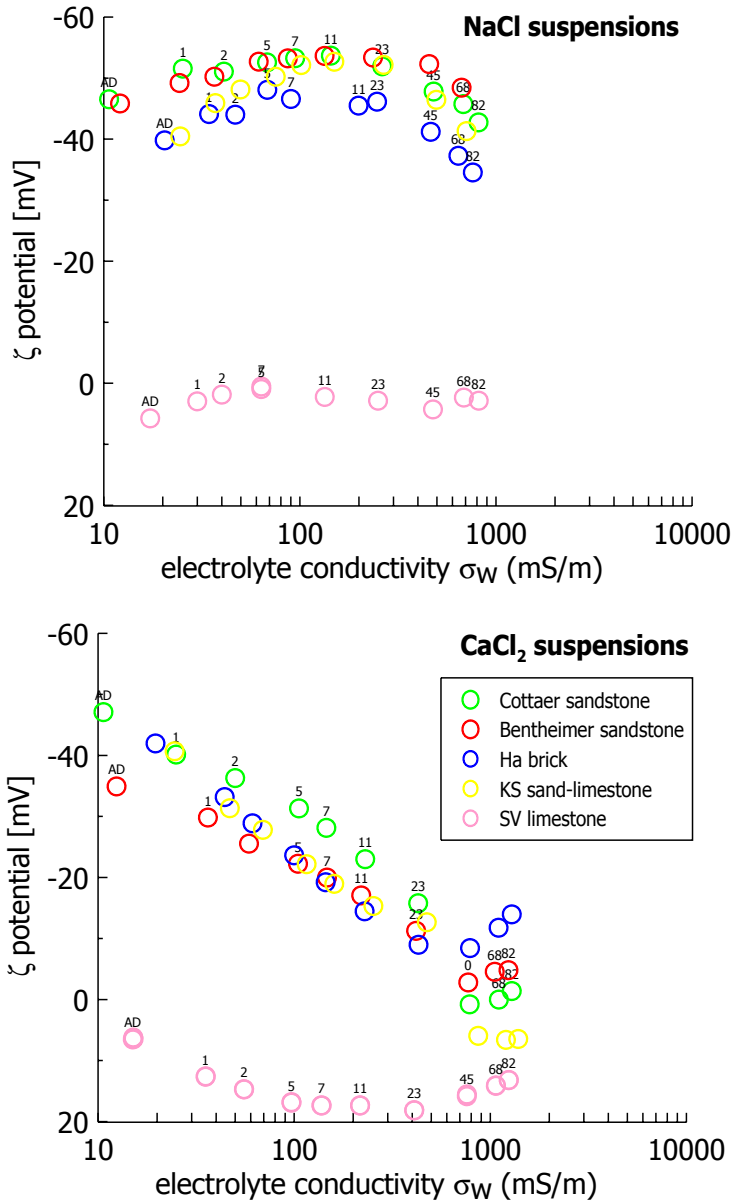


Figure 5.3: Comparison of the zeta-potential inferred from electroacoustic measurements on crushed and micronized Cottaer and Bentheimer sandstones, a historic brick (type Ha), a sand-limestone (type KS) and a limestone (type SV) sample as a function of NaCl (top) and $CaCl_2$ (bottom) suspension conductivity. Black labels denote the salt concentration in units mmol/L.

Table 5.1: Physical properties and zeta-potentials measured for suspensions in distilled water, and in $\approx 0.011 \text{ mol/L}$ (400 ppm) NaCl and CaCl_2 respectively.

SHORT SYMBOL	MATERIAL TYPE	d_m [g/ccm]	d_{50} [μm]	r_{50} [μm]	ζ (AD) [mV]	ζ (NaCl) [mV]	ζ (CaCl_2) [mV]
S	sandstone	2.6372	3.10	1.28	-45.95	-56.52	-19.47
C	sandstone	2.6587	2.55	1.55	-46.55	-53.49	-23.00
SV	limestone	2.7187	1.58	0.79	6.04	2.24	17.35
K	sand-limestone	2.5845	2.28	1.14	-40.80	-52.69	-15.31
Ha	historic brick	2.6456	2.57	1.28	-39.80	-45.50	-14.47

5.1.1 Surface charge density

Experimental Setup

The ESA 9800 device can also perform a pH titration, plotting pH as a function of added base or acid. From this the magnitude of titration charge, which is usually regarded as the total surface charge can be determined. In order to obtain the surface excess, the amount of titrant uptake by solution species must be known. This is done by performing a background titration on a supernatant solution.

Titration curves must be corrected both the acid added initially and the amount of titrant taken up by the solution species. The first correction involves a point-for-point subtraction of the base titrated (C_{base}) at each pH value, from the initial amount of acid added (C_{acid}). This has to be done for both suspension and background titrations:

$$\Delta C = (C_{acid} - C_{base}). \quad (5.7)$$

In this equation also the generally accepted formalism of proton absorption being a positive and hydroxyl absorption being a negative uptake is defined.

The second correction regards the influence of the solution used for suspension. It is accomplished by subtracting the background titration curve from the suspension curve. Hence, the net surface excess of acid or base ($\Delta\Gamma$) in [meg/L] is obtained as:

$$\Delta\Gamma = (\Gamma_{H^+} - \Gamma_{OH^-}) = (\Delta C_{suspension} - \Delta C_{background}). \quad (5.8)$$

This operation yields the net uptake of acid or base by the material surface. In order to find the common interception point corrected titrations have to be made at least at three different ionic strengths. Results are plotted as the net surface excess of acid or base versus pH. The common interception point identifies the point of zero charge (pH_{pzc}).

The surface charge density Σ_t can be calculated from the net surface excess as a function of solution pH using:

$$\Sigma_t \left[\frac{\mu\text{C}}{\text{cm}^2} \right] = \frac{\Delta\Gamma e N_A * 1000}{S} \quad (5.9)$$

with N_A being the Avogadro's constant ($6.02214 \times 10^{23} \text{ eq}^{-1}$), e the electron charge ($1.602 \text{ e-19 Coulomb}$) and S the total surface area (cm^2/l). The latter can be calculated from the powder mass concentration and the specific surface charge area as inferred from BET measurements. Surface charge densities may also be expressed as the number of equivalent electron charges per unit area (typically in nm^2):

$$\Sigma_t \left[\frac{eq}{\text{nm}^2} \right] = 0.062422 \cdot \Sigma_t \left[\frac{\mu\text{C}}{\text{cm}^2} \right]. \quad (5.10)$$

Sample Preparation

The sample suspensions are prepared the same way as for the electroacoustic measurements described above. Prior to starting the titration a specific salt amount of salt has to be added and acid in order to decrease the pH down to a value, where the titration curve is required to start. Titrations of at least three different ionic strengths have to be analyzed in order to get a common intersect and determine the point of zero charge (pzc).

Data Analysis

The titration curves of Cottaer sandstone samples for three different ionic strengths are shown in Fig. 5.4. For Cottaer sandstone the three titration curves are very similar and seem almost independent of ionic strength; no common intersection could be found. Pure quartz is observed have its pzc around pH 2.7 or 3. That this common intersect could not be found is probably due to the fact that this sandstone type contains a great variety of clay minerals and maybe other components, which can cause the pzc to change significantly. However, interestingly for Cottaer sandstone, between pH 7 and 8, the net surface excess $\Delta\Gamma$ is between 1 and 0.5 meq/L. According to eq. 5.9 and 5.10 the total surface charge density is $\Sigma_t = 1.37$ to $2.74 \times 10^1 \mu\text{C}/\text{cm}^2$ or 0.85 to $1.71 \times 10^{18} \text{ eq}/\text{m}^2$.

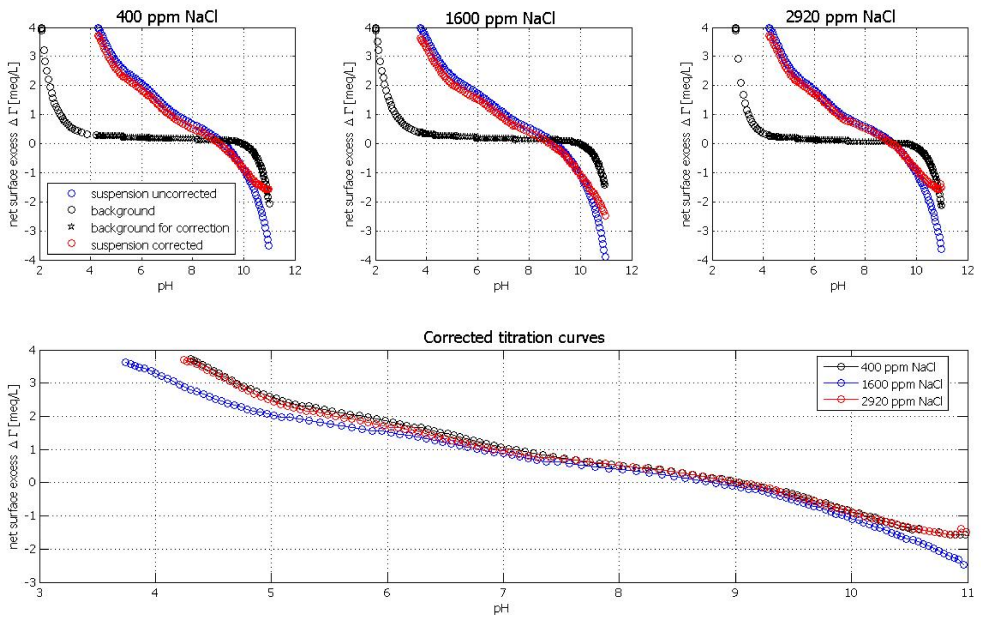


Figure 5.4: Cottaer sandstone, titration curves. Upper three diagrams show the titration curves for one ionic strength including the uncorrected suspension, the background measurement as well as the corrected suspension curves. The bottom diagram includes the background corrected titration curves for the three ionic strengths.

5.2 Discussion

Since the general behavior of the zeta-potential as it changes with salt concentrations looks very similar to what has been observed for the conductivity components σ'' and/or the ratio σ''/σ' (compare Fig. 3.15 to Fig. 3.17) these quantities are plotted against one another. Figure 5.5 (top) presents the correlation of zeta-potential and imaginary conductivity. In a log-linear plot the two exhibit some weak correlation, even though this trend is not as evident anymore when looking at each material separately. The same, even so still weaker, can be noticed for the relation of zeta-potential and the ratio σ''/σ' in Fig. C.8 (top) in the appendix. It is unclear, why for divalent cations the zeta-potential decreases with concentration while the imaginary conductivity increases.

The surface charge density Σ_d in the diffuse layer of the EDL can be calculated from the zeta-potential (Bard and Faulkner, 2001):

$$\Sigma_d = -\sqrt{8k_B T \epsilon_r \epsilon_0 n^0} \sinh\left(\frac{ze\zeta}{2k_B T}\right), \quad (5.11)$$

where k_B particle radius, T absolute temperature, ϵ_r dielectric constant, ϵ_0 dielectric permittivity of free space, n^0 concentration number of each ion in a symmetric electrolyte, e electronic charge, z ionic charge.

For dilute aqueous solutions at 298° K, the constants can be evaluated to give:

$$\Sigma_d = 0.1174\sqrt{c} \sinh(19.5z\zeta), \quad (5.12)$$

where Σ_d surface charge density [C/m²], c electrolyte concentration [mol/L], z electronic charge (for monovalent ions = 1, for divalent ions = 2), ζ the zeta-potential [V].

It seems, therefore, not unlikely to assume that imaginary conductivity depends either more upon diffuse or fixed surface charge density as opposed to zeta-potential directly. Figure 5.5 (bottom) shows the diffuse layer charge as a function of imaginary conductivity. Clearly, for one material, namely Cottaer sandstone, a log-log linear relationship results. This becomes even more striking, when the results are displayed for each material separately (5.6). As well for the others this relationship seems somewhat more substantial than the correlation of imaginary conductivity and zeta-potential. In eq. 5.12 the zeta-potential appears as a factor in the sinh-function. It can easily be shown, that in case where Σ_t is mostly salinity independent (like for Cottaer sandstone) Σ_d strictly increases even though the zeta-potential appears to vary. The same holds for the fixed surface charge Σ_f but with a negative slope (in other words: if Σ_d increases, Σ_f must decrease vice versa; compare eq. 5.1 and suppose Σ_t to be salinity independent.) For Cottaer sandstone titration measurements could be made using NaCl suspensions. Hence, as the titration curves lay almost on top of each other it seems justified to assume at pH 8 a constant, salinity independent, total surface charge of $8.55 \times 10^{17} \text{ eq/m}^{-2}$ ($\Delta\Gamma = 0.5 \text{ meq/L}$, compare Fig. 5.4). The diffuse layer charge density is calculated after eq. 5.12 and the fixed layer charge is taken to be the difference of Σ_t and Σ_d . Correlating these charge

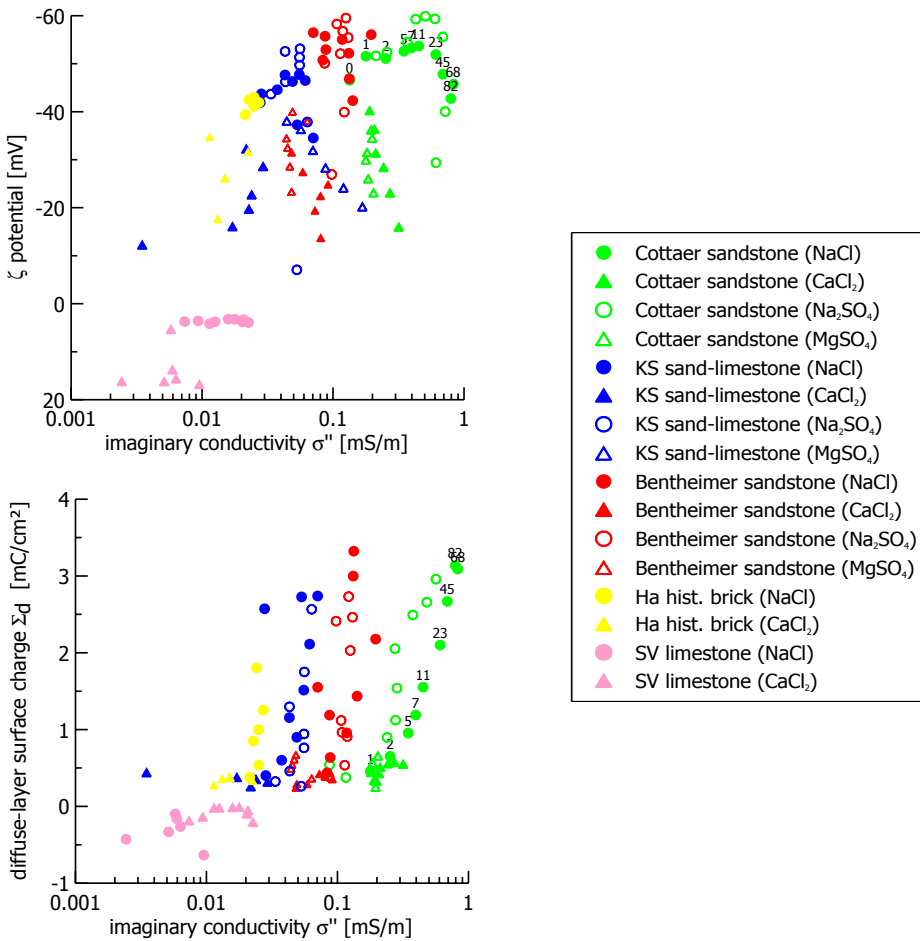


Figure 5.5: Zeta potential (top) and diffuse layer charge Σ_d (bottom) as a function of imaginary conductivity σ'' for all materials and salt concentrations. Black labels denote salt contents in units mmol/L exemplarily for Cottaer sandstone.

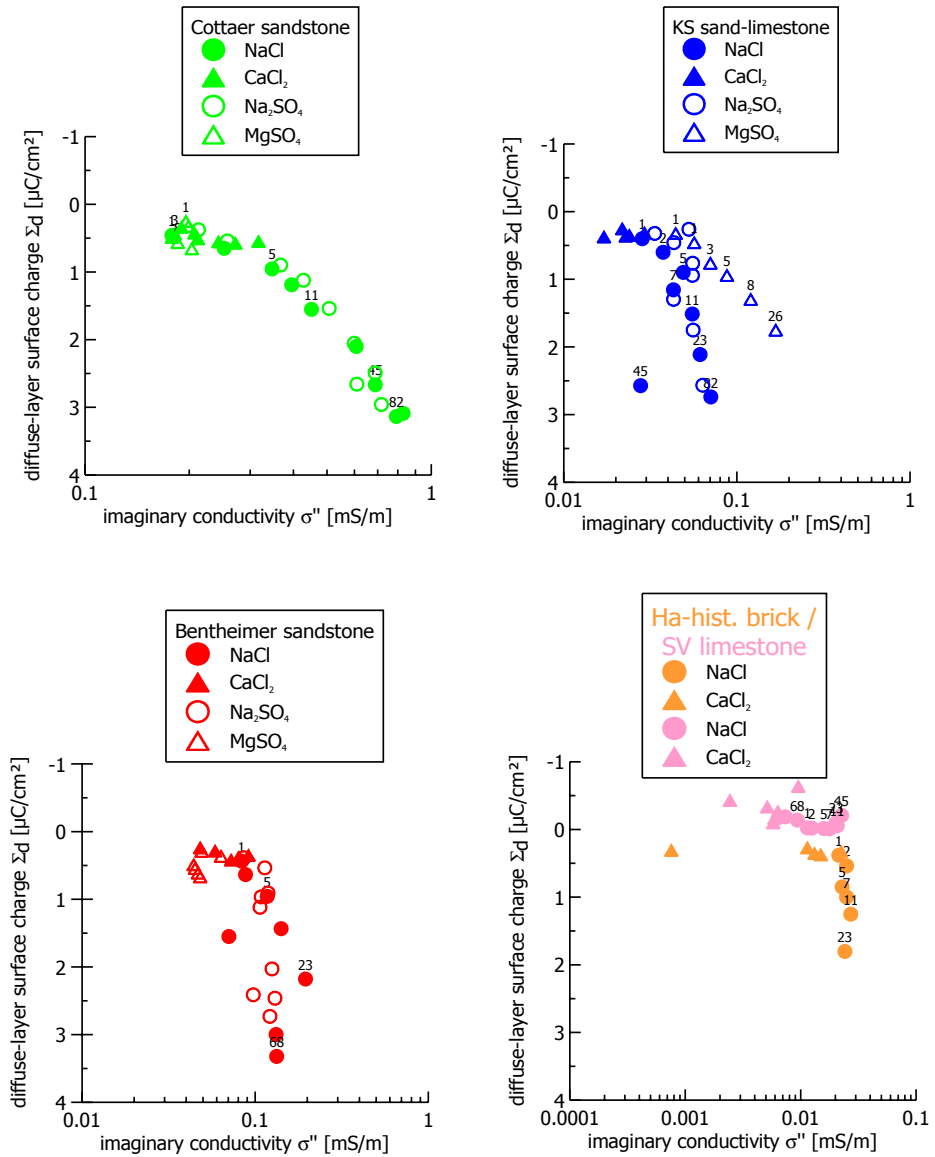


Figure 5.6: Diffuse layer charge Σ_d as a function of imaginary conductivity σ'' for each material separately. The black labels denote the salt concentration in mmol/L.

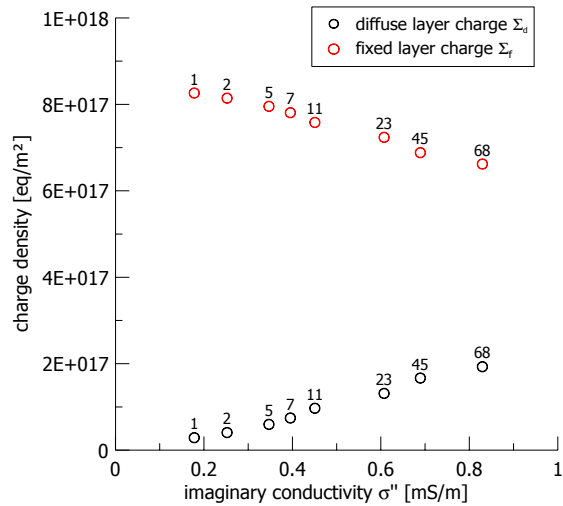


Figure 5.7: Fixed layer charge density Σ_f and diffuse layer charge density Σ_d as a function of fluid conductivity σ'' for Cottaer sandstone and NaCl solutions.

densities to the imaginary conductivity results in positive correlation for the diffuse and a negative correlation for the fixed layer charge densities (see Fig. 5.7).

In general, it is understood, that the total surface charge depends on fluid chemistry, and probably for many materials, also on salinity. The straight forward calculation presented above may not be applicable as easily for other building stones or even other salt types in combination with same material. Titrations made on Bentheimer sandstone also using NaCl suspension indicated instead that the total surface charge can as well be salinity dependent and like the diffuse layer charge possess some maximum value at intermediate concentrations.

5.3 Summary

In the preceding sections the electroacoustic properties of five building stone samples were investigated using the electrosonic analysis (ESA) method. The zeta-potentials of grinded and micronized (d_{50} ranging between 3.1-1.6 μm) material powders in suspension were measured as a function of salt type and concentration. For all samples (two clay-rich sandstones, sand-limestone, brick) but one (limestone) the zeta-potentials were found to decrease for monovalent salts from approximately -60 to 0 mV for salt concentration ranging between 1 to 100 mmol/L. For divalent salts they are generally significantly smaller at equivalent concentrations.

There seems to be some general, even though weak, relationship between zeta-potential and imaginary conductivity. If these two quantities are plotted against each other, a positive log-linear relationship is apparent. In contrast, the dependence of imaginary conductivity on diffuse layer charge density, which can be obtained from the zeta-potential,

is observed to scatter significantly. This may be indicative for the general understanding of polarization processes in the low frequency range. There is still much discussion about their origin in terms of which ions, diffusion constants or length scales are crucial. For one material (Cottaer sandstone) the total surface charge could be determined in an autotitration experiment. For the salt concentrations (and pHs) used in this study, the surface charge density of this material can be considered constant. Knowing the total as well as the diffuse layer charge, the fixed layer charge is usually taken to be their difference. For Cottaer sandstone, hence, results that the fixed layer charge decreases and the diffuse layer charge increases with every addition of salt (here NaCl). This actually implies, that, even though the fixed layer charge is about one order of magnitude higher, the imaginary conductivity correlates with the amount of the more mobile ions in the diffuse part of the electrical double layer.

6 Microstructure based Impedance Response Computing

The materials under investigation in this study can be considered as being composites or random agglomerations of different property material at various length scales. Because of their randomness, their properties cannot be computed analytically, but instead require numerical computation basing on microstructural information. Here, rather than exploring differences between model results using real micrographs, it will be determined whether controlled changes of characteristic length scales in simplified microstructures yield useful general observations.

6.1 Finite Difference Program AC2D

AC2D is written in FORTRAN 77 and operates on an arbitrary general image that is read from a file. The digital images do not have to have the same dimension in each direction; however, pixels have to be square with $a = b = 1$ in arbitrary units. AC2D is a finite difference program for a.c. (or d.c.) problems, being set-up for a conductivity tensor that is diagonal, but can have different terms along the diagonal for the x and y directions. The program solves for the effective conductivity of a material composed of different conducting and non-conducting phases, either at zero or a finite frequency. The effective properties of a composite are defined simply in terms of the averages of various quantities over the system (Garboczi, 1998).

The finite difference program AC2D is based on a solution of Kirchhoff's law for a conductance network, which is equivalent to solving Laplace's equation. AC2D uses the conjugate gradient method to solve the finite difference representation of Laplace's equation for complex conductivity problems with periodic boundary conditions. In the following a short overview of the derivation of the finite difference form of Laplace's equation is given according to Garboczi (1998).

The charge conservation law implies

$$\nabla \cdot \mathbf{J} + \frac{\partial \rho}{\partial t} = 0 \quad (6.1)$$

and becomes for steady state, that is if currents are steady in time, simply

$$\nabla \cdot \mathbf{J} = \nabla \cdot (\sigma \mathbf{E}) = 0 \quad (6.2)$$

or, in regions of constant conductivity,

$$\sigma \nabla^2 V = 0 \quad (6.3)$$

with V being the position dependent potential or voltage. Between phases having different conductivities, the boundary conditions are that the current normal to the interface and the potential are continuous. Consider a region of uniform conductivity, and a point (i,j) in this region, in the middle of a pixel. If the voltage at (i,j) is $u(i,j)$, then, to second order in the pixel dimensions, the potential at $i \pm 1$ or $j \pm 1$ is

$$u(i \pm 1, j) = u(i, j) \pm a \left[\frac{\partial u}{\partial x} \right]_{i,j} + \frac{1}{2} a^2 \left[\frac{\partial^2 u}{\partial^2 x} \right]_{i,j} \quad (6.4)$$

$$u(i, j \pm 1) = u(i, j) \pm b \left[\frac{\partial u}{\partial y} \right]_{i,j} + \frac{1}{2} b^2 \left[\frac{\partial^2 u}{\partial^2 y} \right]_{i,j} \quad (6.5)$$

where $\Delta x = \pm a$ and $\Delta y = \pm b$, and a and b are the dimensions of the pixel in arbitrary units. Then the finite difference Laplace's equation, in terms of the 1D label m and the six nearest neighbors, can be obtained by adding together the above four equations in pairs and solving for the 2nd derivative terms. The first derivations cancel out, the gradient squared is formed from the sum of the second derivatives, and Laplace's equation in finite difference form, at each node m , becomes

$$\sum_n \sum_{m,n} [u(n) - u(m)] = 0 \quad (6.6)$$

where $\sum_{m,n}$ is the conductance of the bond connecting node m to its nearest neighbor with nearest neighbor label n , the sum is over the $n = 1$ to 4 nearest neighbors, and for convenience, both sides of eq. 6.6 are multiplied by the volume of the pixel $a \cdot b$. The values of $\sum_{m,n}$ are $\sum_{m1} = \sum_{m3} = \sigma * b/a$, $\sum_{m2} = \sum_{m4} = \sigma * a/b$, with neighbors (1,2) in the (x,y) and neighbors (3,4) in the $(-x,-y)$ directions. This equation is formally identical to solving Kirchhoff's laws of zero net current into each node for this conductance lattice, where the conductances are those of a pixel of material with a given conductivity tensor in a given direction. Therefore formally the length of the pixel appears in the conductance. Note, that the finite difference programs are set up for square pixels, with $a = b = 1$.

There is an equation like (6.6) for each node m in the system. Putting all these equations together, a global equation can be written: $A_{mn} u_n = 0$. If a quadratic form out of this matrix A is built, $1/2 u A u$, then this form is extremized, when its gradient with respect to u is zero. The formal problem being solved is then the minimization of the quadratic form $1/2 u A u$, where u is the vector of voltages, and A a sparse matrix of the conductances of all bonds in the problem.

Periodic boundary conditions are maintained using a shell of imaginary sites around the main system, as shown in Fig. 6.1. The figure illustrates, there are nine real sites in this 3×3 pixel system, labelled 1-9, and 12 imaginary sites, labelled in italics according to which real site they correspond. So, for example, if the strength of the field is $1/3$, there

exponent z (compare Fig. 6.2) was equal to 1. The author is aware of the fact, that lowering z to 0.5 (Warburg model, or between 0.1 - 0.6 for Cole-Cole model) could affect the model results noticeably.

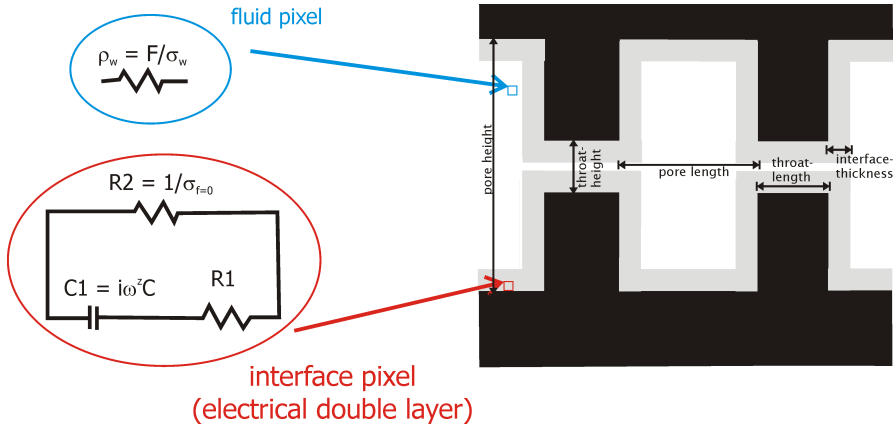


Figure 6.2: Equivalent circuit used in the approach to model microstructural effects on complex resistivity behavior. The model is similar to the traditional Debye model simulating the electrical double layer in a parallel connection of resistor and resistor and capacitor in parallel.

Using this approach the parameter study of the most critical microgeometrical features has been conducted, results of which are outlined in the following. All pictures used consist of 128x128 pixels. It is unknown to the author whether the electrical double layer must be assumed to take similar conductivity values as the fluid, higher (due to higher ion concentration) or even lower (due to ion absorption and lower mobilities). Consequently, most calculations have been done for three different conductivity "environments", that are $\sigma_w > \sigma_{il}$, $\sigma_w = \sigma_{il}$, $\sigma_w < \sigma_{il}$.

6.2.1 Interface shape

In order to develop some more general understanding of how the interface shape can effect CR behavior a number of test microstructures have been generated and simulated using varying conductivities. The first series of models encompasses six models and different types of interfaces (compare Fig. 6.3). Results are given in the bottom fraction of the picture. The first row of phase and amplitude spectra represents a high, the second an intermediate and the third a low fluid (bulk) conductivity σ_w . Conductivity values are given in the figure caption.

Analyzing the results shows that the relation of fluid to interface conductivity plays an important role on the complex resistivity result. If σ_w is very high, the interface shape does not affect the CR result by much. The lower it becomes (compare at $\sigma_w = 0.0001$ S/m) the more vary the results for the particular models. The more discontinuous, or interrupted the interface becomes, the more the phase maximum shifts towards lower frequency (see Fig. 6.3 bottom).

6.2.2 Developing pore throat

Three sets of models were generated to study the effect of a pore throat. In the one set the interface is continuous and lines the pore. In the other two the interface is discontinuous and exists (mimicing an electrical behavior like described in Titov et al. (2002) by the existence of "selective" zones) only in the pore throats. The two discontinuous models differ in their throat (selective zones) lengths. Similar to the previous models calculations were made for three different fluid conductivities and constant interface properties.

Model set 1 - continuous interface The first set of models, which have a continuous interface, is shown in Fig. 6.4 (top). For these models the maximum phase increases and move towards lower frequency with decreasing pore throat size. Moreover, there seems to be some dependence on fluid conductivity for this shift. The peak position changes most if the fluid conductivity is high and it practically disappears as it gets very low.

Model set 2 - discontinuous interface The second model set is shown in Fig. 6.5 (top). The interface exists only in the throat being shorter than the pore 'belly'. As in the case of the previous model the peak phase shifts increases and shifts to lower frequency when the throat narrows. Contrary to what was observed for the first model for the lowest fluid conductivity a frequency shift of the resistivity phase is observed. Again it holds that with decreasing fluid conductivity the amount by which the peak phase displaces becomes less.

Model set 3 - discontinuous interface The third model set is shown in Fig. 6.6 (top) and comprises six models with discontinuous interface, but now with equal length pore belly and throat parts. For these models the phase peak again increases, but is independent of fluid conductivity and does not change position.

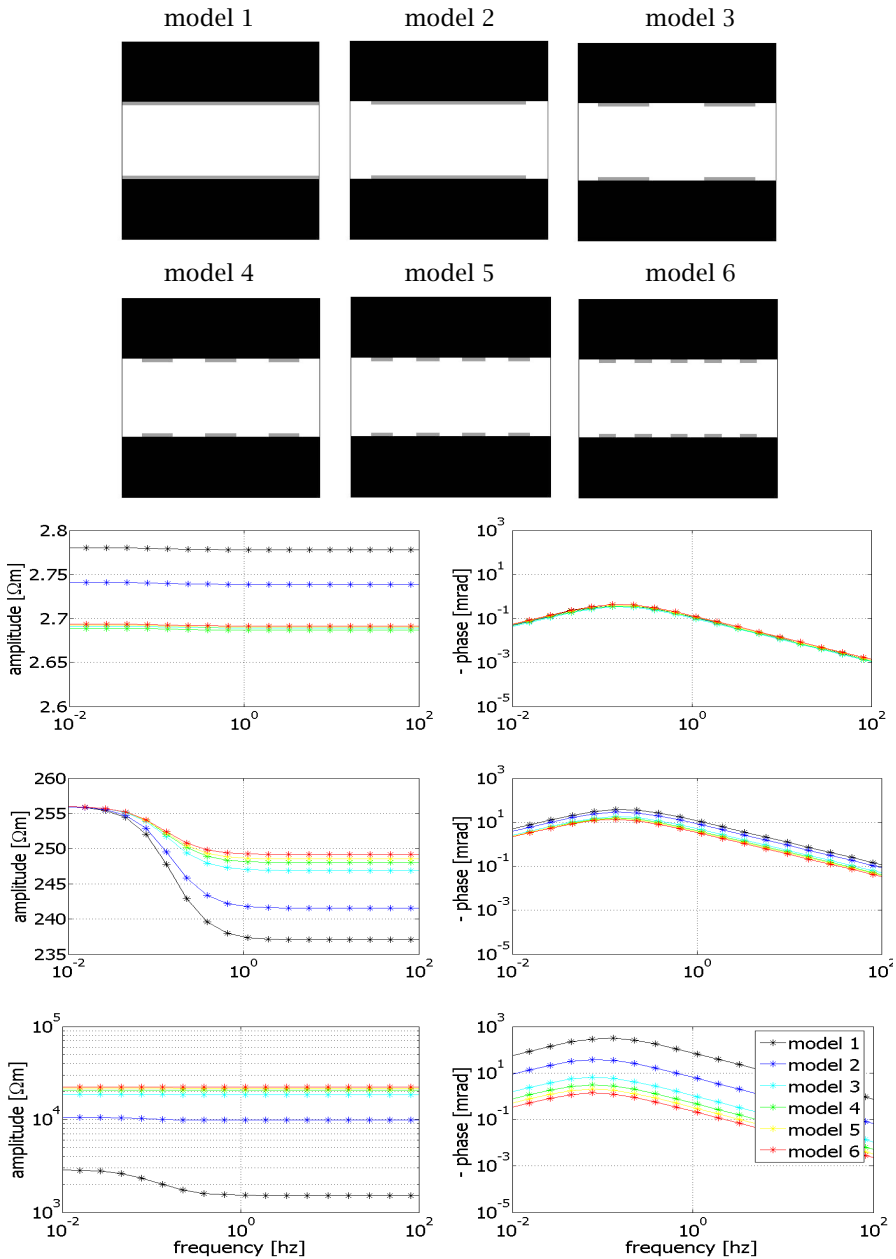


Figure 6.3: Series of different interface shapes. Models are shown in the top fraction (1 through 6 from upper left to lower right corner) and IP spectra below. The upper two CR diagrams are the results for a fluid conductivity of $\sigma_w = 1$ S/m, in the middle $\sigma_w = 0.01$ S/m and on the bottom $\sigma_w = 0.0001$ S/m. The interface conductivity is constant for all models with $\sigma_{R1} = 0.01$ S/m, $C1 = 0.01$ F, $\sigma_{R2} = 0.01$ S/m.

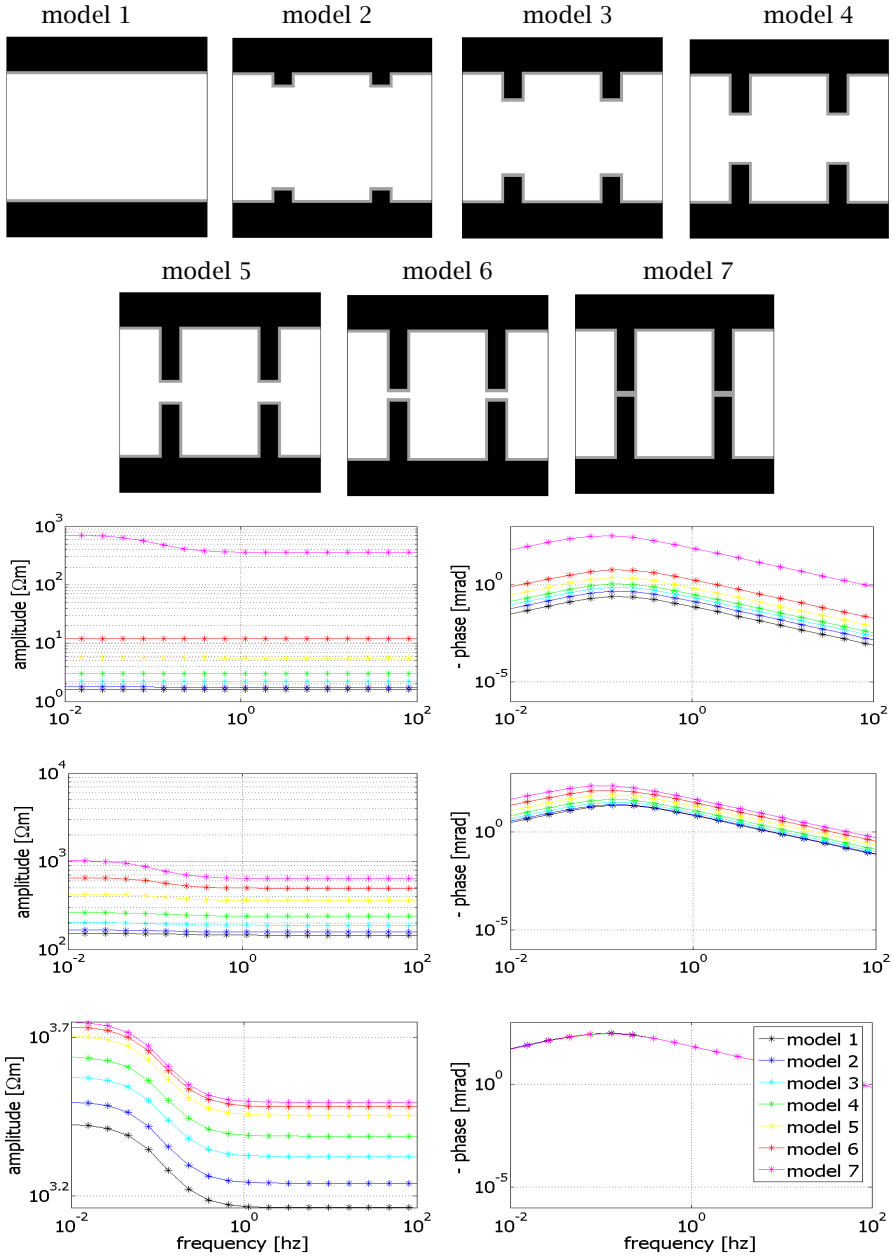


Figure 6.4: Model set 1: series of different pore throat shapes. Models are shown in the top fraction and CR spectra below. The upper two CR diagrams are the results for a fluid conductivity of $\sigma_w = 1$ S/m, in the middle $\sigma_w = 0.01$ S/m and on the bottom $\sigma_w = 0.0001$ S/m. The interface conductivity is constant for all models with $\sigma_{R1} = 0.01$ S/m, $C1 = 0.01$ F, $\sigma_{R2} = 0.01$ S/m.

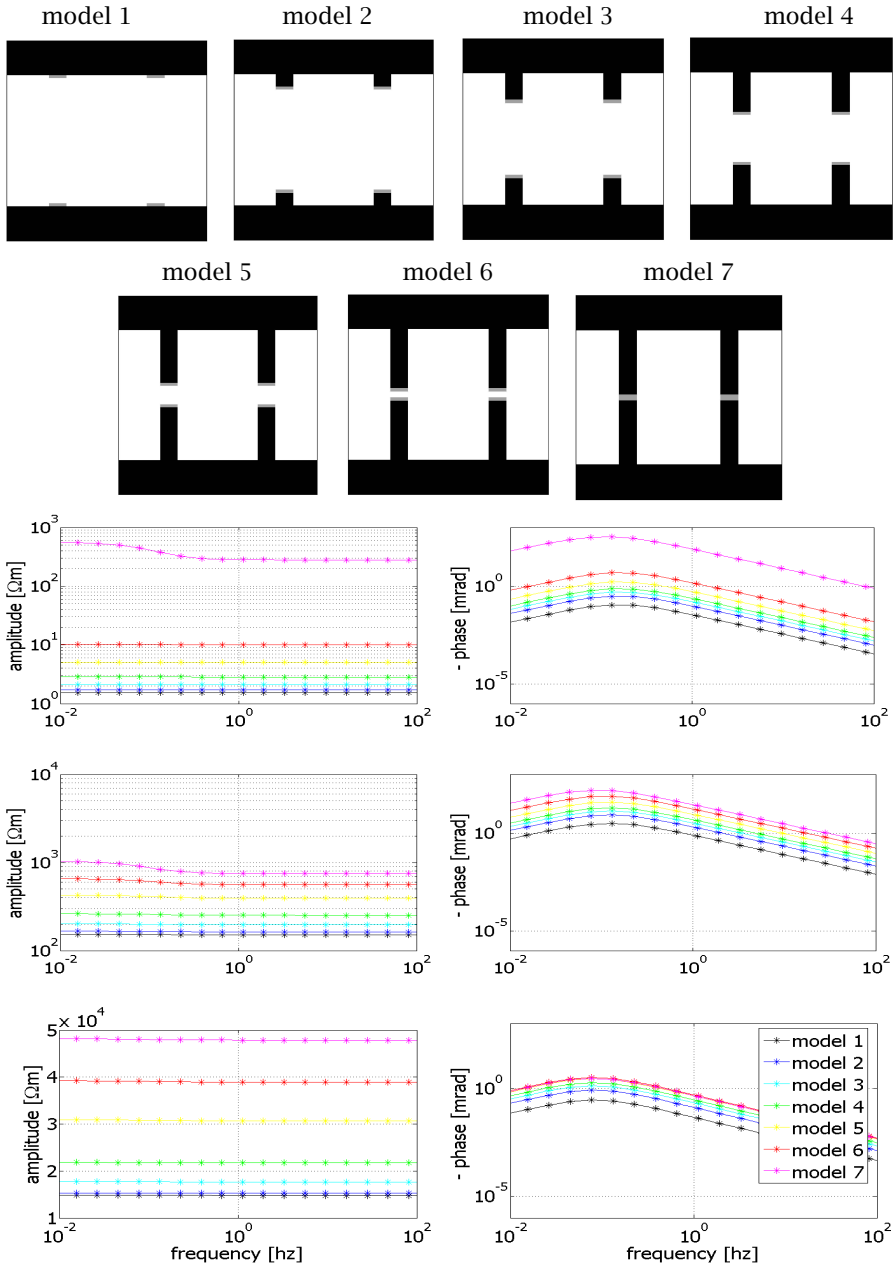


Figure 6.5: Model set 2: series of different pore throat shapes. Models are shown in the top fraction and IP spectra below. The upper two CR diagrams are the results for a fluid conductivity of $\sigma_w = 1$ S/m, in the middle $\sigma_w = 0.01$ S/m and on the bottom $\sigma_w = 0.0001$ S/m. The interface conductivity is constant for all models with $\sigma_{R1} = 0.01$ S/m, $C1 = 0.01$ F, $\sigma_{R2} = 0.01$ S/m.

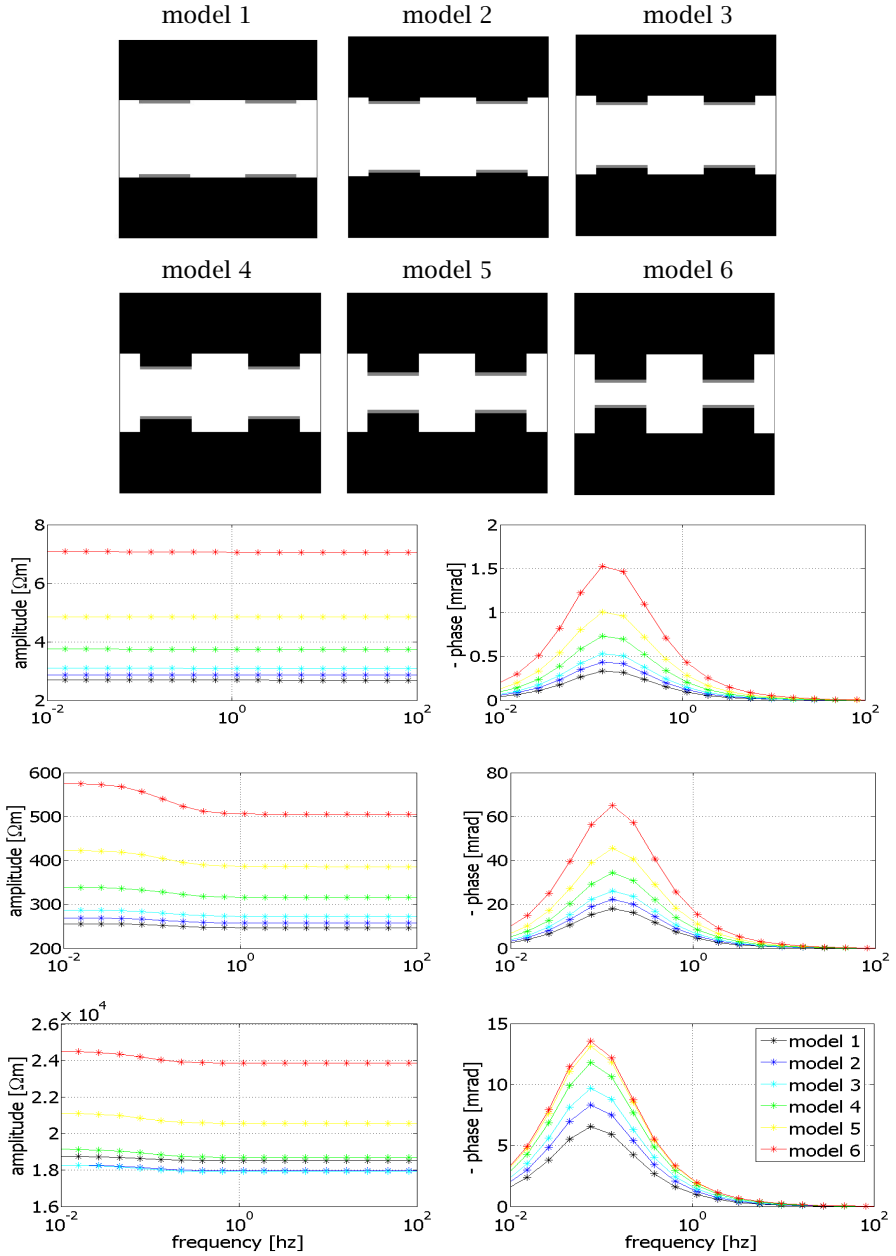


Figure 6.6: Model set 3: series of different pore throat shapes. Models are shown in the top fraction and IP spectra below. The upper two CR diagrams are the results for a fluid conductivity of $\sigma_w = 1$ S/m, in the middle $\sigma_w = 0.01$ S/m and on the bottom $\sigma_w = 0.0001$ S/m. The interface conductivity is constant for all models with $\sigma_{R1} = 0.01$ S/m, $C1 = 0.01$ F, $\sigma_{R2} = 0.01$ S/m.

6.2.3 Interface thickness

For two types of models the effect of a decreasing interface thickness was studied. This is of particular interest, since it describes phenomenologically what happens if the salt content in a fluid increases. Therefore, results should be compared to what has been observed in the salt study in chapter 3.

Model set 1 - continuous interface The first set of models is shown in Fig. 6.7 (top). The interface decreases from 7 pixel thickness down to 1 pixel. Again the interface conductivities remained constant ($\sigma_{R1} = 0.01$ mS/m, $C1 = 0.01$ F, $\sigma_{R2} = 0.01$ mS/m) throughout the simulation and calculations for three fluid conductivities have been made.

Independent of the fluid conductivity the general trend to be observed is a decrease of the phase peak as the interface thickness decreases. It does not change visibly in position, though.

Model set 2 - discontinuous interface If the interface is only present in the pore throats (model set in Fig. 6.8) and becomes gradually thinner, interestingly, the maximum phases are observed at some intermediate fluid conductivity. Moreover, and contrary to what was observed for the continuous interface, for intermediate fluid conductivities the maximum phase starts to shift somewhat in frequency (Fig. 6.9) upwards. For very low fluid conductivities (compared to the interface), the maximum even increases with decreasing interface thickness.

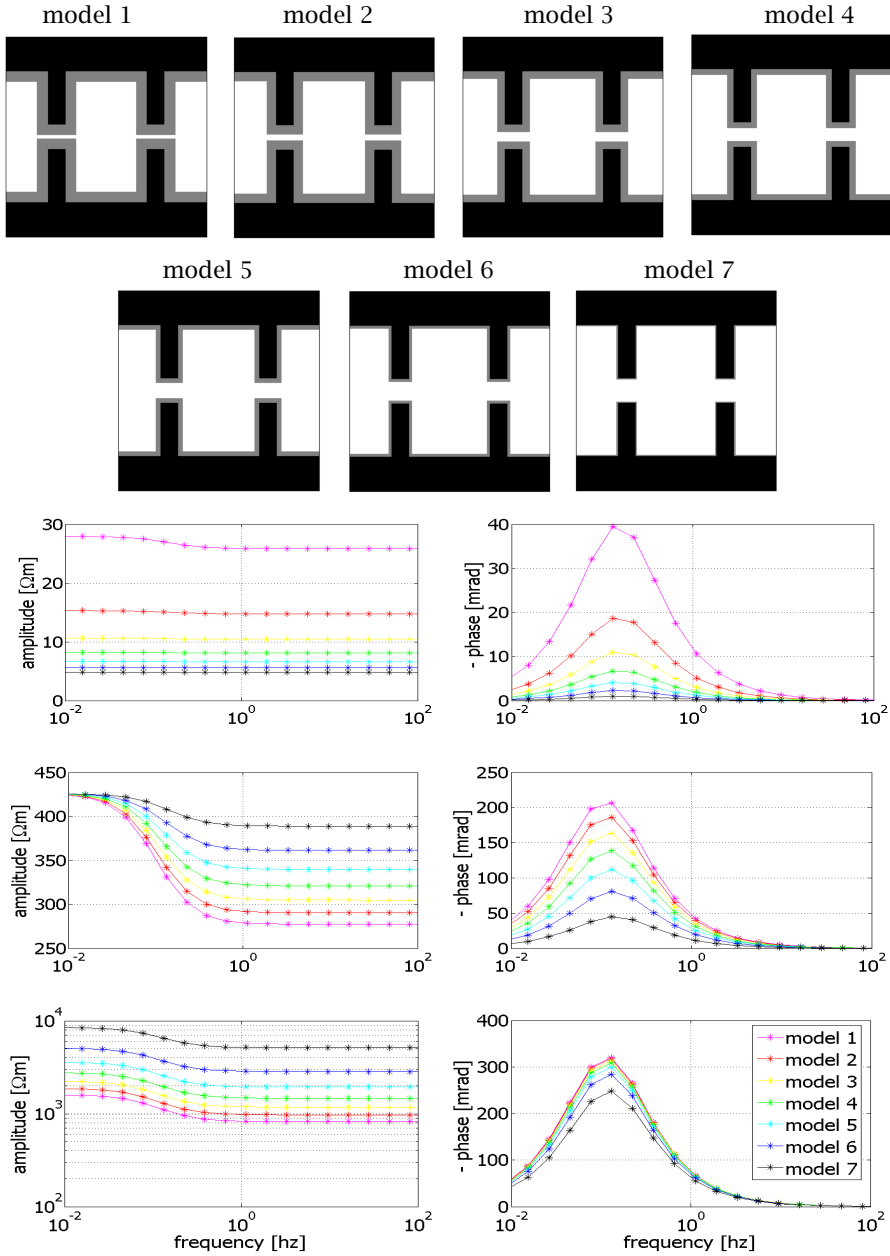


Figure 6.7: Model set 1: series of changing interface thicknesses. Models are shown in the top fraction (1 through 7 from upper left to lower right corner) and IP spectra below. The upper two CR diagrams are the results for a fluid conductivity of $\sigma_w = 1$ S/m, in the middle $\sigma_w = 0.01$ S/m and on the bottom $\sigma_w = 0.0001$ S/m. The interface conductivity is constant for all models with $\sigma_{R1} = 0.01$ S/m, $C1 = 0.01$ F, $\sigma_{R2} = 0.01$ S/m.

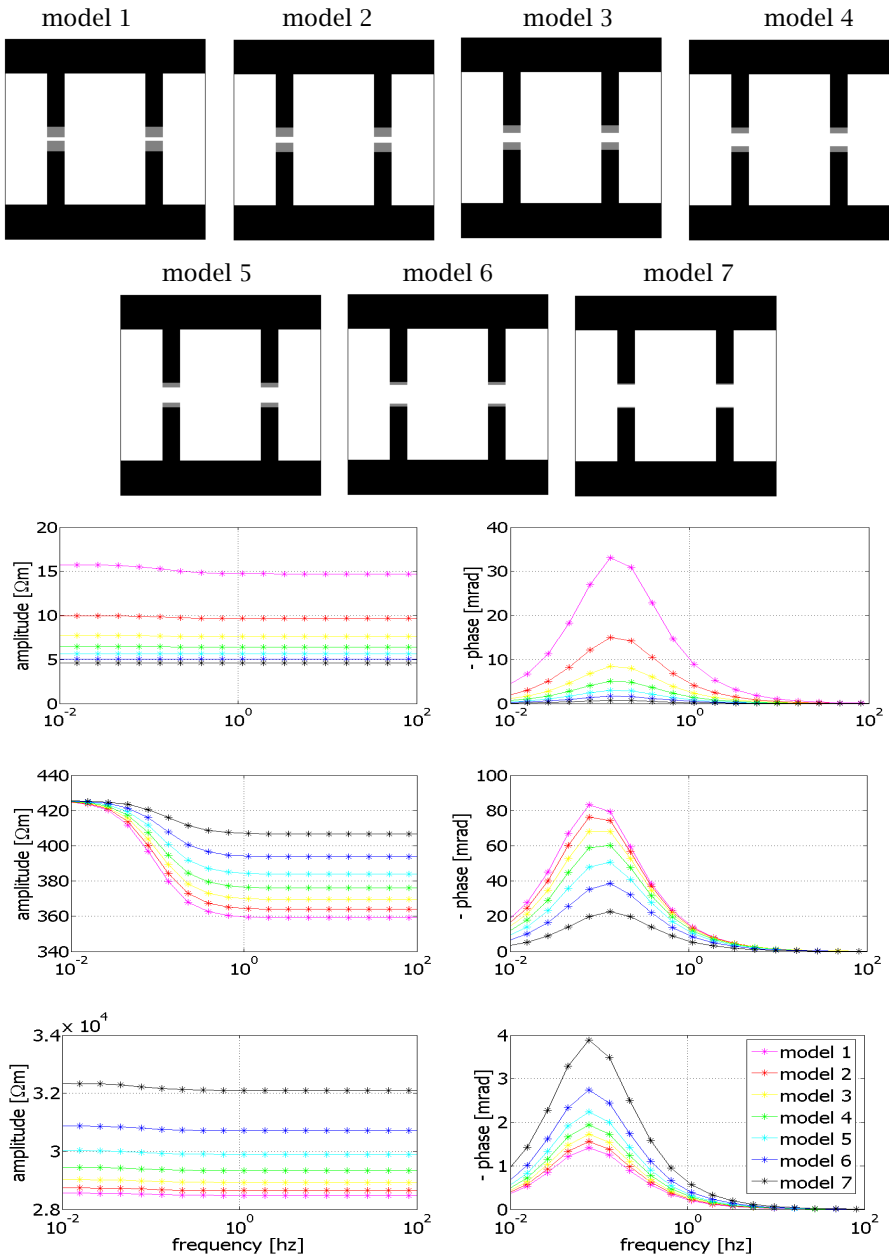


Figure 6.8: Model set 2: series of changing interface thicknesses. Models are shown in the top fraction (1 through 7 from upper left to lower right corner) and IP spectra below. The upper two CR diagrams are the results for a fluid conductivity of $\sigma_w = 1$ S/m, in the middle $\sigma_w = 0.01$ S/m and on the bottom $\sigma_w = 0.0001$ S/m. The interface conductivity is constant for all models with $\sigma_{R1} = 0.01$ S/m, $C1 = 0.01$ F, $\sigma_{R2} = 0.01$ S/m.

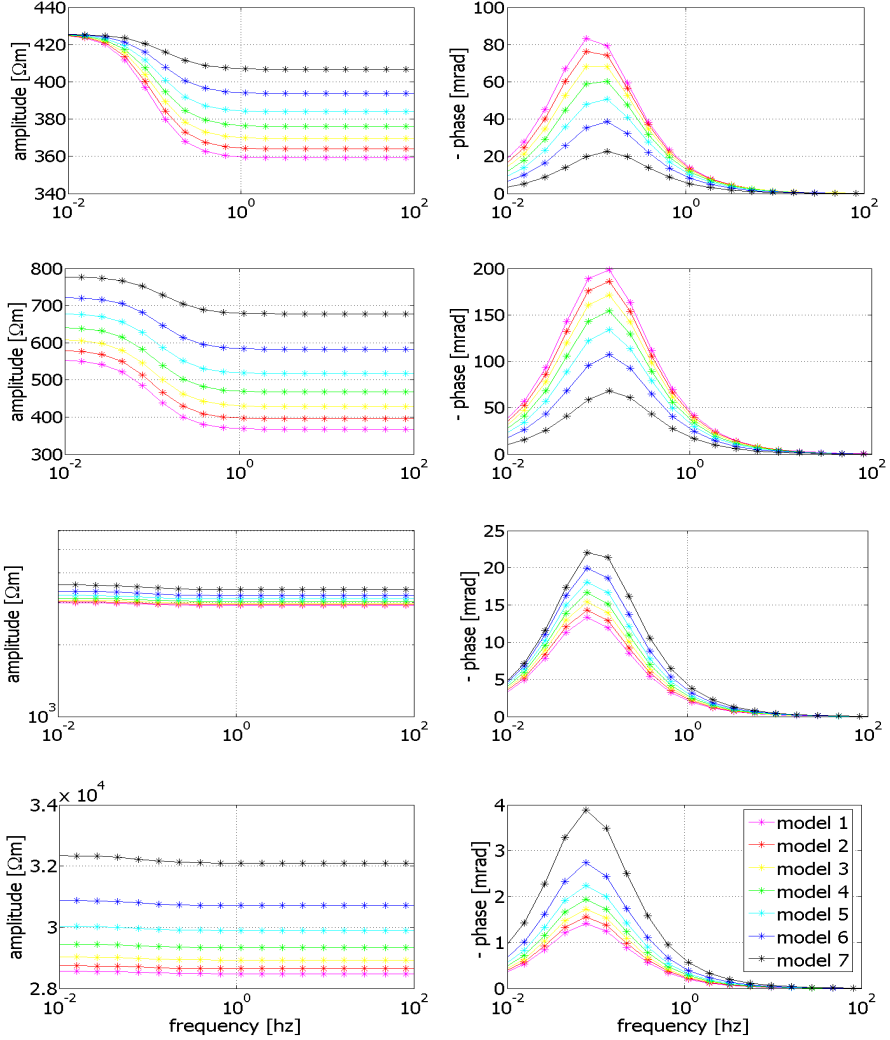


Figure 6.9: CR responses for the models shown in Fig. 6.8 for intermediate fluid conductivities. Top down σ_w changes from 0.01, 0.005, 0.001 to 0.0001 S/m. The interface conductivity is constant for all models with $\sigma_{R1} = 0.01$ S/m, $C1 = 0.01$ F, $\sigma_{R2} = 0.01$ S/m.

6.2.4 Changing conductivity

To understand the effects an increasing salt concentration in the fluid has, four models having different interface shapes were generated and their fluid conductivities changed, while the interface conductivity was kept constant. Hence, it is assumed that an increasing salt concentration will mainly change the fluid properties and probably only as a second order effect the electrical parameters (mobility, ion concentration) of the interface. The four models are shown in Fig. 6.10 on top, the according the phase spectra for different fluid conductivities below. Generally for increasing fluid conductivity the peak phase moves slightly to higher frequency. Depending on the model, the absolute phase maximum does not necessarily coincide with the lowest fluid conductivity. For example, the third and fourth model of the series generate highest phases at intermediate fluid conductivities ($\sigma_w = 0.0001$ and 0.001 S/m for models 3 and 4, respectively).

In the experimental salt study it was observed for most materials, that the phase peak shifted slightly towards higher frequencies as the salt concentration increases. The model results presented above add weight to the assumption that changing the relationship of fluid to interface conductivity might be at least one part of the overall explanation.

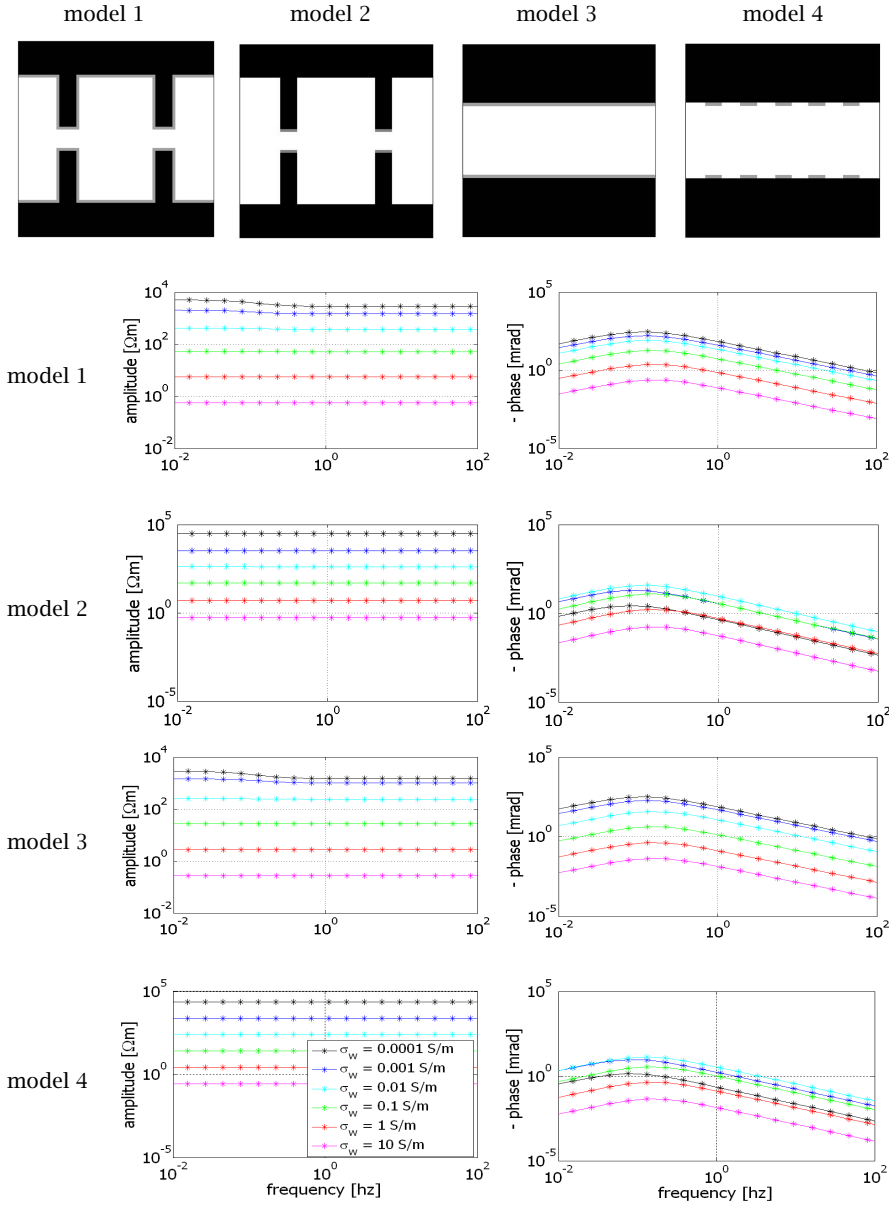


Figure 6.10: Set of four models to study the effect of an increasing fluid conductivity σ_w . Models are shown in the top fraction and CR spectra below. The interface conductivity is constant for all models being $\sigma_{R1} = 0.01$ S/m, $C1 = 0.01$ F, $\sigma_{R2} = 0.01$ S/m.

6.2.5 Changing saturation

The effect of evaporative drying is mimiced by adding a forth phase to the models, which represents air and has, like the matrix, a zero conductivity. This has been simulated for two model sets, one having a continuous and one having a discontinuous interface. Since the conducting volume decreases with reduced saturation, the fluid conductivity must increase. Saturation degrees and the corresponding changes in fictional "fluid concentration" were calculated for each model in the series. In other words, the last model in the series (compare Fig. 6.11) has a saturation degree of 0.17, which means the "concentration" increases by a factor of 5.84. In terms of conductivity, however, this factor is not as high. From the practical part of this study it was found that (slightly dependent on the salt) this corresponds approximately a factor of 3 (compare for example Fig. 3.15). How the saturation degrees, fictional "concentration" and corresponding fluid conductivity change for the models used here is listed in table 6.1. However, it is not obvious, how the interface conductivity changes for reducing water contents. Its ion content either also increases together with the fluid concentration or it may stay constant and take up surplus ions only later on. Both cases were simulated for the two model sets below.

Table 6.1: Desaturation properties of the models in Fig. 6.11 and 6.12.

	saturation	"concentration"	σ_w
model 1	1.00	1.00	0.010
model 2	0.98	1.01	0.010
model 3	0.93	1.01	0.011
model 4	0.81	1.24	0.011
model 5	0.65	1.54	0.012
model 6	0.29	3.43	0.020
model 7	0.17	5.84	0.030

Model set 1 - continuous interface The models used here are shown in Fig. 6.11 (top). Air pixels have a dark grey color and are not conducting. The results are modelled for a fluid conductivity σ_w of 0.01 S/m. The upper row of CR spectra in the same figure illustrates the responses in case of a constant interface conductivity consisting of $\sigma_{R1} = \sigma_{R2} = 0.01$ S/m and $C1 = 0.01$ F. For this case the phase peak increases with reducing water content, but does not shift in frequency. A similar observation is made, if the interface conductivity components σ_{R1} and σ_{R2} are changed and for each desaturation step take the same value like the fluid conductivity σ_w . This would correspond to an ion uptake of the electrical double layer, where the ions as much that they would undergo a mobility drop. As the lower CR spectra in Fig. 6.11 illustrates, however, the maximum phase travels towards higher frequencies as the water content is reduced.

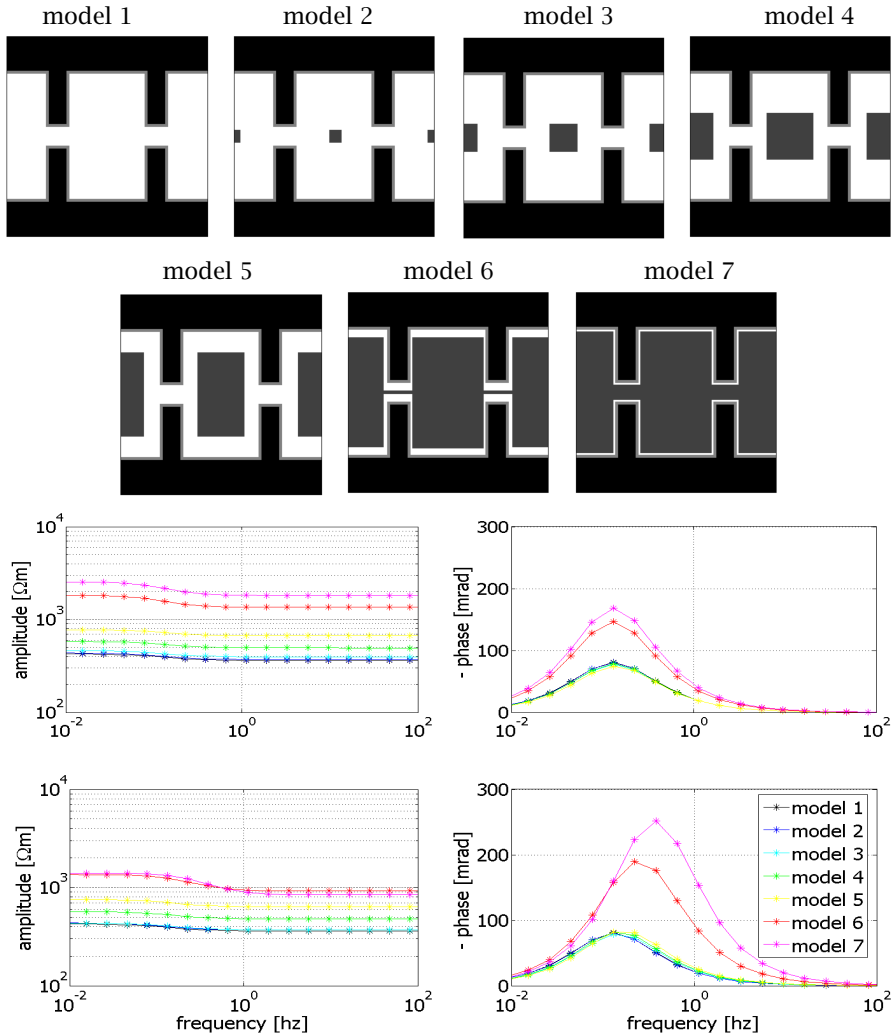


Figure 6.11: Model set 1: series of models varying in saturation, the interface is continuous. A fourth phase (dark grey) is introduced symbolizing air and having a conductivity of $\sigma_{air} = 0$ S/m like the matrix. Models are shown in the top fraction, CR spectra below. The upper CR diagram is for a constant interface conductivity, the lower for a interface conductivity increasing together with fluid conductivity σ_w .

Model set 2 - discontinuous interface The second model set is given in Fig. 6.12. The saturation levels are exactly the same as for the previous models and the conductivities are again changed in the same way. It must be noted, that the interface shape is important and crucial for the phase and imaginary conductivity behavior; here, the maximum phase decreases with saturation. As seen earlier, the position of the peak is stable if the interface conductivity is constant. When it increases with reducing water content it shifts as in case of the first model towards a higher frequency.

For both models and the two cases the normalized saturation exponents for the real and imaginary conductivity components were calculated for comparison with the experimental results in chapter 4.2.3. Figure 6.13 shows the saturation exponents of the model results. For the model with continuous interface the real conductivity components decline in any case faster than the imaginary ones no matter what the interface conductivities are. This corresponds to observations made by Ulrich and Slater (2004) on unconsolidated sands with negligible clay contents. For the second model set with a discontinuous interface the opposite behavior is seen: the real (Archie) term decreases more slowly than the interface term. This case matches with the evaporative drying results of the majority of the materials investigated in this study.

From thin section analysis and Xray diffractometry results the Cottaer and Bentheimer sandstones have relatively high clay contents. In fact, this actually implies that in these materials surface conduction occurs along a continuous layer of pore lining clay minerals. Furthermore, this at least initially happens relatively independent of water saturation, since clays have an irreversible water content, which cannot be removed by evaporative drying. However, if the modelling results presented above can be understood to represent some effective electrical behavior, this suggests that somehow the surface conduction paths do become discontinuous for a reduced water saturation. It seems conceivable to assume that especially for those materials with a high clay content already a very small change in saturation would intermediately affect (decrease) surface conductivity.

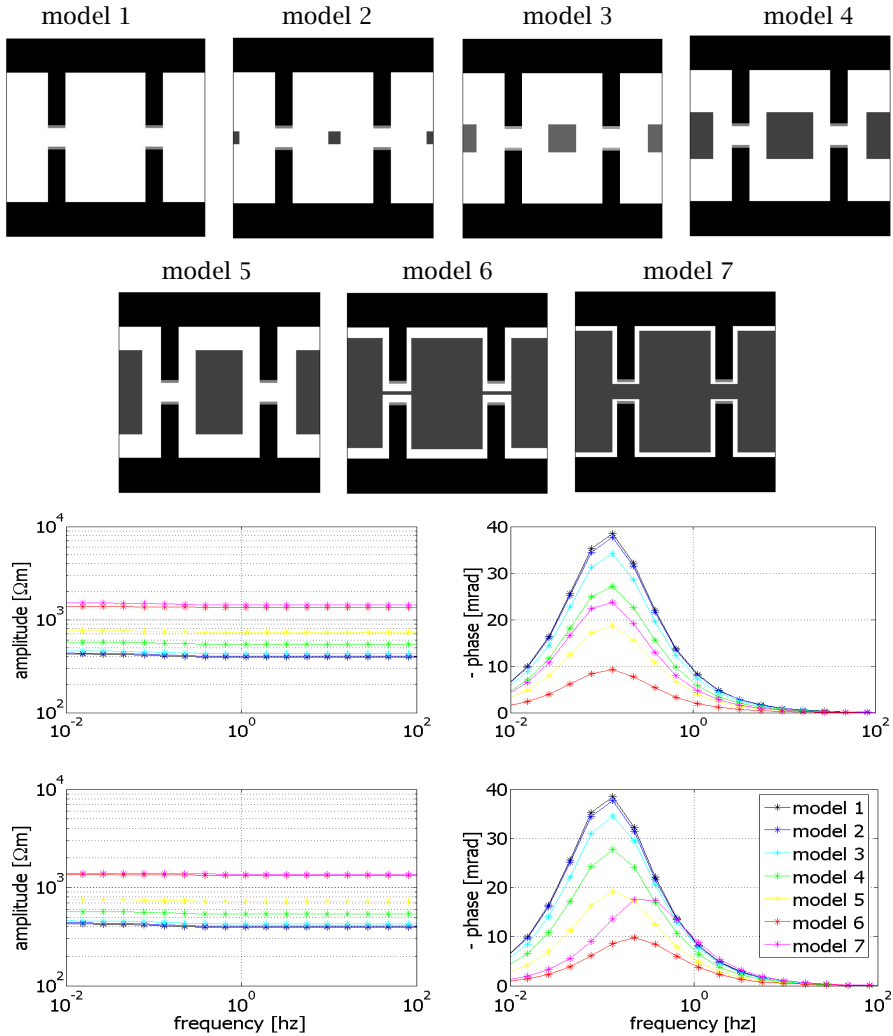


Figure 6.12: Model set 2: series of models varying in saturation, interface only existent in pore throats. A fourth phase (dark grey) is introduced symbolizing air and having a conductivity of $\sigma_{air} = 0$ S/m like the matrix. Models are shown in the top fraction, CR spectra below. The upper CR diagram is for a constant interface conductivity, the lower for a interface conductivity increasing together with fluid conductivity σ_w .

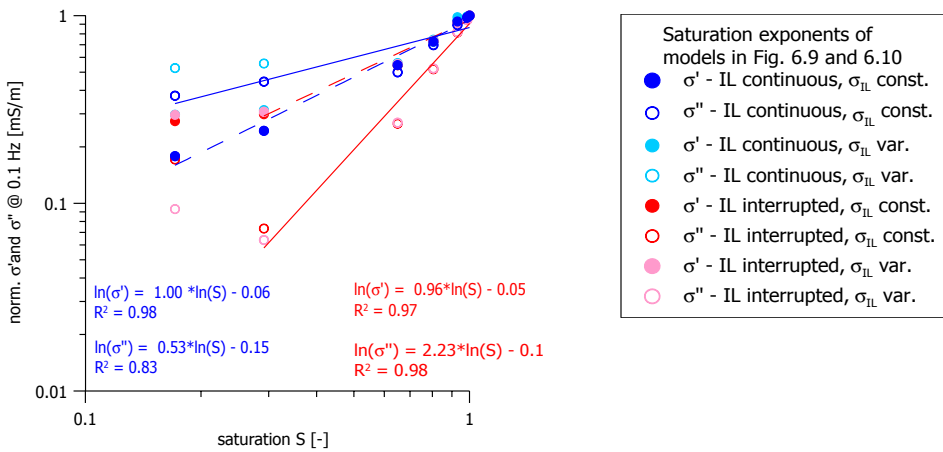


Figure 6.13: Normalized saturation exponents for the models in Fig. 6.11 and 6.12.

6.2.6 Archie relationships

In this section, studies on the relationship of porosity, tortuosity and the formation factor will be made to prove whether this model is also qualified for general studies on the empirical Archie law. If surface conductivity is negligible and the electrical conduction takes place in between parallel pore walls with no constrictions (tortuosity $T = 1$, compare eq. 2.44) the bulk conductivity is barely a function of porosity. For the models shown in Fig. 6.14 on top the tortuosity equals 1 and the porosity changes from 0.08 in model 1 to 0.86 in model 6. The power-law dependence between formation factor and porosity for these models is illustrated in Fig. 6.15 evidencing, that the slope between the two parameters is about 1 like expected for a straight pore.

The formation factor was also determined for two other models previously used in the study of a developing pore throat depicted in Fig. 6.4 and 6.6. For these models the tortuosity is not equal to 1, but varies with porosity. The CR responses of these two models were re-calculated neglecting the interface ($\sigma_{R1} = \sigma_w$, $\sigma_{R2} = C1 = 0$). However, as it appears from Fig. 6.15 these results do not differ much from those with intermediate surface conductivity ($\sigma_{R1} = \sigma_{R2} = 0.01$ S/m, $C1 = 0.01$ F, compare open and filled symbols in this figure). Due to the changing tortuosity in these two models does not result a log-log linear correlation of F and Φ .



Figure 6.14: Model set with varying porosities Φ . From model 1 (top left) to model 6 (bottom right) Φ takes the values 0.08, 0.23, 0.39, 0.55, 0.70, 0.85.

The tortuosity T after Winsauer and Shearin (1952) is defined as $F \cdot \Phi$. In the case of the 2D models this value should match the ratio of average geometrical radius r_g and average electrical radius r_{el} . The average electrical radius equals $r_{el} = 0.5 \cdot L/F$ for the

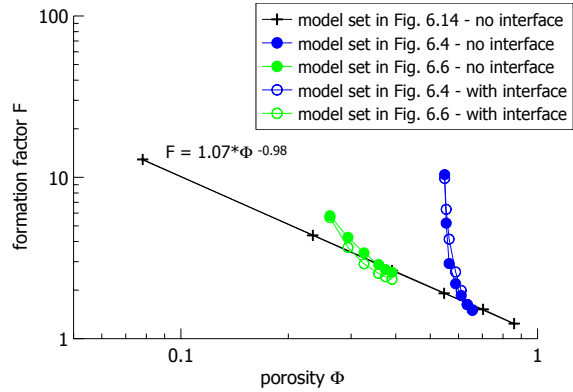


Figure 6.15: Formation factor F versus porosity Φ for the model sets shown in Fig. 6.4, 6.6 and 6.14. Fluid conductivity $\sigma_w = 0.01$ S/m

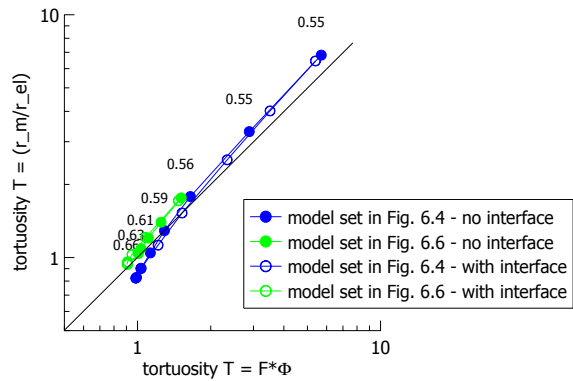


Figure 6.16: Tortuosity calculated from the formation factor F versus tortuosity calculated from geometrical and electrical characteristic length scales for the model sets shown in Fig. 6.4 and 6.6. Black labels denote porosities.

cubic models used here with L being the length of the pore. The average geometrical radius is defined as $r_g = (L1*r1 + L2*r2)/L$ with $L1$ and $r1$ being the length and radius of the throat and $L2$ and $r2$ the length and radius of the pore belly, respectively. Figure 6.16 proves, that the tortuosities calculated the two ways match well.

6.3 Summary

A new procedure for an image based effective electrical impedance modelling was presented. The images consist of user defined distributed conducting and non-conducting phases. The conductivity tensors of each phase can have different terms along the diagonal for the x- and y-directions and each being either real or imaginary in value. This approach allows one to estimate how particular length scales and conductivities alter CR responses. The author considers this important as until now it lacks a way to unlink structural from chemical effects observed in CR measurements. The FD program AC2D (Garboczi, 1998) had to be adapted to be used for a microstructural parameter study on simple test microstructures.

In addition to some general studies, the focus in this chapter was to understand how the addition of salt to a pore fluid would change CR patterns. The driving force to do this was the question which phenomena observed in the experimental salt study in chapter 3 must (can) be associated with changing structural features and which not. The two main properties influenced by the addition of salt are the fluid conductivity and the thickness of the double layer (here referred to as interface). To increase the explanatory power of this study different "conductivity environments" possible in a pore for two basic microstructures having either continuous or a discontinuous interfaces were examined. The results showed that both a decreasing interface thickness and a more conductive fluid tend to result in a maximum peak shifting to higher frequencies. Depending on the conductivities of fluid and interface, the maximum can increase or decrease while moving. It has also been shown that for those microstructures with discontinuous interface an increase of the fluid conductivity causes the phase to reach a (global) maximum at some intermediate value of σ_w . These model results match well with the findings obtained in the laboratory; for most materials a decrease of the C-C relaxation time τ was found, which corresponds to an increase of the relaxation frequency. Similarly, for the majority of the samples the maximum phase was highest at intermediate fluid salinities. Basically, the only material behaving differently was the clayey Cottaer sandstone, for which τ increased with fluid conductivity. This indicates that possibly other, most likely chemical factors (ion exchanges, mobility changes) must be recognized in this case.

Another concern in this chapter was to develop a better understanding of how CR responses depend on saturation. It was shown that the results are essentially different in case of either a continuous or a discontinuous interface in the microstructure. For the former, the interface conductivity quickly dominates electrolytical conductivity yielding increasing and towards higher frequency moving phases. Vice versa, for the latter, the interface conductivity reduces more rapidly, the phase peaks diminish and move again towards higher frequency. If these model sets are not oversimplified but do actually represent an effective medium behavior, it must follow that primarily those materials with a high clay content, do act like they would have an interrupted electrical double layer. Others, like bricks and limestone, behave like they have a continuous electrical double layer, even though their clay content is practically zero.

In the last section of this chapter the results of models with changing porosity and tortuosity were compared in order to prove, whether the existing general relations between these parameters can also be retrieved here. The expected relationships could be reproduced substantiating the practical use of this approach.

7 Conclusions

Salt weathering is a potent cause of rock decay. Conservators and building engineers concerned with restorative problems demand new technologies and non-destructive testing tools to thoroughly understand ongoing decay and predict service life or renovation costs.

Complex electric measurements of brine-saturated material are a function of both the microgeometry and the surface chemistry of the sample. Hence, they may be used to remotely determine the textural and solution chemistry properties. Moreover, electrochemical polarizations in ion conductive material is sensitive to small pores at high frequencies and to large pores at low frequencies, therefore, by measuring the complex resistivity response of rock over a wide frequency range, information about the material microgeometry may be obtained.

This thesis is concerned with the complex resistivity behavior of building materials under the influence of changing salinization and saturation regimes. The experimental side of the study consists of complex resistivity and electroacoustic measurements, which allow both to describe phenomenologic changes of the electrical properties and to simultaneously characterize the chemistry of the electrical double layer. Complementary, a new image based FD modelling procedure calculating effective impedance responses has been used for a thorough parameter study on test microstructures in order to differentiate between structural and more chemical influences. Gaining a better understanding of which trends in CR response altering must be associated with structural changes helps to single out "unexpected" (experimental) phenomena which consequently occur rather due to chemical changes.

Probably of great significance is the dependence of maximum (peak or flat) phase and the dominant pore throat size. It could be shown that for the entirety of the spectra measured here (and previously by other authors) there is a power-law dependence of Cole-Cole relaxation time τ and some characteristic length scale (in consolidated materials mostly the dominant pore throat diameter $> 10 \mu\text{m}$). This dependency has been expressed by other authors earlier, but the data basis was weak. The author suggests using complex resistivity as a non-destructive testing tool merely for materials having pore sizes between 10 and 100 μm . As soon as pore throat sizes fall below 10 μm , phase angles get smaller than -5 to -1 mrad what makes them challenging to measure. Concretes and mortar have pore throats of less than 1 μm , thus, they generate phases of only

-1 mrad and, consequently these materials must be classified inapt for reliable complex resistivity assessments.

The results of the salt study show how responsive polarization (imaginary conductivity) is to changing the salinization regime. With increasing salt concentration of the saturation fluid for most materials the imaginary conductivity increases until the fluid conductivity reaches about 1 S/m. Afterwards it is either constant or slightly reduces. The sensitivity of impedance measurements to the anion type is considerably less compared to the dominant cation type of the pore solution. Often (mainly for sandstones) salts with divalent cations generated much lower polarization magnitudes compared to the same salts with a monovalent cation. For the former the electrical double layer thickness is thinner and the bondage of their cations stronger to a negatively charged matrix.

The Cole-Cole relaxation time τ is mostly observed to decrease with increasing fluid salinity σ_w . The power-law exponent of the log-log relationship between σ_w and τ was usually between -0.35 and -0.55 and did not depend on the salt type. Only in case of a very clay-rich sandstone (Cottaer) τ increased with fluid salinity, however, despite from being positive the exponent was with 0.38 about in the same range. It is conceivable to assume either ion exchange processes, ion mobility changes or effects related to the high surface roughness causing this.

It is known that complex resistivity also depends on saturation, even though most of the very few as yet published experimental results were obtained on unconsolidated earth materials. Hence, understanding the implications of salinization on complex resistivity is not enough, when they are unlikely to hold in the instance of variable saturation. But, even in the laboratory, electrical measurements on partially saturated samples are still associated with high electromagnetic noise and coupling difficulties due to their generally dry surfaces. Even under relatively easy, noise-free conditions, most measurements are poor in quality and difficult to repeat. Problems can arise from the fact, that dry samples soak moisture from the coupling medium and their water content may change during the experiment. The four-point measurement cell developed at BAM provided with potential wires sitting in contact chambers outside the current paths and filled with agar gel, however, was found to enable repeatable and reliable measurements. The effect of water saturation was studied for six materials in combination with up to five fluids. Fluid chemistry does not influence general trends as it is generally observed for a material. Only for the distilled water pore fluid cases the saturation exponents may vary from those determined for more saline fluids. In most cases the imaginary conductivity decreases more rapidly than the real (or bulk) conductivity. This observation is opposite to what other authors reported for measurements on unconsolidated sediments (being probably comparable to the sandstones in mineralogy). Most critical for how saturation exponents change is very likely the pore system and its geometry. The brick and limestone samples have similar desaturation patterns like reported for unconsolidated sediments. The

sandstones and the very porous aerated concrete behaved differently, which, in fact, are the samples with the highest clay content.

To improve the practical value and predictive use of complex resistivity measurements the theoretical understanding of the electrical double layer and its particular changes with fluid chemistry seems essential. Zeta-potentials and how they vary with salt concentration and type have been studied for five materials in electroacoustic measurements to characterize the diffuse part of the electrical double layer and estimate its relation to polarization. Mono- and divalent salts show generally major differences for all materials. Whereas for monovalent ions zeta-potentials first increase with salinity and later on decrease, even small amounts of divalent salts cause the zeta-potential to diminish instantly. Comparing how zeta-potentials and imaginary conductivity vary with salinity shows a noticeable universal correlation although this is weaker than expected. Results may indicate, that a better and more direct measure of polarization could be the fixed layer charge density, which can be referred from zeta-potential values if the total surface charge is known. One way to quantify this would be to use the measured diffuse-layer charge density in a polarization model like Fixman's and to compute the expected response from the diffuse layer polarizations. If then the simulated dielectric response is significantly smaller than the measured response, this would support the assumption that fixed-layer polarization do actually control polarization.

A new approach in the microstructural modelling of geometrical features has been presented. The conductivity model used assumes the interface matrix/fluid (electrical double layer) to consist of a parallel connection of a resistor and a resistor and a capacitor in parallel. This model equals the traditional Debye type to explain relaxation phenomena. The single resistor in the interface phenomenologically demonstrates the surface conductivity at zero frequency. The series of a resistor and a capacitor mimics the dispersion phenomena observed at higher frequencies. Using the new approach indicates that changing double layer thickness may not have as much an effect as changing fluid conductivity to shift the polarization peak in the frequency range. The former, however, is still found to decrease polarization as it thins out. Interestingly, it could also be shown, that depending on the microstructure it may cause the maximum phase to occur at some intermediate thickness. This phenomenon was also observed in the experimental section in this thesis, but interpreted tentatively as a charge saturation versus decreasing ion mobility process; the new results imply to further include microstructural features in the argumentation. However, it is important to note that no claim is made that finality has already been reached on any particular aspect of this modelling procedure. For instance, the frequency exponent of the capacitor in the electrical circuit representing interface pixel was, throughout all calculations, equal to 1. It is, however, known that many rocks do have frequency exponents between 0.1 - 0.6, which for example appears in the Cole-Cole model. However, large quantitative discrepancies should be expected to result from complications which were not taken into account in the highly simplified

2D microstructures. For example, the used microstructures consist of 128x128 pixels resulting in improbable proportions of bulk pore, pore throat and interface sizes. Using a model which resembles possibly true proportions (e.g. bulk pore 100 μm , pore throat 20 μm , electrical double layer 0.3 $\text{\AA} = 3 \times 10^{-4} \mu\text{m}$) would need to consist of about 400 000 x 400 000 pixels to make the interface at least one pixel thick. This exceeds the normal computing power of available PCs by far. Still, the qualitative implications of the image based impedance modelling are rather far reaching.

In conclusion, complex resistivity is a promising method to improve our understanding of electrical charge storage and electrolytical ion transport in conductive wet porous media. Having calibration data available complex resistivity measurements should improve and facilitate physical and chemical assessments of rock decay. The additional information that is contained in the polarization response is a useful indication of the chemistry of the saturating fluid. Complex resistivity provides a reliable means to at least qualitatively map the spatial distribution of water and salt for example between boreholes. Nevertheless, further laboratory studies are needed before the method can be sufficiently well used in routine analyzes. The quantitative determination of salt contents remains extremely challenging. Usually the investigated effects are considerably small being of the order of a few milliradians, which very often is slightly greater than their standard deviation or even the measurement accuracy. When salts are present, the measured resistivity signals further reduce, which, in fact, is unfavorable for a quantitative testing method. It must also be understood, that applying complex resistivity in the field scale can be delicate due to high noise levels (electricity, tubing, electromagnetic noise) or deficient electrode coupling. Own experience showed that the field deployment of these techniques is often limited to frequencies below 10 Hz. The advantage of complex resistivity over common other methods is to be able to measure along profiles or 2D grids and get a 3D picture of possible damages. Hence, they are a useful tool to support core sample analyzes, which provide precise information but low spatial resolution.

Appendices

A Mineralogy of the materials investigated

In order to characterize the materials under investigation and help interpret their CR behavior a variety of additional petrophysical analyzes have been made. In the subsequent sections the lithologies and detailed test results will be described.

Lithology

Cottaer sandstone is a sedimentary rock from the creataceous age. It is mined in Großcotta (Saxony) in Germany, its basic color is light to yellow grey, often with striae of darkish yellow brown limonite precipitations. Carbon particles may cause distinct marbling. Cottaer sandstone is a uniformly, fine grained sediment, partially clayey, siliceous or limy cemented with grain sizes between 0.0063 - 0.63 mm, the dominant grain size being 0.02 - 0.063 mm. The poorly rounded grains are in contact mostly along binder phases. The mineral content comprises quartz, alkali, feldspar, kaolinite and the binding phases illit and kaolinite. It has a comparatively high clay content, and the clay minerals exist along pore linings as well as in in intergranular bands (compare thin section, the brownish band on the right in the left picture, Fig. A.3)

Bentheimer sandstone is a sedimentary rock from the lower cretaceous age mined in Bad Bentheim (Lower Saxony) in Germany. It is white to light brown in color. Grains are fine to medium (0.1 - 0.5 mm), fairly sorted with no layering, partially clayey and containing fine pores. Bentheimer sandstone contains well rounded quartz, feldspar and accessories (tumaline, zircon, rutile, muscovite, glauconite) only less than 1%. Binding phases are isolated kaolinite pore fillings, but mostly suturated grain contacts.

Baumberger sandstone is a light grey to yellowish and yellow-brown sandy calcareous marl, which is mined in Münsterlad/Baumberge (Westfalen) in Germany. It formed as a marine sediment in the upper cretaceous (Campan). Its color is homogeneous with darker layers, weathered surfaces are browner due to the limonite content. The matrix of Baumberger sandstone contains mostly carbonate, other components are fossils (50%), quartz and feldspar (40%), and in traces, glauconite and limonite. The grains are moderately to well sorted, sub-rounded to rounded and around 0.3 mm in size. The fossils are between 0.1 and 1.5 mm in size. The binding phase is largely micritic containing peloids (83%) and kaolinite and chalcedon in pore fillings (17%).

Savonniere limestone is a sedimentary rock of beige color composed largely of the mineral calcite (calcium carbonate: $CaCO_3$ or dolomite $CaMg(CO_3)_2$), often contain variable amounts of silica in the form of chert or flint, as well as varying amounts of clay, silt and sand as disseminations, nodules, or layers within the rock. The primary source

of the calcite in limestone is most commonly marine organisms. These organisms secrete shells that settle out of the water column and are deposited on ocean floors as pelagic ooze or alternatively is conglomerated in a coral reef (see lysocline for information on calcite dissolution).

Bricks Clay bricks are artificial stones made by forming clay into rectangular blocks which are hardened by burning in a kiln. Over the period of firing, brickclay becomes a metamorphic rock. Clay minerals break down, release chemically bound water and change into a mixture of two minerals, quartz and mullite. The quartz crystallizes very little in that time and remains in a glassy state. Thus, the key mineral in bricks is mullite, a blended compound of silica and alumina. Iron is a lesser ingredient that oxidizes into hematite and causes the red color of most bricks. The bricks in this study were fabricated by FALKENLOEWE (www.falkenloewe.dk)

Sand-limestones are artificial masonry bricks that are made on a very extensive scale in many countries. Dry sand is mixed in a proportion of about 12:1 with quicklime (CaO). The mixture is then slightly moistened with water and moulded into bricks under presses. The mixture is compacted and 4-8 hours hardened under vapor pressure. A typical sand lime stone contains: silica (SiO_2) 84%, lime (CaO) 7%, alumina and oxide of iron 2%, water, magnesia and alkalis together 7%. In Germany sand-limestones are classified after DIN V 106 according to molded density (1.0 - 2.2, most common are 1.4, 1.8, 2.0) and comprehensive strength classes (between 4-60, most common are 12 and 20). The DIN classification of the samples used in this study are listed in Table A.1.

Table A.1: DIN classification of the sand-limestones used in this study.

SHORT SYMBOL	DIN CLASSIFICATION
KS	DIN V 106 - KS 12 1,8 - NF PK
Ka	DIN V 106 - KS L 20 1.8 - 2DF
Kb	DIN V 106 - KS 20 2.0 - NF
Kc	DIN V 106 - KS 28 2.0 - NF
Kd	DIN V 106 - KS L 12 1.4-2 - DF
Ke	DIN V 106 - KS 12 1.8 - NF

Aearated concrete is a precast, manufactured building stone made of natural raw materials. Portland cement is mixed with lime, silica sand, or recycled fly ash, water, and aluminum powder or paste and poured into a mold. Steel bars or mesh can also be placed into the mold for reinforcing. The reaction between aluminum and concrete causes microscopic hydrogen bubbles to form, expanding the concrete to about five times its original volume. After evaporation of the hydrogen, the highly closed-cell, aerated concrete is cut to size and form and steam-cured in a pressurized chamber (an autoclave).

Mercury injection capillary pressure

The pore size distributions as determined in mercury injection experiments shows Fig. A.1. The top picture gives the results for the sandstones and the limestone, the center picture the bi-model distributions measured for the sand-limestones.

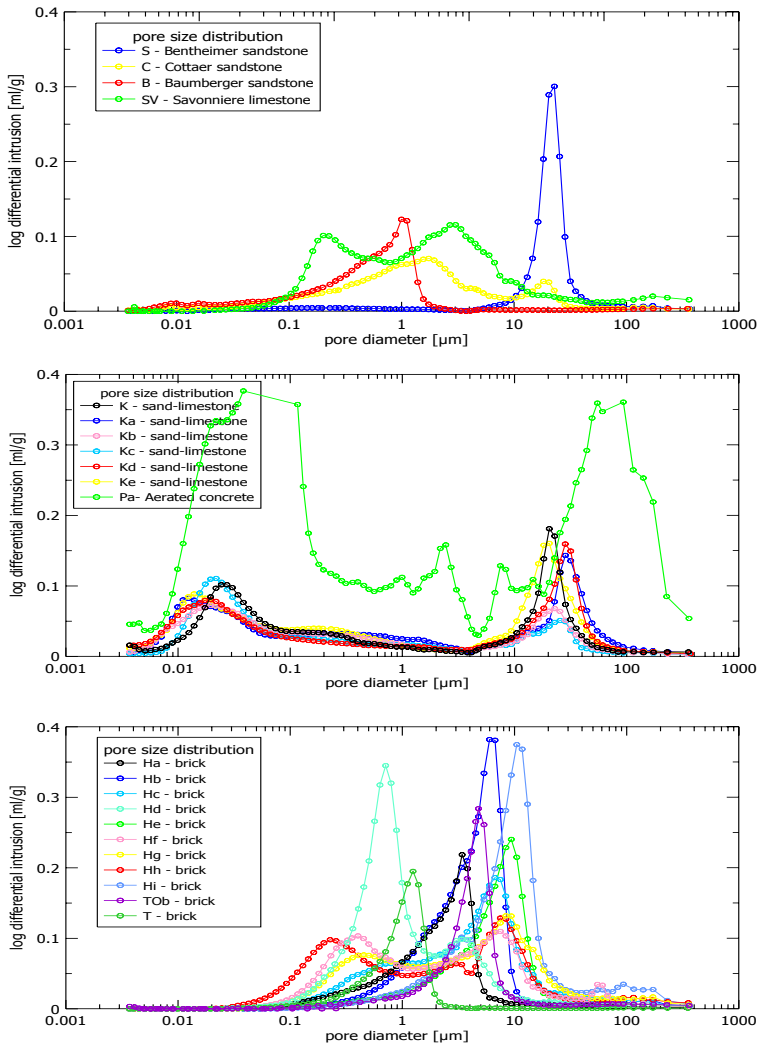


Figure A.1: Pore size distributions (PSD) of the materials under investigation determined in mercury intrusion experiments. Top: sandstones and limestone, center: sand-limestones and aerated concrete, bottom: bricks.

XRD results

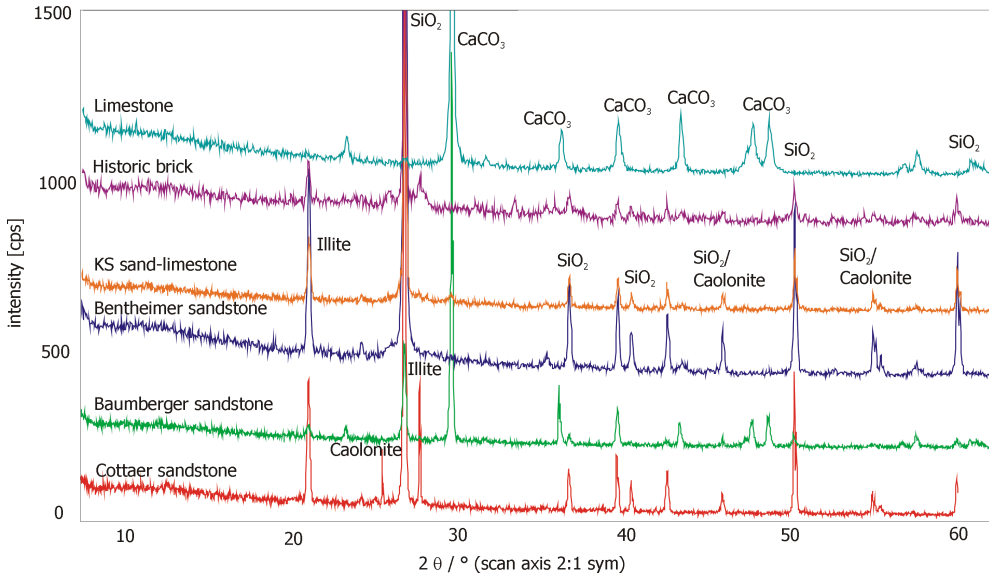
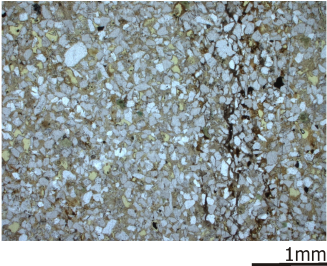


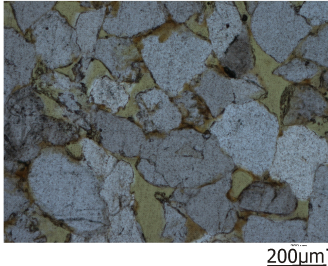
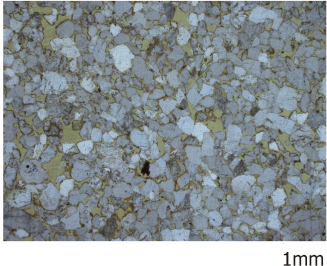
Figure A.2: The clay minerals appear to be the most abundant in the Cottaer sandstone. Bentheimer sandstone has calcite and quartz with some illite but no kaolinite and little, if any montmorrillonite. The brick (green pattern) is higher because of the scatter from the amorphous materials and also from iron and contains quartz.

Light optical microscope and Scanning electron microscope

C - Cottaer sandstone



S - Bentheimer sandstone



B - Baumberger sandstone

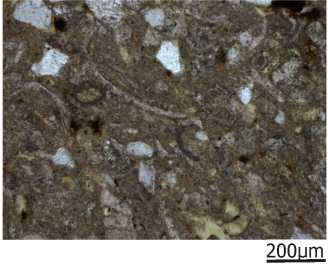
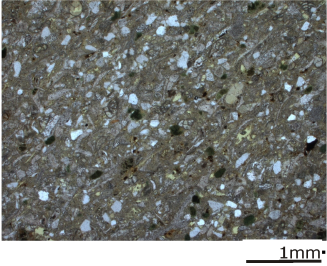
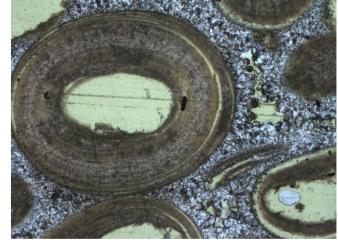
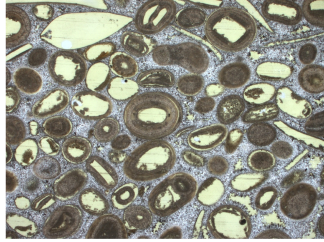
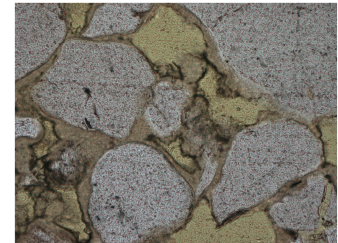
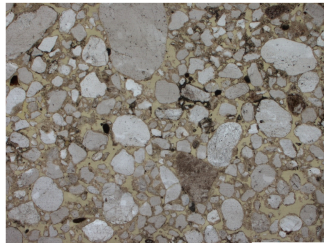


Figure A.3: Thin section images of Cottaer, Bentheimer and Baumberger sandstone made with a polarizing microscope using plain polarizing light.

SV - Savonniere
limestone



K Sand-limestone



Ha - historic
brick



Figure A.4: Thin section images of limestone, sand-limestone (type KS) and brick (type Ha) made with a polarizing microscope using plain polarizing light.

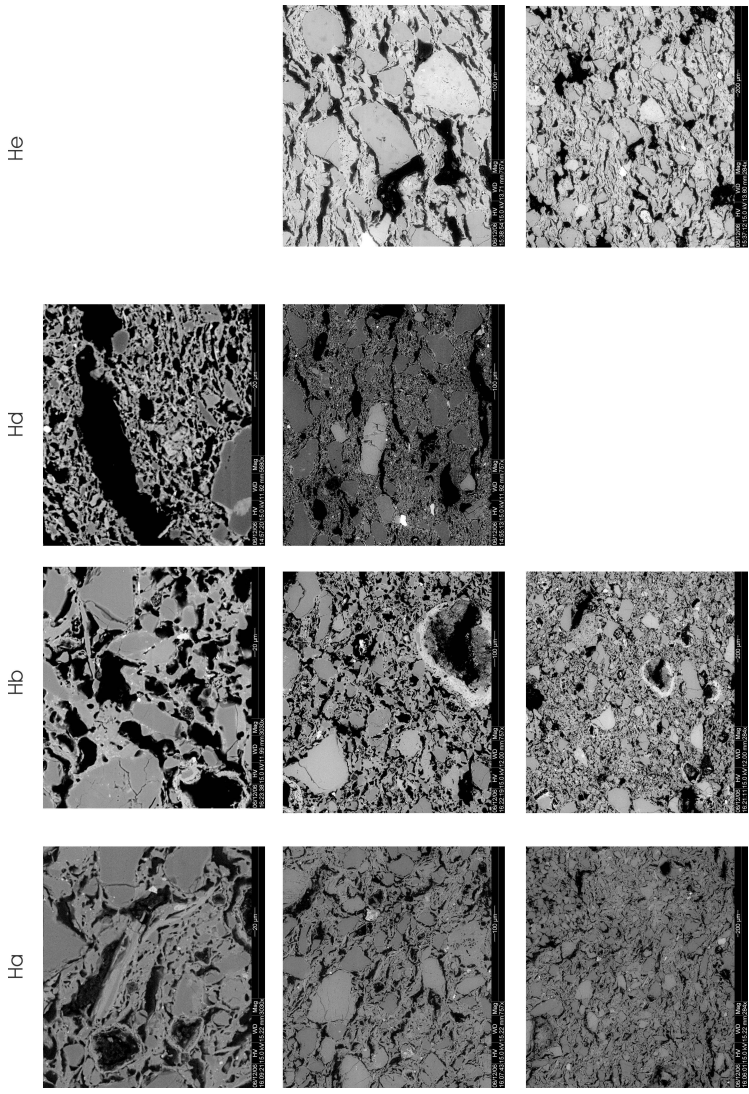


Figure A.5: Scanning electron microscope (SEM) micrographs of historic bricks Ha, Hb, Hd and He in three different resolutions. Bricks of the Ha and He type conform to a Cole-Cole behavior, whereas Hb and Hd had flat SIP responses.

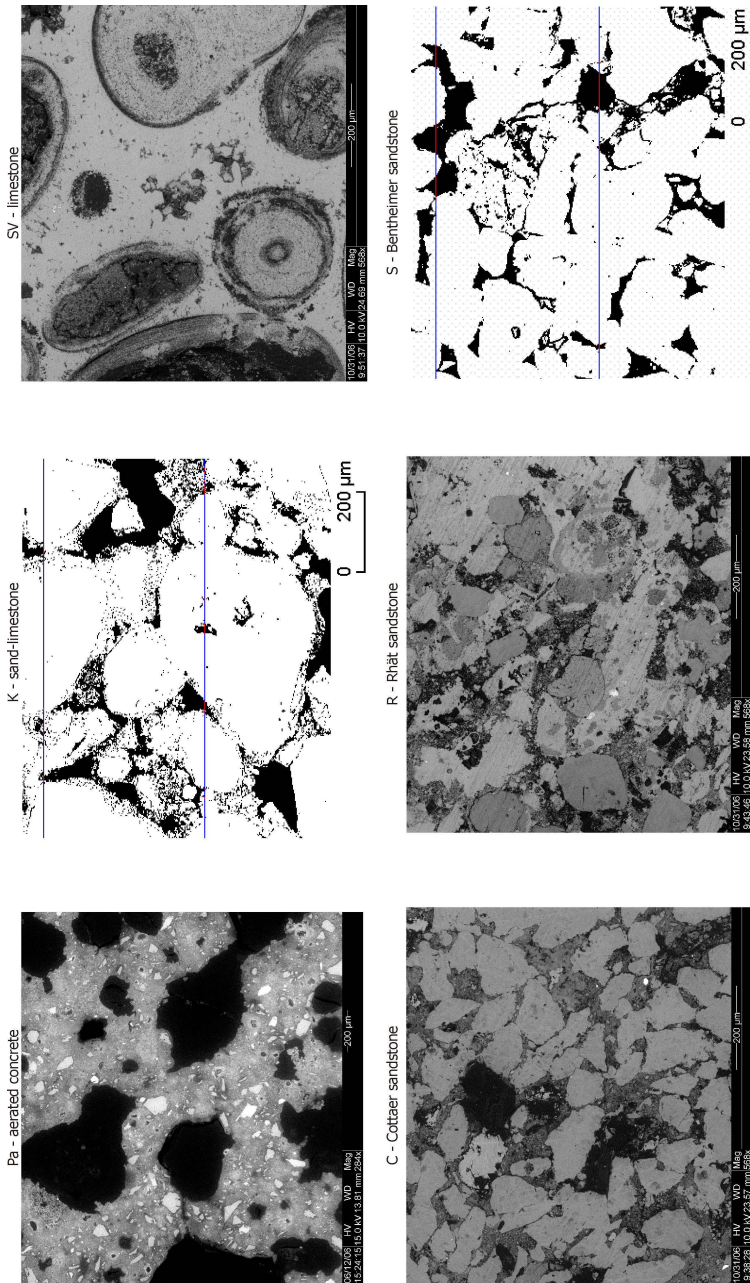


Figure A.6: Scanning electron microscope (SEM) micrographs of (first row, from left to right) Pa -aerated concrete, K - sand-limestone, SV - limestone, (bottom row, from left to right) C - Cottaer sandstone, B - Baumberger sandstone, S- Bentheimer sandstone. The micrographs of Bentheimer sandstone and sand-limestone, were obtained and processed by BAM V.1 (Th. Moelders) the others by NIST, BFRL (P. Stutzman).

B Experiment set-up and reliability tests

Sample holder and coupling medium

The key features in the design of the sample holder are the composition of the electrodes and the way the electrodes are coupled to the sample. The sample holder was constructed by BAM and accommodates cores which are 75 mm long and 20 mm in diameter. As current electrodes serve stainless steel end caps. The potential electrodes are made of German Silver, which is an Ni-Co alloy. To minimize cell effects the potential electrodes were found optimum as being ring wires placed outside the electric field and surrounding the sample at a distance of about 40 mm. The sample holder itself is of PVC (Fig. B.1).

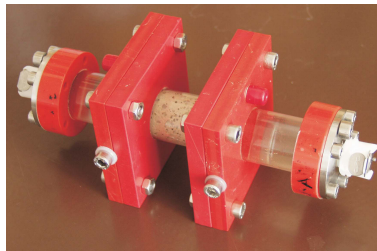


Figure B.1: BAM four point measurement cell for complex electric resistivity measurements.

The measurement cell was filled with different coupling media, which are supposed not to be polarizable and test "blank" measurements were made. Figure B.2 shows amplitude and phase spectra for fluid and Agar-gel filled sample blanks and compares them to results presented in Binley et al. (2005). Capacitive phase angles of more than 2 mrad occur for frequencies over 100 Hz. The capacitive phase angles below 100 Hz are less than 0.5 mrad and can be considered negligible for the measurements made in this study. For frequencies higher than 100 Hz capacitive coupling becomes more significant and has to be corrected before the data can be interpreted.

Reliability

The first measurements have been made with a SIP 256c device, which calculates a confidence interval from the number of subsequently measured time series partitions. This confidence intervals were usually very narrow and hence the data quality for the materials investigated seemed reliable; one example is shown in Fig. B.3, the error bars are here mostly in the range of the symbol sizes. But, the majority of the measurements

has been made with a Solartron from Solartron Analytical. This device performs a number of specified repetitions for each frequency and calculates a mean value, however, it does neither report a standard deviation nor an error. To have still some measure of uncertainty two reproducibility tests were made. Firstly, spectra which were previously measured with the SIP 256c were repeated with the Solartron and the results compared. Secondly, each CR spectrum obtained with the Solartron was at least measured twice or until a reproducible result was obtained.

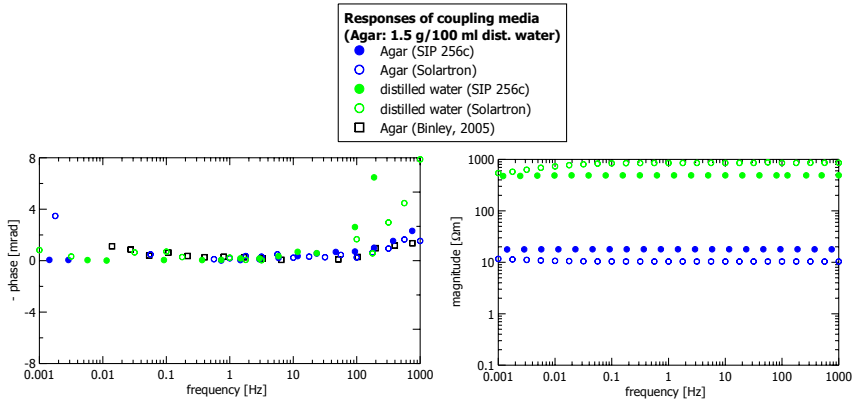


Figure B.2: CR spectra of different coupling media. Left: phases, right: magnitudes. Black boxes show the results of Agar measurements published in Binley et al. (2005) having a resistivity magnitude of $\approx 13 \Omega m$.

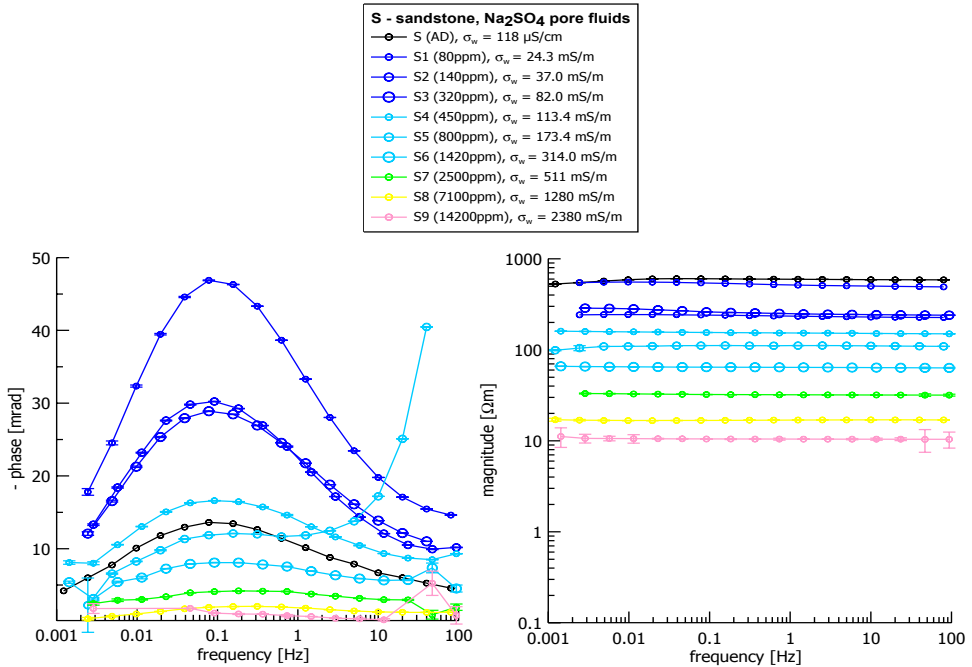


Figure B.3: CR responses and errors as measured with the SIP 256c equipment. Left: phases, right: magnitudes.

C Additional experimental results

		sandstone			limestone	sand-limestone		aerated concrete	brick			
		S	C	B	SV	K	Kc	P1	Ha	Hd	He	
distilled water ($\sigma_w = 0.2\text{mS/m}$)		x, dry	x, dry	x, dry	x, dry	x	x	x, dry	x, dry	x	x	
tap water ($\sigma_w = 60\text{mS/m}$)		x	x	x	x	x		x			x	
Conc. in ppm		Conc. in mol/l										
Na ₂ SO ₄	80	0.0008	x	x	x	x	x	x	x	x	x	
	140	0.0015	x	x	x	x	x	x	x	x	x	
	320	0.0033	x	x	x	x	x	x	x	x	x	
	450	0.0047	x	x	x	x	x	x	x	x	x	
	800	0.0083	x, dry	x, dry	x, dry	x, dry	x	x	x, dry	x, dry	x	x
	1420	0.0148	x	x	x	x	x	x	x	x	x	x
	2500	0.0260	x	x	x	x	x	x	x	x	x	x
7100	0.0739	x	x	x	x	x		x	x	x	x	
14200	0.1478	x	x	x	x	x		x	x			
MgSO ₄	80	0.0008	x	x	x	x	x	x	x			
	140	0.0015	x	x	x	x	x	x	x			
	320	0.0033	x	x	x	x	x	x	x			
	450	0.0047	x	x	x	x	x	x	x			
	800	0.0083	x	x, dry	x	x	x	x	x			
	1420	0.0148	x	x	x	x	x	x	x			
NaCl	40	0.0011	x	x	x	x	x	x	x		x	
	80	0.0023	x	x	x	x	x	x	x		x	
	160	0.0045	x	x	x	x	x	x	x		x	
	240	0.0068	x	x	x	x	x	x	x		x	
	400	0.0113	x, dry	x, dry	x, dry	x, dry	x	x	x, dry	x, dry	x	
	800	0.0226	x	x	x	x	x	x	x	x	x	
	1600	0.0451	x	x	x	x	x	x	x	x		
2400	0.0677	x	x	x	x	x		x	x			
2920	0.0824	x	x	x	x	x		x				
CaCl ₂	40	0.0011	x	x	x	x	x	x	x			
	80	0.0023	x	x	x	x	x	x	x			
	160	0.0045	x	x	x	x	x	x	x			
	240	0.0068	x	x	x	x	x	x	x			
	400	0.0113	x	x, dry	x	x	x	x	x	x		
	800	0.0226	x	x	x	x	x	x	x	x		

Figure C.1: List of the salt experiments. Salt loads are color-coded on the left according to the conservator's quantifications (Arendt and Seele, 2001). White: unloaded, light yellow: low, yellow: medium, red: high. The label "dry" identifies those samples, that were afterwards used in the evaporative desaturation study.

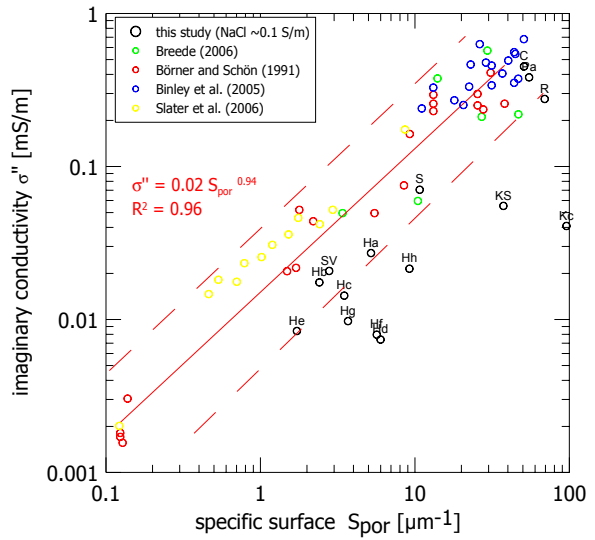


Figure C.2: Imaginary component σ'' of the complex electric conductivity versus specific surface S_{por} . Results of this study and data previously published by other authors are given for comparison.

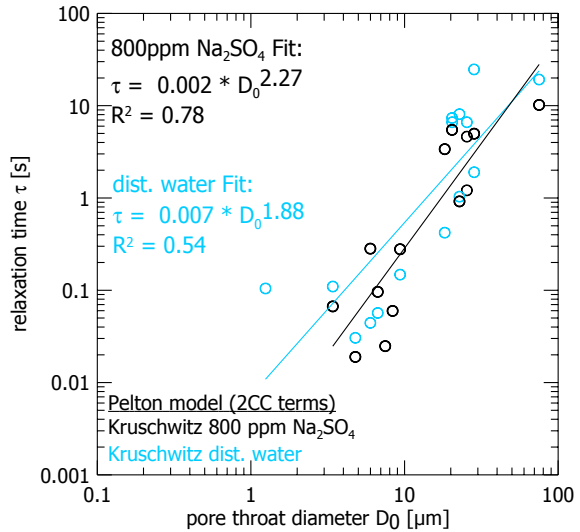


Figure C.3: C-C relaxation time τ as a function of dominant pore throat diameter. The data were fitted using SpecFit and 2 C-C terms. The data obtained on samples saturated with distilled water and 800 ppm Na_2SO_4 fluids.

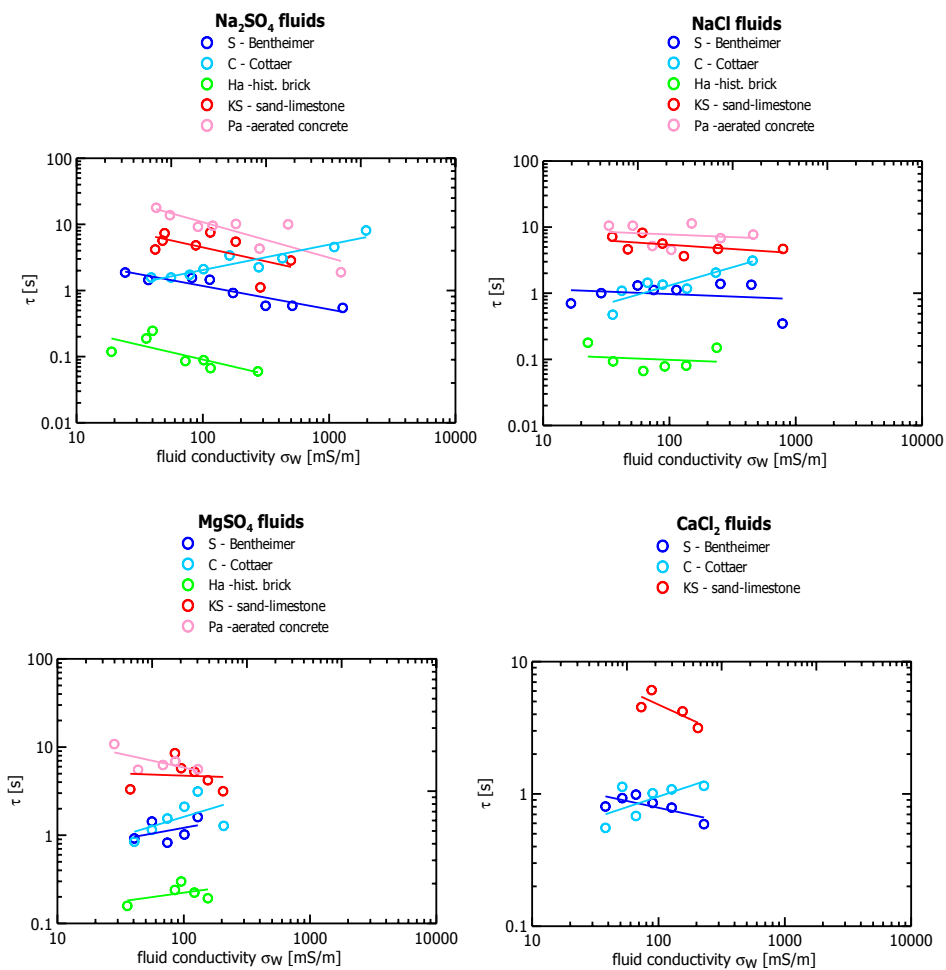


Figure C.4: C-C relaxation time τ versus fluid conductivity for the four Na_2SO_4 , $NaCl$, $MgSO_4$ and $CaCl_2$ brines.

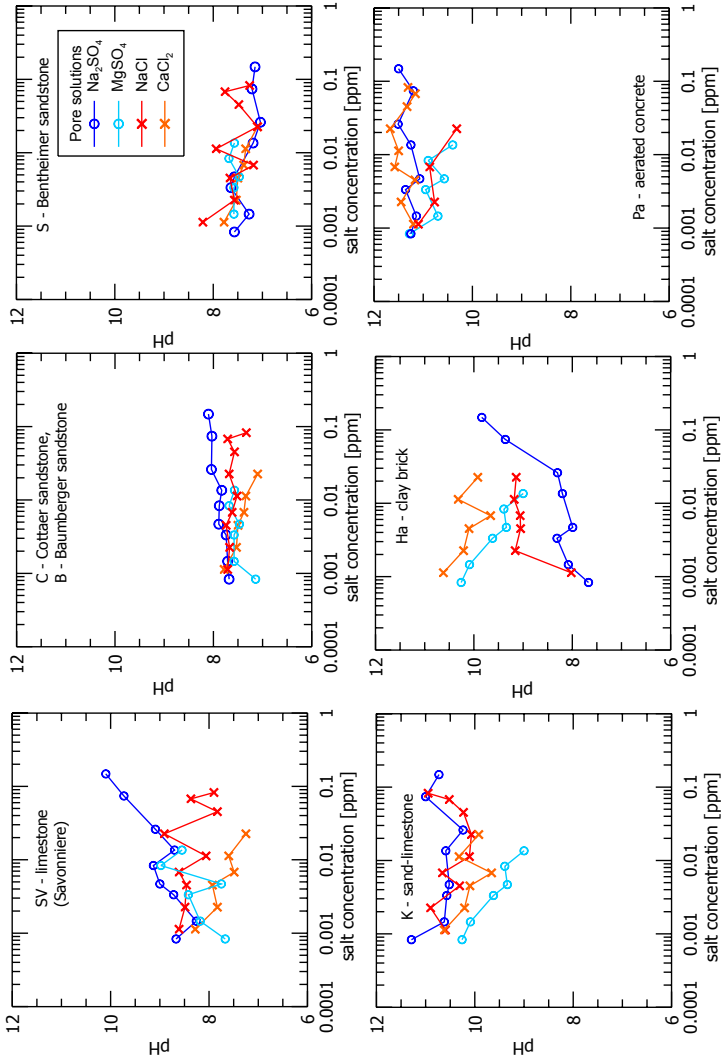


Figure C.5: Variation of pH values versus fluid conductivity for each material.

Zeta-potential

Surface production, hydroxylation of quartz The surfaces of quartz crystals (SiO_2) are highly unstable in the presence of water. Broken covalent Si-O bonds present "naked" electrical charges to the surrounding environment, which quickly get hydroxylized resulting in a surface cover of Si-OH, silanol, groups (Parks, 1984):



If the new hydroxylated surface is immersed in water, the chemical equilibria to consider are:



These equations represent the amphoteric reaction of hydroxylated silanol groups with H^+ and OH^- to produce charged surface sites. The equilibrium constants for these two equations are:

$$K_1 = \frac{[Si-OH_2^+]}{[H^+][Si-OH]} \quad \text{and} \quad K_2 = \frac{[H^+][Si-O^-]}{[Si^-]OH} \quad (C.6)$$

The condition or pH of zero charge at which macroscopic effects of charged surface groups cancel each other out is:

$$[Si-OH_2^+] = [Si-O^-] \quad (C.7)$$

so that

$$\frac{K_2}{K_1} = [H^+]^2 \frac{[Si-O^-]}{[Si-OH_2^+]} = [H^+]^2 \quad (C.8)$$

As pH is defined as minus the log of the hydrogen ion concentration, one can express the pH in terms of K_2/K_1 and, providing eq. C.8 holds,

$$pzc = pH_{pzc} = -\frac{1}{2} \log\left(\frac{K_2}{K_1}\right) \approx 3. \quad (C.9)$$

The pH at zero surface charge is defined as the pzc of the material and for quartz has been determined experimentally as approximately 3 (Parks, 1984). This is equivalent to saying that any fluid coating the surface needs to have a $[H^+]$ of approximately 10^{-3} M to produce a surface with an average neutral charge over its entire area, with the

equilibrium positions of equations C.4 and C.5 such that equal amounts of surface $[Si-O^-]$ and $[Si-OH_2^+]$ are produced.

As a consequence, if the solution saturating the surface is at a different pH than 3, for example pH 7 ($[H^+] = 10^{-7}$ M), then this reduction in the value of $[H^+]$ disturbs the equilibrium positions of the two reactions in C.4 and C.5. Equation C.4 is driven to the left hand side to provide more H^+ ; which itself reduces the value of $[Si-OH_2^+]$. Equation C.5 is driven to the right hand side to provide likewise more H^+ resulting in an increasing value for $[Si-O^-]$. In this way the surface becomes dominated with negative charges at $pH > 3$ because

$$[Si-OH_2^+] \ll [Si-O^-] \quad (C.10)$$

A similar, but opposite argument applies to the solution where the saturating fluid has a $pH < 3$. For $pH < 3$, the surface becomes dominated by positive charges, since

$$[Si-OH_2^+] \gg [Si-O^-] \quad (C.11)$$

Assuming that the value of K_2/K_1 remains constant for the range of pH 3 to 7, one can calculate the ratio of $[Si-O^-]$ to $[Si-OH_2^+]$ existing on the surface at pH 7 to be $10^8:1$, as follows:

$$\left(\frac{K_2}{K_1}\right)_{pH3} = 10^{-6} = \left(\frac{K_2}{K_1}\right)_{pH7} = \frac{[Si-O^-]_{pH7}}{[Si-OH_2^+]_{pH7}} = 10^{-14} \frac{[Si-O^-]_{pH7}}{[Si-OH_2^+]_{pH7}} \quad (C.12)$$

Therefore:

$$\frac{[Si-O^-]_{pH7}}{[Si-OH_2^+]_{pH7}} = 10^8 \quad (C.13)$$

So, at pH 7 the surface is overwhelmingly dominated by $Si-O^-$ groups. There is a reduction of 2 orders of magnitude in the $[Si-OH_2^+]:[Si-O^-]$ ratio for a pH change of 1, so by the time pH 7 is reached, the number of surface $Si-OH_2$ groups is negligibly small.

Particle sizes of materials used in electroacoustic measurements Figure C.6 shows the particle size distributions of the micronized material powders used for the zeta-potential measurements. The median particle sizes (d_{50}) are between 1 and 3 μm , which is the upper limit for getting reliable results with the MATEC 9800 equipment used in this study. The PSD measurements were done on a Malvern Instruments Mastersizer 2000. This equipment uses the laser defraction technique, where the angular distribution of light is measured after passing through an optically dilute dispersion of suspended particles. The dispersent used was Isopropyl Alcohol.

Zeta-potential versus pH In Fig. C.7 is the measured zeta-potential shown as a function of suspension pH. The dependence of the zeta-potential on pH (2-11) is widely known for many materials. For the experiments here the pH of the suspensions was not changed in terms of adding acid or base, it just varies somewhat by the stepwise addition of salt. As the figure shows for most materials the zeta-potentials vary only within a range of 0.5

pH units, which can be considered negligible. Consequently, the zeta-potential variations observed here can be assumed to occur due the addition of salt. The black labels denote the amount of salt added in units mol/L.

Results Figure C.8 shows the zeta-potential (top) and the diffuse layer surface charge density (bottom) for all material / salt combinations measured as a function of the ratio of the quadrature conductivity and real conductivity.

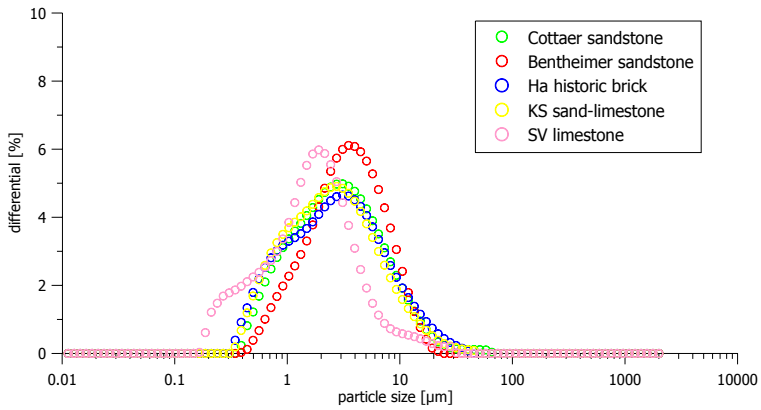


Figure C.6: Particle size distributions of the micronized samples used for electroacoustic measurements.

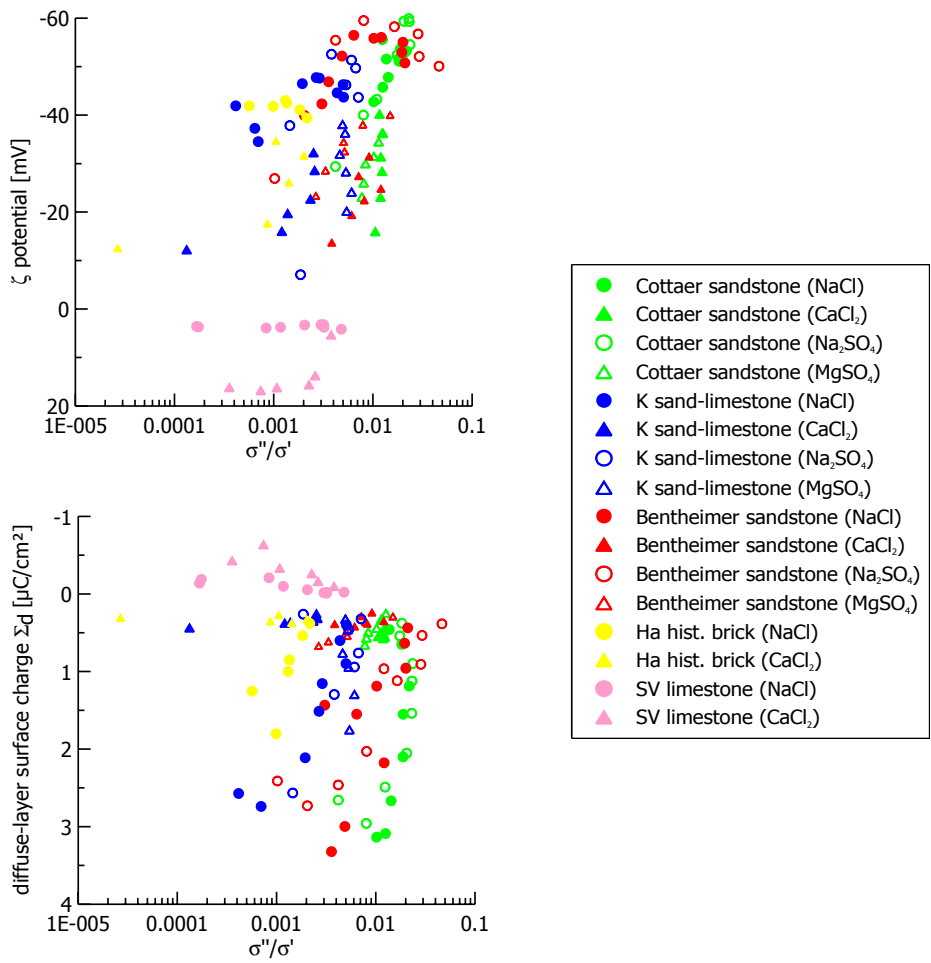


Figure C.8: Zeta-potential (top) and diffuse layer surface charge Σ_d (bottom) as a function of the ratio σ''/σ' for all materials and salt concentrations measured.

D FD modelling with Ac2D

Testing the algorithm

In order to test the effective impedance algorithm Ac2D simple test microstructures have been generated, which's modelling results could likewise easily be calculated using an equivalent test network. The resistivities of conductive layers or blocks of a test microstructure are calculated as $R_{el.network} = R_{Ac2D} * \text{length} / \text{height}$. Naturally, in a test network only currents in the x-direction, not in y-direction exist. The exact same CR responses will hence only result for microstructures having only vertical layer boundaries. If horizontal layer boundaries exist, it will immediately also result in vertical current flow, which cannot be simulated in an electrical circuit.

To prove the correctness of the effective impedance modelling in Ac2D a variety of test structures was generated and the results compared to the theoretical predictions of an equivalent test circuit. The responses of three such structures are shown in Fig. D.1. The electrical circuits are depicted on the left and the Ac2D microstructures on the right. Note, that model 2 and 3 do have horizontal layer boundaries and therefore, some deviation of the two results may be expected. The comparison of the results in the bottom fraction proves, that the effective impedance program works reliably. Even for the second model, where the interface is quite highly resistive and y-currents should be low, the two results match. Only for the third model, where considerably more currents in y-direction flow, because the horizontal layers are similar in their conductivities, some visible deviation results. The simulations, however, substantiate the plausibility of the program.

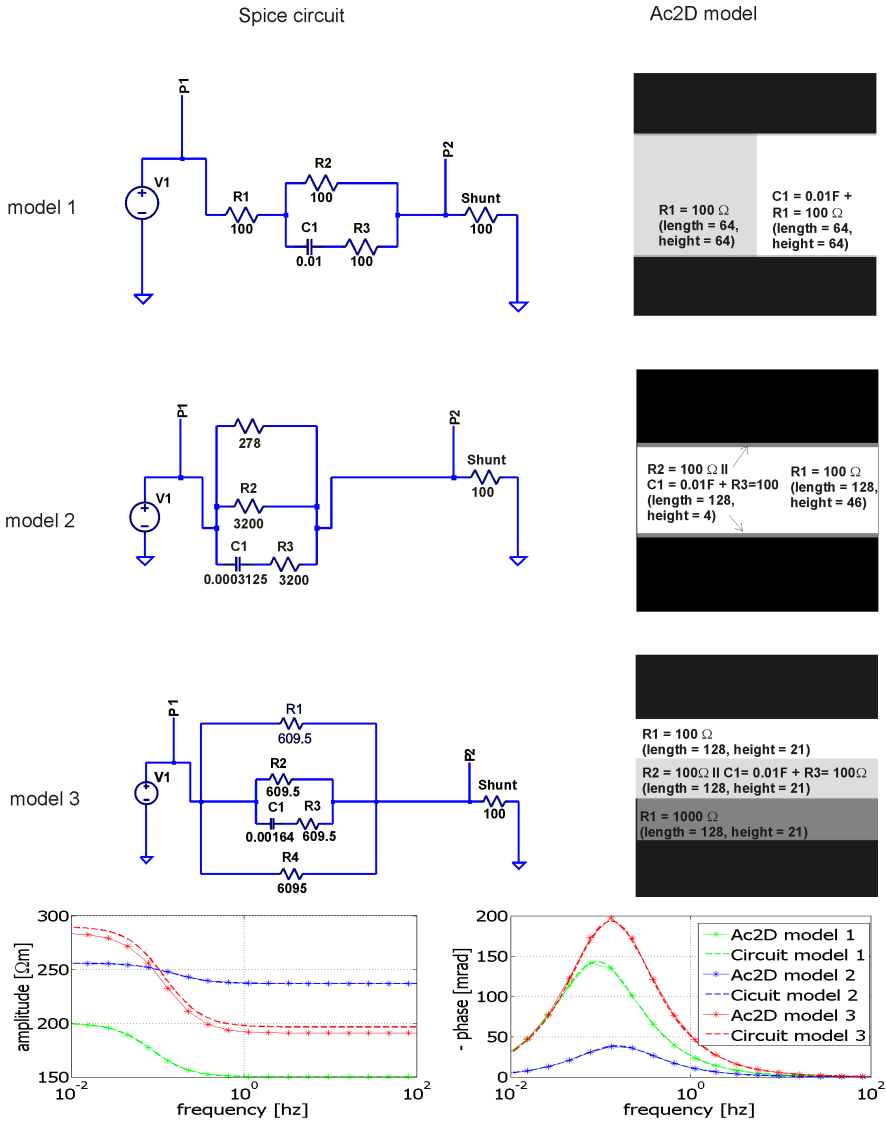


Figure D.1: Three models as Ac2D microstructures (right) and equivalent electrical circuits (left). The CR spectra of the two are compared in the lower figure section.

Conductivity components of the interface using the triple model

Each pixel in Ac2D is assigned a real and a quadrature conductivity component. If the "triple model" shown in Fig. 6.2 is used, the total conductivity of interface pixels is:

$$\sigma_{iL}^* = \frac{R_1 \omega^2 C^2 + i \omega C}{1 + R_1^2 \omega^2 C^2} + \frac{1}{R_2} \quad (D.1)$$

$$\sigma_{iL}^* = \frac{(R_1 \omega^2 C^2 + i \omega C) R_2}{(1 + R_1^2 \omega^2 C^2) R_2} + \frac{1 + R_1^2 \omega^2 C^2}{R_2 (1 + R_1^2 \omega^2 C^2)} \quad (D.2)$$

$$\sigma_{iL}^* = \frac{R_2 R_1 \omega^2 C^2 + i \omega C R_2 + 1 + R_1^2 \omega^2 C^2}{R_2 (R_1^2 \omega^2 C^2 + 1)} \quad (D.3)$$

This term can easily be separated in real part and imaginary part as follows:
real part:

$$\sigma'_{iL} = \frac{R_1 \omega^2 C^2 (R_2 + R_1) + 1}{R_2^2 (R_1^2 \omega^2 C^2 + 1)} \quad (D.4)$$

and imaginary part:

$$\sigma''_{iL} = \frac{i \omega C R_2}{R_2 (R_1^2 \omega^2 C^2 + 1)} \quad (D.5)$$

These were the terms, that were used as real and imaginary components for each interface pixel throughout the modelling. For all model results the values used for R1, C1 and R2 are given in the figure captions or in the corresponding text fraction.

List of Symbols and Abbreviations

Table 4.1: Roman symbols.

Symbol	Meaning	Dimension
c	(a) concentration (b) exponent (Cole-Cole model)	mol/m^3 or mol/L none
d_M	matrix density	g/m^2
D	dielectric displacement field	C/m^2
D_i	diffusivity (of ion species i)	$m^2/s/K$
D_0	average pore throat diameter	m
E	electric field	V/m
e	electronic charge ($1.60217646 \times 10^{-19}$)	C
f	technical Frequency	Hz
F	(a) formation factor (b) Faraday's constant ($eN_A = F = 96485.3$)	none C/mol
H	magnetic field	A/m
I	(a) electrical current (b) ionic strength	A mol/m^3
J	electrical current density	A/m^2
k	(a) configuration factor (b) hydraulic conductivity	m m/s
k_B	Boltzmann's constant (1.38066×10^{-23})	J/K
M	cementation index (Archie model)	none
m	chargeability (Cole-Cole model)	none
N_A	Avogadro's number (6.02214×10^{23})	$1/mol$
n	saturation exponent (for σ_w)	none
n^0	concentration number ($= c[mol/L] * 1000 * N_A$)	$1/m^3$
q	electric charge density	$C/m^3, eq/m^3$
R	gas constant ($k_B N_A = R = 8.31541$)	$J/K/mol$
S_M	surface area per mass	m^2/g
S_{por}	surface area related to porosity (specific surface)	$1/\mu m^2$
T	(a) absolute temperature (b) tortuosity	K none
z	charge number	none
Z	electrical impedance	$m^2/V/s$

Table 4.2: Greek symbols.

Symbol	Meaning	Dimension
β	Debye screening length	m
Γ	surface excess charge	meq/L
ϵ_r	dielectric constant	none
ϵ_0	electrical permittivity of free space (8.85419×10^{-12})	$A\ s/V/m$
ϵ	dielectric permittivity	$A\ s/V/m$
ζ	zeta-potential	V
η	viscosity	kg/m/s or Pa s
μ_0	magnetic permeability of free space (1.256637×10^{-6})	$V\ s/A/m$
μ_d	electrophoretic mobility	mol s/kg or $m^2/V/s$
μ_i	ion mobility (of ion species i)	$m^2/V/s^1$
μ_s	effective surface ionic mobility	$m^2/V/s^1$
ν	(a) saturation exponent (for σ_{surf}) (b) kinematic viscosity	none m^2/s
ρ_s	apparent electrical resistivity	Ω
ρ	specific electrical resistivity	Ωm
Φ	effective porosity	none
ϕ	phase	$^\circ$ or mrad
σ	electrical conductivity	S/m
σ_{eff}	effective electrical conductivity of a material composite	S/m
σ_{surf}	electrical surface conductivity	S/m
σ_{bulk}	electrical bulk conductivity	S/m
σ_w	electrical fluid conductivity	S/m
Σ_t	total surface charge density	C/m^2 or eq/m^2
Σ_f	fixed-layer surface charge density	C/m^2 or eq/m^2
Σ_d	diffuse-layer surface charge density	C/m^2 or eq/m^2
τ	relaxation time (Cole-Cole model)	s
ω	angular frequency	rad/s

List of Figures

- 2.1 Complex resistivity signal for a distinct frequency. The applied voltage (V) causes a subsequent current (A) signal, which is shifted in time. The amplitude ratio of the two signals is the resistivity magnitude (Ωm due to geometrical considerations of sample diameter and length) and their time shift is related to as phase angle ϕ (mrad or deg). 9
- 2.2 Equivalent circuit for the electrical response of rocks and soils after Lesmes and Frye (2001). Electrolytic conduction in the bulk pore is assumed to be purely resistive, the high frequency dielectric constant ϵ_r represents the high frequency dielectric constant, and σ_{surf}^* is the complex conductivity. . 10
- 2.3 Schematic of ion-conductive zones in porous rocks after Titov et al. (2004).(1) Excess and deficiency in ion concentration around a polarized spherical negatively charged particle. The solid arrow shows the direction of the electrical field, the dotted shows the diffusion flow of both, anions and cations and the dashed arrow shows the local diffusion flow near the surface mostly by cations. (2) Excess and deficiency along a polarized pore throat. (3) Schematic distribution of the ion concentration around a polarized spherical particle or along a polarized pore throat. C^* denoted the excess concentration produced by the polarizing field. 12
- 2.4 Three layer model of the electrical double layer as shown in Lorne et al. (1999). IHP: Internal Helmholtz plane; OHP: outer Helmholtz plane; ISCP: internal surface charge plane, OSCP: outer surface charge plane. The zeta-potential is defined as the electric potential at the shear plane, located at a distance s from the Stern plane. 13
- 2.5 Debye lengths as a function of salt concentrations for Na_2SO_4 and NaCl (monovalent cations) and $MgSO_4$ and $CaCl_2$ (divalent cations). The Debye length of salts with monovalent cations are larger compared to salts with divalent cation at the same concentration. Black labels denote the salt concentrations in units of parts per million (ppm). 17

2.6 The liquid layer surrounding the particle exists as two parts: an inner region (Stern layer), where the ions are strongly bound and an outer (or diffuse) region, where the ions are less firmly attached. When a particle moves, ions within a notional boundary of the diffuse layer will move with it, any ions beyond this boundary do not travel with the particle. This boundary is the surface of hydrodynamic shear or slipping plane. The electrical boundary at this plane is referred to as the zeta-potential. 18

2.7 Variation of the ζ -potential with electrolyte concentration measured for silica surfaces and 1:1 electrolyte. Source: Revil et al. (1999). Results of different publications are plotted: Ref.1: Gaudin and Fuerstenau (1995), Ref.2: Li and de Bruyn (1966), Ref.3: Watillon and de Backer (1970), as well as the model prediction of Revil et al. (1999). 20

3.1 Scheme of the measurement cell used. As potential leads serve German Silver wires sitting in PVC chambers. As current electrodes were used stainless steel caps at the front and end of the cell. Electrodes were coupled either with agar gel or water to the specimen. 31

3.2 CR phase spectra of three different materials classes: Top left: sandstones, top right: aerated concrete, limestone, mortar and concrete, bottom left: sand-limestones, bottom right: historic and modern fired clay bricks. All samples were saturated with distilled water. 34

3.3 Imaginary component of the complex electric conductivity σ'' specific versus surface S_{por} as measured on building material samples saturated with distilled water and results of previous works by other authors. 36

3.4 Imaginary component of the complex electric conductivity σ'' specific versus surface S_{por} as measured on building material samples saturated with Na_2SO_4 and results of previous works by other authors. The red lines enclose 68% of the data (Gaussian standard deviation). 36

3.5 Frequency at which the maximum phase value was observed after saturation with distilled water versus dominant pore throat diameter (MICP). 37

3.6 Maximum phase value as measured for each material after saturation with distilled water versus dominant pore throat diameter (MICP). 37

3.7 Variation of specific surface S_{por} with dominant pore throat diameter D_0 . 38

3.8 Imaginary conductivity σ'' at peak frequency as a function of the dominant pore throat diameter D_0 , increasing bubble sizes denote increasing specific surface S_{por} . Measurement results for samples saturated with distilled water. 38

3.9 Bentheimer sandstone, CR phase spectra measured on samples with varying sulfate and chloride concentrations. From top left to bottom right: Na_2SO_4 , $MgSO_4$, $NaCl$, $CaCl_2$ 40

3.10 Cottaer sandstone, CR phase spectra measured on samples with varying sulfate and chloride concentrations. From top left to bottom right: Na_2SO_4 , $MgSO_4$, $NaCl$, $CaCl_2$	41
3.11 Baumberger sandstone, CR phase spectra measured on samples with varying sulfate and chloride concentrations. From top left to bottom right: Na_2SO_4 , $MgSO_4$, $NaCl$, $CaCl_2$	42
3.12 Savonnières limestone (SV), CR phase spectra measured on samples with varying sulfate and chloride concentrations. From top left to bottom right: Na_2SO_4 , $MgSO_4$, $NaCl$, $CaCl_2$	43
3.13 CR phase spectra of a) fabricated sand-limestone (K), b) aerated concrete (Pa), c) historic brick samples (Ha) and d) historic brick sample He. All samples were saturated with Na_2SO_4 brines of the same concentrations.	44
3.14 Formation factor F versus porosity Φ for the different building materials.	46
3.15 Imaginary part (left), bulk (middle) conductivity and ratio of imaginary and real conductivity (right) versus fluid conductivity for three different sandstones.	47
3.16 Imaginary part (left), bulk (middle) conductivity and the ratio of imaginary and real conductivity (right) versus fluid conductivity for a limestone sample, a sand-limestone and an aerated concrete.	48
3.17 Imaginary part (left), bulk (middle) conductivity and the ratio of imaginary and real conductivity (right) versus fluid conductivity for three different bricks.	49
3.18 Relaxation time τ as resulting from the C-C data fitting routine SpecFit for the low relaxation term versus fluid conductivity.	52
3.19 Normalized chargeability m_{norm} as resulting from the C-C data fitting routine SpecFit for the low relaxation term versus fluid conductivity.	53
3.20 Cole-Cole exponent c as resulting from the C-C data fitting routine SpecFit for the low relaxation term versus fluid conductivity.	54
3.21 CR phase spectra of saturated building materials. Results of samples saturated with distilled water (small circles) are compared to saturations with tap water (big circles).	56
3.22 Real components of the electrical conductivity for samples saturated with distilled (grey) and tap water (pink) respectively.	57
3.23 Imaginary components of the electrical conductivity for samples saturated with distilled (grey) and tap water (pink) respectively.	57
3.24 Change of the real conductivity component σ' between distilled and tap water saturated samples.	58
3.25 Change of the imaginary conductivity component σ'' between distilled and tap water saturated samples.	58

3.26 Correlation of relaxation time τ and pore throat diameter D_0 . Black: Results presented in this study. Blue: results presented by Binley et al. (2005), red: results presented by Scott and Barker (2005), green: results presented in Breede (2006b). The two dashed lines enclose 68% of the data (Gaussian standard deviation). 60

3.27 Diffusion coefficients D_i of aqueous salt solutions at 25° C after Lobo (1984). 61

4.1 CR spectra (phase left, magnitude right) for a Cottaer sandstone sample (C, top) and a historic brick sample (Ha, center) and an aerated concrete (Pa, bottom) under different water saturations. All samples were originally saturated with distilled water. 65

4.2 Variation of the C-C relaxation time, τ , normalized chargeability, m_{norm} , and C-C exponent, c , with saturation for aerated concrete (Pa (left)) and historic brick (Ha (right)) samples. 67

4.3 Dependence of the real and imaginary conductivity on saturation during evaporative drying. Top: Cottaer sandstone, middle: Bentheimer sandstone, bottom: Baumberger sandstone. The lines show power law fits from which saturation exponents were estimated. 69

4.4 Dependence of the real and imaginary conductivity on saturation during evaporative drying. Top: Aerated concrete, middle: historic brick (Ha), bottom: Savonniere limestone. The lines show power law fits from which saturation exponents were estimated. 70

4.5 Saturation exponents n (real component σ') versus ν (imaginary component σ''). The black circles show the results measured by Ulrich and Slater (2004) on unconsolidated sands. 71

5.1 Signal loss of zeta-potential in electroacoustic measurements as a function of particle size after Flatt and Ferraris (2002). 76

5.2 Top: zeta-potential inferred from electroacoustic measurements using crushed and micronized Cottaer sandstone, as a function of suspension conductivity. Bottom: zeta-potential inferred from electroacoustic measurements using only ionic solutions and *no* material powders. The results of different ions varying in valence are compared. Black labels denote the salt concentration in units mmol/L. 78

5.3 Comparison of the zeta-potential inferred from electroacoustic measurements on crushed and micronized Cottaer and Bentheimer sandstones, a historic brick (type Ha), a sand-limestone (type KS) and a limestone (type SV) sample as a function of NaCl (top) and $CaCl_2$ (bottom) suspension conductivity. Black labels denote the salt concentration in units mmol/L. 79

5.4	Cottaer sandstone, titration curves. Upper three diagrams show the titration curves for one ionic strength including the uncorrected suspension, the background measurement as well as the corrected suspension curves. The bottom diagram includes the background corrected titration curves for the three ionic strengths.	82
5.5	Zeta potential (top) and diffuse layer charge Σ_d (bottom) as a function of imaginary conductivity σ'' for all materials and salt concentrations. Black labels denote salt contents in units mmol/L exemplarily for Cottaer sandstone.	84
5.6	Diffuse layer charge Σ_d as a function of imaginary conductivity σ'' for each material separately. The black labels denote the salt concentration in mmol/L.	85
5.7	Fixed layer charge density Σ_f and diffuse layer charge density Σ_d as a function of fluid conductivity σ'' for Cottaer sandstone and NaCl solutions. . .	86
6.1	Illustration of how periodic boundary conditions are implemented in the finite difference program AC2D after Garboczi (1998).	91
6.2	Equivalent circuit used in the approach to model microstructural effects on complex resistivity behavior. The model is similar to the traditional Debye model simulating the electrical double layer in a parallel connection of resistor and resistor and capacitor in parallel.	92
6.3	Series of different interface shapes. Models are shown in the top fraction (1 through 6 from upper left to lower right corner) and IP spectra below. The upper two CR diagrams are the results for a fluid conductivity of $\sigma_w = 1$ S/m, in the middle $\sigma_w = 0.01$ S/m and on the bottom $\sigma_w = 0.0001$ S/m. The interface conductivity is constant for all models with $\sigma_{R1} = 0.01$ S/m, $C1 = 0.01$ F, $\sigma_{R2} = 0.01$ S/m.	94
6.4	Model set 1: series of different pore throat shapes. Models are shown in the top fraction and CR spectra below. The upper two CR diagrams are the results for a fluid conductivity of $\sigma_w = 1$ S/m, in the middle $\sigma_w = 0.01$ S/m and on the bottom $\sigma_w = 0.0001$ S/m. The interface conductivity is constant for all models with $\sigma_{R1} = 0.01$ S/m, $C1 = 0.01$ F, $\sigma_{R2} = 0.01$ S/m.	95
6.5	Model set 2: series of different pore throat shapes. Models are shown in the top fraction and IP spectra below. The upper two CR diagrams are the results for a fluid conductivity of $\sigma_w = 1$ S/m, in the middle $\sigma_w = 0.01$ S/m and on the bottom $\sigma_w = 0.0001$ S/m. The interface conductivity is constant for all models with $\sigma_{R1} = 0.01$ S/m, $C1 = 0.01$ F, $\sigma_{R2} = 0.01$ S/m.	96
6.6	Model set 3: series of different pore throat shapes. Models are shown in the top fraction and IP spectra below. The upper two CR diagrams are the results for a fluid conductivity of $\sigma_w = 1$ S/m, in the middle $\sigma_w = 0.01$ S/m and on the bottom $\sigma_w = 0.0001$ S/m. The interface conductivity is constant for all models with $\sigma_{R1} = 0.01$ S/m, $C1 = 0.01$ F, $\sigma_{R2} = 0.01$ S/m.	97

6.7 Model set 1: series of changing interface thicknesses. Models are shown in the top fraction (1 through 7 from upper left to lower right corner) and IP spectra below. The upper two CR diagrams are the results for a fluid conductivity of $\sigma_w = 1$ S/m, in the middle $\sigma_w = 0.01$ S/m and on the bottom $\sigma_w = 0.0001$ S/m. The interface conductivity is constant for all models with $\sigma_{R1} = 0.01$ S/m, $C1 = 0.01$ F, $\sigma_{R2} = 0.01$ S/m. 99

6.8 Model set 2: series of changing interface thicknesses. Models are shown in the top fraction (1 through 7 from upper left to lower right corner) and IP spectra below. The upper two CR diagrams are the results for a fluid conductivity of $\sigma_w = 1$ S/m, in the middle $\sigma_w = 0.01$ S/m and on the bottom $\sigma_w = 0.0001$ S/m. The interface conductivity is constant for all models with $\sigma_{R1} = 0.01$ S/m, $C1 = 0.01$ F, $\sigma_{R2} = 0.01$ S/m. 100

6.9 CR responses for the models shown in Fig. 6.8 for intermediate fluid conductivities. Top down σ_w changes from 0.01, 0.005, 0.001 to 0.0001 S/m. The interface conductivity is constant for all models with $\sigma_{R1} = 0.01$ S/m, $C1 = 0.01$ F, $\sigma_{R2} = 0.01$ S/m. 101

6.10 Set of four models to study the effect of an increasing fluid conductivity σ_w . Models are shown in the top fraction and CR spectra below. The interface conductivity is constant for all models being $\sigma_{R1} = 0.01$ S/m, $C1 = 0.01$ F, $\sigma_{R2} = 0.01$ S/m. 103

6.11 Model set 1: series of models varying in saturation, the interface is continuous. A fourth phase (dark grey) is introduced symbolizing air and having a conductivity of $\sigma_{air} = 0$ S/m like the matrix. Models are shown in the top fraction, CR spectra below. The upper CR diagram is for a constant interface conductivity, the lower for a interface conductivity increasing together with fluid conductivity σ_w 105

6.12 Model set 2: series of models varying in saturation, interface only existent in pore throats. A fourth phase (dark grey) is introduced symbolizing air and having a conductivity of $\sigma_{air} = 0$ S/m like the matrix. Models are shown in the top fraction, CR spectra below. The upper CR diagram is for a constant interface conductivity, the lower for a interface conductivity increasing together with fluid conductivity σ_w 107

6.13 Normalized saturation exponents for the models in Fig. 6.11 and 6.12. 108

6.14 Model set with varying porosities Φ . From model 1 (top left) to model 6 (bottom right) Φ takes the values 0.08, 0.23, 0.39, 0.55, 0.70, 0.85. 109

6.15 Formation factor F versus porosity Φ for the model sets shown in Fig. 6.4, 6.6 and 6.14. Fluid conductivity $\sigma_w = 0.01$ S/m 110

6.16 Tortuosity calculated from the formation factor F versus tortuosity calculated from geometrical and electrical characteristic length scales for the model sets shown in Fig. 6.4 and 6.6. Black labels denote porosities. 110

A.1	Pore size distributions (PSD) of the materials under investigation determined in mercury intrusion experiments. Top: sandstones and limestone, center: sand-limestones and aerated concrete, bottom: bricks.	121
A.2	The clay minerals appear to be the most abundant in the Cottaer sandstone. Bentheimer sandstone has calcite and quartz with some illite but no kaolinite and little, if any montmorillonite. The brick (green pattern) is higher because of the scatter from the amorphous materials and also from iron and contains quartz.	122
A.3	Thin section images of Cottaer, Bentheimer and Baumberger sandstone made with a polarizing microscope using plain polarizing light.	123
A.4	Thin section images of limestone, sand-limestone (type KS) and brick (type Ha) made with a polarizing microscope using plain polarizing light.	124
A.5	Scanning electron microscope (SEM) micrographs of historic bricks Ha, Hb, Hd and He in three different resolutions. Bricks of the Ha and He type conform to a Cole-Cole behavior, whereas Hb and Hd had flat SIP responses.	125
A.6	Scanning electron microscope (SEM) micrographs of (first row, from left to right) Pa -aerated concrete, K - sand-limestone, SV - limestone, (bottom row, from left to right) C - Cottaer sandstone, B - Baumberger sandstone, S- Bentheimer sandstone. The micrographs of Bentheimer sandstone and sand-limestone, were obtained and processed by BAM V.1 (Th. Moelders) the others by NIST, BFRL (P. Stutzman).	126
B.1	BAM four point measurement cell for complex electric resistivity measurements.	127
B.2	CR spectra of different coupling media. Left: phases, right: magnitudes. Black boxes show the results of Agar measurements published in Binley et al. (2005) having a resistivity magnitude of $\approx 13 \Omega m$	129
B.3	CR responses and errors as measured with the SIP 256c equipment. Left: phases, right: magnitudes.	129
C.1	List of the salt experiments. Salt loads are color-coded on the left according to the conservator's quantifications (Arendt and Seele, 2001). White: unloaded, light yellow: low, yellow: medium, red: high. The label "dry" identifies those samples, that were afterwards used in the evaporative desaturation study.	131
C.2	Imaginary component σ'' of the complex electric conductivity versus specific surface S_{por} . Results of this study and data previously published by other authors are given for comparison.	132
C.3	C-C relaxation time τ as a function of dominant pore throat diameter. The data were fitted using SpecFit and 2 C-C terms. The data obtained on samples saturated with distilled water and 800 ppm Na_2SO_4 fluids.	132

C.4	C-C relaxation time τ versus fluid conductivity for the four Na_2SO_4 , $NaCl$, $MgSO_4$ and $CaCl_2$ brines.	133
C.5	Variation of pH values versus fluid conductivity for each material.	134
C.6	Particle size distributions of the micronized samples used for electroacoustic measurements.	137
C.7	Zeta-potential as a function of pH for the materials and salt concentrations used.	138
C.8	Zeta-potential (top) and diffuse layer surface charge Σ_d (bottom) as a function of the ratio σ''/σ' for all materials and salt concentrations measured.	139
D.1	Three models as Ac2D microstructures (right) and equivalent electrical circuits (left). The CR spectra of the two are compared in the lower figure section.	142

List of Tables

1.1	Most common deterioration salts. Source: Kabrede (2003).	4
2.1	Debye lengths β in [nm] at various concentrations of aqueous solutions at 298 ° K according to eq. 2.27. The charge type of the electrolyte is given as charge of the cation dash charge of the anion in the headerline.	16
2.2	Ion mobilities at extreme dilution in aqueous solution at 298 K. (after Oldham and Myland (1994))	20
2.3	Overview of simple relaxation models after Pelton et al. (1983). The last two columns indicate the low and high frequency phase angle asymptotic slopes. 23	
3.1	Examination methods for the petrophysical and mineralogical charaterization. 29	
3.2	Deterioration levels of salts. Source: Arendt and Seele (2001)	29
3.3	Physical characteristics of the building material samples under investigation. The cross in the salt column marks those materials that were investigated in the salt concentration study. Abbreviations: AD - distilled water.	30
3.4	Formation factors F and interface (intercept) conductivities σ_q in [mS/m] of the building material samples under investigation as obtained in the multiple salinity measurements.	46
3.5	Power law fit results of relaxation time τ versus fluid conductivity (Fig. 3.18.) 50	
3.6	Ion concentrations c in mol/L as used for CR measurements and data shown in Fig. 3.26.	59
4.1	Physical characteristics and saturation exponents of the real (n) and imaginary (ν) conductivity components as determined in evaporative desaturation experiments.	68
5.1	Physical properties and zeta-potentials measured for suspensions in distilled water, and in ≈ 0.011 mol/L (400 ppm) NaCl and $CaCl_2$ respectively. 80	
6.1	Desaturation properties of the models in Fig. 6.11 and 6.12.	104
A.1	DIN classification of the sand-limestones used in this study.	120
4.1	Roman symbols.	145
4.2	Greek symbols.	146

Bibliography

- Analytical, S., 2007. <http://www.solartronanalytical.com/downloads/datasheets/1260.pdf>. 3.1.3
- Archie, G., 1942. Electrical resistivity as an Aid in Core Analysis Interpretation. Trans. AIME 146, 54-61. 2.5, 3.4
- Arendt, C., Seele, J., 2001. Feuchte und Salz in Gebäuden. Vol. 2. Verlagsanstalt Alexander Koch GmbH, Leinfelden-Echterdingen. 3.2, C.1, 7, 7
- Bard, Allen, J., Faulkner, Larry, R., 2001. Electrochemical Methods: Fundamentals and Applications. John Wiley and Sons Inc. 5.2
- Binley, A., Slater, Lee, D., Fukes, M., Cassiani, G., 2005. Relationship between spectral induced polarization and hydraulic properties of saturated and unsaturated sandstone. Water Resources Research 41, W12417. 1.1, 2.5, 3.2.2, 3.7, 3.6, 3.26, 4.2.1, 4.2.2, 4.3, B, B.2, 7
- Börner, F., 1992. Complex conductivity measurements of reservoir properties. In: Reviewed Proceedings of the Society of Core Analysts Third European Core Analysis Symposium, Paris, France, 14-16 September. 2.4.2
- Börner, F., Gruhne, M., Schön, J., 1993. Contamination Indications Derived From Electrical Properties in the Low Frequency Range. Geophysical Prospecting 41, 83-98. 2.4.2
- Börner, F., Schön, J., 1991. A Relation between The Quadrature Component Of Electrical Conductivity And The Surface Area Of Sedimentary Rocks. Log Analyst 32, 613-613. 2.4.2, 3.2.2
- Börner, F., Weller, A., Schopper, J., 1996. Evaluation Of Fluid And Storage Properties in the Soil And Groundwater zone From Induced Polarization Measurements. Geophysical Prospecting 44 (4), 583-601. 2.4.2, 2.4.2, 2.4.2, 3.2.2
- Breede, K., 2006b. SIP-Messungen an Sandsteinen. Master's thesis, Technical University of Clausthal. 3.2.2, 3.7, 3.6, 3.7, 3.26, 7
- Breede, K., Weller, A., March, 6.-9th 2006. SIP-Messungen an Sandsteinen mit Lösungen unterschiedlicher Salze. In: DGG (Ed.), 66. Jahrestagung der Deutschen Geophysikalischen Gesellschaft (DGG). Bremen, Germany. 1.1
- Breede, K., Weller, A., Scott, J., 2005. SIP-Messungen an Sandsteinen mit Lösungen unterschiedlicher Salzkonzentrationen. In: 65. Jahrestagung der Deutschen Geophysikalischen Gesellschaft. Graz, Österreich. 1.1

- CETS, 1982. Conservation of Historic Stone Buildings and Monuments. National Academy Press, Washington D.C. 1.4
- Chelidze, T., Gueguen, Y., 1999. Electrical spectroscopy of porous rocks: A review-I. Theoretical models. *Geophysical Journal International* 137, 1-15. 2.2.2
- Chouteau, M., Beaulieu, S., 2002. An investigation on application of the electrical resistivity tomography method to concrete structures. Second Annual Conference on the Application of Geophysical and NDT Methodologies to Transportation Facilities and Infrastructure. 1.1
- Cole, K. S., Cole, R. H., 1941. Dispersion and absorption in dielectrics. *J. Chem. Phys.* 9, 341-351. 2.4.1
- Davis, J., James, R., Leckie, J., 1978. Surface ionization and complexation at the oxide/water interface. *J. Colloid and Interface Science* 63, 480-499. 2.2.2, 2.2.2, 5.1
- Desai, F. N., Hammad, H. R., Hayes, K. F., 1993. Background Electrolyte Correction for Electrokinetic Sonic Amplitude Measurements. *Langmuir* 9, 2888-2894. 5.1
- Dukhin, S., Shilov, V. N., 1974. Dielectric Phenomena and the Double Layer in Disperse Systems and Polyelectrolytes. John Wiley and Sons, New York. 2.2
- Fixman, M., 1980. Charges macromolecules in external fields, I, The sphere. *J. Chem. Phys.* 72, 5177-5186. 3.7
- Flath, D., 1989. The low-frequency complex electrical response of brine saturated shaly sandstones. Ph.D. thesis, University of Birmingham. 3.4
- Flatt, R. J., Ferraris, C. F., 2002. Acoustophoretic characterization of cement suspensions. *Materials and Structures/ Matériaux et Constructions* 35, 541-549. 5.1, 7
- Fuller, B., Ward, S., 1970. Linear system description of the electrical parameters of rocks. *IEEE trans. Geoscience Electronics, GE* 8, 7-18. 2
- Garboczi, E. J., 1998. Finite Element and Finite Difference Programs for Computing the Linear Electric and Elastic Properties of Digital Images of Random Materials. National Institute of Standards and Technology, Building and Fire Research Laboratory, Gaithersburg, Maryland 20899, <http://ciks.cbt.nist.gov/garboczi>, nistir 6269 Edition. 6.1, 6.1, 6.3, 7
- Gaudin, A. M., Fuerstenau, D., 1995. Quartz flotation with anionic collectors. *Trans. Am. Inst. Min. Metall. Pet. Eng.* 202, 66-72. 2.7, 7
- Hackley, Vincent, A., Malghan, Subhas, G., 1993. Investigation of Parameters and Secondary Components Affecting the Electroacoustic Analysis of Silicon Nitride Powders. In: Proceedings of Workshop "Electroacoustics for Characterization of Particles and Suspensions" held at the National Institute of Standards and Technology. Gaithersburg, Maryland, pp. 161-179. 5.1
- Holm, A., Krus, M., Wardzikowski, P., Sept., 17.-18th 1997. Bestimmung der Wasser- und Salzgehaltsverteilung durch Kombination von NMR- und γ -Durchstrahlungsmessungen. In: 9. Feuchttag. Weimar, pp. 203-217. 1.1

-
- Hunter, R. J., -. MATEC ESA 8000 - Estimation of effective radius of a distribution, application note No 101. Tech. rep., MATEC APPLIED SCIENCE. 5.1
- Jackson, P., Smith, D., Stanford, P., 1978. Resistivity-porosity-particle shape relationships for marine sands. *Geophysics* 43, 1250-1268. 2.5
- James, M., Hunter, Robert, J., O'Brien, Richard, W., 1992. Effect of Particle Size Distribution and Aggregation on Electroacoustic Measurements of ζ -Potential. *Langmuir* 8 (2), 420-423. 5.1
- James, R., Parks, G., 1982. Characterization of aqueous colloids by their electrical double layer and intrinsic surface chemical properties. *Surf. Colloid Sci.* 12, 119-216. 2.2.2
- Kabrede, H.-A., 2003. Feuchteschäden an Gebäuden, Schadenserkennung und Bewertung. In: Venzmer, H. (Ed.), *Aktuelle Entwicklungen der Bauwerkstroeknenlegung*. Verlag Bauwesen Berlin, Warnemünde, pp. 251-265. 1.4, 1.1, 7
- Kahle, M., 1994. Verfahren zur Erkundung des Gefügezustandes von Mauerwerk, insbesondere an historischen Bauten. Ph.D. thesis, Universität Karlsruhe. 1.1
- Kemna, A., 2000. Tomographic inversion of complex resistivity. Dissertation, Ruhr Universität Bochum. 3.5
- Kemna, A., Binley, A., Slater, L., 2004. Crosshole IP imaging for engineering and environmental applications. *Geophysics* 69 (1), 97-107. 2.2
- Kremer, F., Schönhals, A., 2003. *Broadband Dielectric Spectroscopy*. Springer-Verlag Berlin Heidelberg New York. 2.4.1
- Kruschwitz, S., Niederleithinger, E., Martin, T., February 21 -25 2005. Spektrale Induzierte Polarisation zur Charakterisierung von Baumaterial. In: 65. Jahrestagung der Deutschen Geophysikalischen Gesellschaft. Graz, Austria, pp. 296-297. 1.1
- Lataste, J., Sirieix, C., Frappa, M., Breyse, D., September 2001. Electrical resistivity measurement applied to non destructive testing in civil engineering: Influence of the humidity. In: Hill, I. (Ed.), 7th EEGS-Meeting 2001. University of Birmingham, pp. 60-61. 1.1
- Lataste, J. F., Sirieix, C., Breyse, D., Frappa, M., 2003. Electrical resistivity measurement applied to cracking assessment on reinforced concrete structures in civil engineering. *NDT and E International* 36, 383-394. 1.1
- Lesmes, D., Morgan, F. D., 2001. Dielectric spectroscopy of sedimentary rocks. *Journal of Geophysical Research* 106, 13334-13346. 2.2.2, 3.4, 5
- Lesmes, D. P., Friedman, S. P., 2005. Chapter: *Relationships between the Electrical and Hydrogeological Properties of Rocks and Soil* in *Hydrogeophysics*, 87-128. 2.1, 2.2
- Lesmes, D. P., Frye, K., 2001. The influence of pore fluid chemistry on the complex conductivity and induced polarization responses of Barea sandstone. *Journal of Geophysical Research* 106, 4079-4090. 1.1, 2.2, 2.1, 2.1, 2.2.1, 2.2.2, 2.4.1, 3.4, 7

- Li, H., de Bruyn, P., 1966. Electrokinetic and adsorption studies on quartz. *Surface Science* 5, 203-220. 2.7, 7
- Lobo, Victor, M. M., 1984. Electrolyte solutions: Literature data on thermodynamic and transport properties. Vol. 1 und 2. 3.7, 3.27, 7
- Lorne, B., Perrier, F., Avouac, J.-P., 1999. Streaming potential measurements 1. Properties of the electrical double layer from crushed rock samples. *Journal of Geophysical Research* 104 (B8), 17857-17877. 2.4, 2.2.2, 5.1, 5.1, 7
- Lubelli, B., van Hees, R. P. J., Groot, C. J. W. P., 2004. The role of sea salts in the occurrence of different damage mechanisms and decay patterns on brick masonry. *Construction and Building Materials* 18, 119-124. 1.4
- Major, J., Silic, J., 1981. Restriction on the use of Cole-Cole dispersion model in complex resistivity interpretation. *Geophysics* 46, 916-931. 2.4.1
- Marshall, D., Madden, T., 1959. Induced Polarization, A Study Of Its Causes. *Geophysics* 24 (4), 790-816. 2.2
- Matec Applied Science, 2006. User's Operation Manual, Version 2.1, Colloid Zeta Potential Measurement Without Sample Dilution. 2.3, 5.1
- Münch, M., Kemna, A., Vereecken, H., March, 6.-9th 2006. Beziehung zwischen SIP Relaxationszeit und Salinität, Korngröße, Sättigung bzw. hydraulischer Leitfähigkeit. In: 66. Jahrestagung der Deutschen Geophysikalischen Gesellschaft (DGG). Bremen, Germany. 2.5, 3.5, 4.2.2
- Münch, M., Kemna, A., Zimmermann, E., Vereecken, H., 2005. Abhängigkeit der SIP-Charakteristik von Salinität, Korngröße und Sättigung. *Deutsche Geophysikalische Gesellschaft, Graz*. 3.5
- Neville, A., 1997. *Properties of concrete*, 4th Edition. Wiley and Sons, Inc. 3.2.2
- O'Brien, R., 1988. Electroacoustic effects in a dilute suspension of spherical particles. *Journal of Fluid Mechanics* 190, 71-86. 5.1
- Oldham, Keith, B., Myland, Jan, C., 1994. *Fundamentals of Electrochemical Science*. Academic Press Inc. 2.2.2, 2.2.2, 2.2, 7
- Olhoeft, G., 1985. Low Frequency Electrical Properties. *Geophysics* 50, 2492-2503. 2
- Parks, G., 1984. Surface and interfacial free energies of quartz. *J. Geophys. Research* 89, 3997-4008. C, C
- Pelton, W., Sill, W., Smith, B., 1983. Interpretation of complex resistivity and dielectric data, part I. *Geophysical Transactions* 29, 297-330. 2, 2, 2, 2.4.1, 2.4.1, 2.4.1, 2.3, 7
- Pelton, W., Ward, S., Hallof, P., Sill, W., Nelson, P., 1978. Mineral Discrimination And Removal of Inductive Coupling with Multifrequency IP. *Geophysics* 43 (3), 588-609. 4.2.2

-
- Pride, S., Morgan, F., 1991. Electrokinetic dissipation induced by seismic waves. *Geophysics* 56, 914-925. 2.3
- Radic Research, 2007. Technical Specification SIP 256c. http://www.radic-research.de/Flyer_SIP256C_161104.pdf. 3.1.3
- Raupach, M., Wolff, L., 2002. Untersuchungen zur Leistungsfähigkeit und Dauerhaftigkeit von Hydrophobierungen auf Stahlbetonoberflächen mit Multiring-Elektroden. In: *Proceedings des 11.ten Feuchtetages in Weimar*. pp. 125-137. 1.1
- Revil, A., Glover, P., 1998. Nature of surface electrical conductivity in natural sands, sandstones and clays. *Geophys. Research Letters*, 691-694. 2.1, 2.2.2, 2.3
- Revil, A., Pezard, P. A., Glover, P. W. J., 1999. Streaming potential in porous media - 1. Theory of zeta potential. *Journal of Geophysical Research* 104, 21,012 - 21,031. 2.3, 2.3, 2.7, 7
- Scales, P. J., Griesner, F., Healy, T. W., 1990. Electrokinetics of the muscovite mica-aqueous interface. *Langmuir* 6, 582-589. 2.3
- Schön, J., 1996. *Physical properties of Rocks: Fundamentals and Principles of Petrophysics*. Elsevier Science Publishers, Oxford. 2.5, 3.4
- Schwarz, G. A., 1962. A theory of the low-frequency dielectric dispersion of colloidal particles in electrolyte solution. *J. Phys. Chem.* 66, 2636-2642. 3.7
- Scott, J., 2003. Low-frequency electrical spectroscopy of sandstone. Ph.D. thesis, School of Geography, Earth and Environmental Sciences, University of Birmingham. 3.2.2
- Scott, J., Barker, R., 2005. Characterization of sandstone by electrical spectroscopy for stratigraphical and hydrogeological investigation. *Quarterly Journal of Engineering Geology and Hydrogeology* 38, 143-154. 2.2.2, 3.7, 3.26, 7
- Scott, J. B. T., 2006. The origin of the observed low-frequency electrical polarization in sandstones. *Geophysics* 71, 235-238. 2.2.2, 3.6
- Scott, J. B. T., Barker, R., 2003. Determining pore-throat size in Permo-Triassic sandstones from low-frequency electrical spectroscopy. *Geophysical Research Letters* 30 (8). 2.2.2, 3.2.2
- Sen, P., 1981. Relation of certain geometrical features to the dielectric anomaly of rocks. *Geophysics* 46, 1714-1720. 3.5
- Sen, P., Goode, P., Sibbit, A., 1988. Electrical conduction in clay bearing sandstones at low and high salinities. *Journal of Applied Physics* 63, 4832-4840. 2.1
- Slater, L., Ntarlagiannis, D., Wishart, D., 2006. On the relationship between induced polarization and surface area in metal-sand and in clay-sand mixtures. *Geophysics* 71 (2), A1-A5. 3.2.2
- Telford, W., Geldart, L., Sheriff, R., 1990. *Applied Geophysics*. Cambridge University Press, Cambridge. 2.2

- Titov, K., Kemna, A. und Tarasov, A., Vereecken, H., 2004. Induced polarization of unsaturated sands determined through time-domain measurements. *Vadose Zone Journal* 3, 1160-1168. 2.2, 2.3, 7
- Titov, K., Komarov, V., Tarasov, V., Levitski, V., 2002. Theoretical and experimental study of time domain-induced polarization in water saturated sands. *Journal of Applied Geophysics* 50, 417-433. 2.2.2, 3.7, 6.2, 6.2.2
- Ulrich, C., Slater, Lee, D., 2004. Induced polarization measurements on unsaturated, unconsolidated sands. *Geophysics* 69, 762-771. 2.2.2, 2.5, 4.1, 4.2.3, 4.5, 6.2.5, 7
- Vanhala, H., 1997. Mapping Oil-Contaminated Sand And Till With The Spectral Induced Polarization (SIP) method. *Geophysical Prospecting* 45, 303-326. 2.4.1, 3.2.2
- Vinegar, H., Waxman, M., 1984. Induced Polarization Of Shaly Sands. *Geophysics* 49 (8), 1267-1287. 2.1, 2.4.2, 3.4
- Watillon, A., de Backer, R., 1970. Potentiel d'écoulement, courant d'écoulement et conductance de surface à l'interface eau-verre. *J. Electroanal. Chem., Interfacial Electrochem.* 25, 181-196. 2.7, 7
- Waxman, M., Smits, L., 1968. Electrical conductivities in oil-bearing shaly sands. *Society of Petroleum Engineers Journal* 243, 107-122. 2.1, 2.1, 2.1, 2.5
- Winsauer, W. O., Shearin, H. M. and Masson, P. H. W. M., 1952. Resistivity of brine-saturated sands in relation to pore geometry. In: *Bulletin of the American Association of Petroleum Geologists* 38 (2), 253-277. 2.5, 6.2.6
- Wyllie, M., Southwick, P., 1954. An experimental investigation of the SP and resistivity in dirty sands. *J. Pet. Technol.* 6, 44-57. 2.1
- Wyllie, R. M. J., 1957. *The fundamentals of electric log interpretation.* Academic Press, New York. 2.5

Acknowledgements

I am thankful to all my teachers who have challenged and encouraged me along the way. The thesis was supervised by Professor Ugur Yaramanci (Technical University Berlin, Germany), whom I wish to thank for his guidance and useful discussions. I am very pleased that I was given the opportunity to work with Professor Andreas Weller (Technical University Clausthal, Germany) and be able to benefit and learn from his expertise. My particular thanks are due to Professor Andrew Binley (Lancaster University, England). His insightful questions, always kind and competent counsel sincerely helped to improve this work. Just as well did his English proof-reading of the manuscript.

The Federal Institute of Materials Research and Testing (BAM, Berlin, Germany) provided the funding for this research. I am indebted to my division chief Dr. Herbert Wigganhauser and department head Dr. Heinrich Heidt for their effort and able personal commitment going unusual ways. Moreover I thank Ernst Niederleithinger for his valuable scientific guidance as well as for his long-standing encouragement and friendship.

The National Institute of Standards and Technology (NIST, Maryland, USA) provided additional sponsorship and laboratory facilities, which made this work possible. Most of all, I want to thank my group leader Dr. Edward Garboczi and Dr. Kenneth Snyder from the BFRL group at NIST for giving me considerable freedom to explore own ideas and always supporting me with any means necessary to finish. Dr. Richard Ricker and Dr. Vincent Hackley is thanked for their always instant assistance and technical advises.

I deeply acknowledge the contribution of Dr. David Lesmes (US Department of Energy), who has been as knowledgeable as supportive with his constructive remarks in discussing the findings of this study. His interest in my work sincerely encouraged me.

Many people have contributed with laboratory assistance. I appreciate the competence and professionalism of the staff at BAM, the Technical University Berlin and the National Institute of Standards and Technology. In particular I wish to thank Marco Lange (BAM) for both being a valuable example of German engineering skills and an even more precious friend.

I wish to give my parents the thanks they so richly earn. They patiently educated me about life and determined accompany me through setbacks and successes. Their reassurance keeps me going.

Lastly, I thank Erik Hansen and Francesca Capodagli for their support that always sustains me. Their close friendship pushes me forward and sound advice keeps me headed straight.

Vita

Sabine Kruschwitz was born in Berlin, Germany on November 15, 1976. After graduating from the Goethe Gymnasium in Berlin Wilmersdorf, she attended the Technical University of Berlin for the studies of Environmental and Applied Geosciences with an emphasis on Applied Geophysics. She graduated in February 2002 with a Dipl.-Ing. in Applied Geosciences. After working as a research fellow with the Federal Institute for Geosciences and Natural Resources (BGR) in Hannover, Germany until July 2002, she got enrolled in the PhD program of the Federal Institute of Materials Sciences and Research (BAM). During the course of her PhD she transferred for 9 months to the National Institute of Standards and Technology (NIST) in Gaithersburg, Maryland - USA. She is currently employed by BAM as a research fellow. Her permanent address is Niebuhrstraße 69, 10629 Berlin, Germany.